The role of tissue viscoelasticity in axon guidance during *Xenopus* brain development

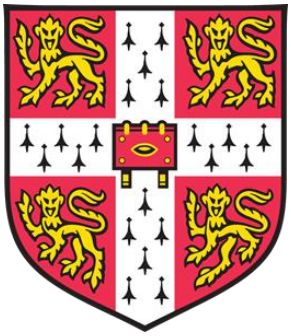

Ryan David Greenhalgh

Department of Physiology, Development and Neuroscience

Supervisor: Kristian Franze

University of Cambridge

Queens' College

NanoDTC

August 2022

This thesis is submitted for the degree of Doctor of Philosophy.

Declaration

I declare that:

- This thesis is submitted for the degree of Doctor of Philosophy.
- This thesis is the result of my own work and includes nothing which is the outcome of work done in collaboration except as declared in the preface and specified in the text.
- It is not substantially the same as any work that has already been submitted before for any degree or other qualification except as declared in the preface and specified in the text.
- It does not exceed the prescribed word limit for the Biology Degree Committee.

Signed: [Signature redacted]

Date: 6th August 2022

Ryan David Greenhalgh

Acknowledgments

I would like to first thank Sarah Foster for helping me get started with my experiments and always having good scientific conversations and coffee early in the morning. Eva Pillai for helping with injections and always being happy & helpful. Eva Kreysing for assistance with rodent experiments, always being enthusiastic about research questions, and spending the time to have deep technical discussions. Liz Williams for helping with general lab matters and for indulging in long lunches along with conversations about life. Julia Becker for stimulating conversations about AFM analysis making sure that I'm always keeping sharp. Katrin Mooslehner for help with making constructs and generally being a biology champion. Jana Sipkova for being a "good friend" as we like to put it and being supportive when experiments were challenging. Joy Thompson for assistance and advice with *in vivo* experiments when I was first getting started. Johannes Rheinlaender for discussions on AFM analysis and creep measurements. Andrea Dimitracopoulos for discussions about TFM and deep meaningful conversations. Max Jakobs for good discussion about machine learning and good book recommendations. The NanoDTC program for providing great training, a fantastic community, and support over the duration the PhD.

I'd also like to thank close friends, family, and advocates for supporting over the years including Victoria Greenhalgh, Christopher Greenhalgh, Clare Greenhalgh, George Claireaux, Vivek Badiani, William Ackernley, Nicholas Byres, Benjamin Devoy, Katie Woods, Alba Rocafort Marco, Hannah Benson, Katharina Tiesmeier, Katherine Ross, Ele Ward, Jonny Blaker, Nicola Tirelli, Jake Haigh, Scott Oliver, Karishma Jain, Rebecca Myers, and Haikal Pribadi.

Finally, I would like to thank Kristian for being a fantastic supervisor. When I first started the PhD I always thought it was about the pursuit of research. Further I got through the PhD, I found it was more about getting closers to the real version of myself. Kristian nurtures an environment for people to do this and I could not be more thankful. I would not be in the position I am now without the relationships and friendships that I formed during my time in Kristian's lab. I look forward to my future journey with Max Jakobs and Andrea Dimitracopoulos, a relationship and partnership which has been formed from Kristian's lab.

Summary

During nervous system development, axon bundles grow over large distances along well-defined pathways, guided by gradients of chemical cues in their environment. In addition, axons mechanically interact with their environment and respond to stiffness gradients they may encounter in the developing brain. In the model organism *Xenopus* laevis, retinal ganglion cell axons grow along the optic pathway toward the optic tectum. On their way through the mid-diencephalon, they turn caudally in response to gradients of the chemical guidance cues Semaphorin3A, Slit 1 and Slit 2 as well as tissue elasticity. However, while the importance of elasticity is becoming well-accepted in the context of development, biological tissues are not purely elastic but rather exhibit time-dependent mechanical properties known as viscoelasticity.

In this project, I developed a method based on atomic force microscopy (AFM) to measure the viscoelasticity of biological tissues (*in vivo Xenopus* brain and *ex vivo* rodent spinal cord tissue). To investigate the influence of viscoelasticity on axon guidance, I first investigated the mechanical properties of the developing brain *in vivo*. I found that the *Xenopus* brain exhibited heterogeneous viscoelasticity and that greater tissue elasticity is correlated with a greater tissue viscosity.

Subsequently, I wanted to understand how this heterogeneous tissue viscoelasticity may regulate axon growth. I developed tissue culture substrates with varying elasticities and viscosities and cultured *Xenopus* eye primordia explants on these substrates. I found that axons grew significantly longer on stiff elastic substrates compared to soft elastic substrates, reproducing previously published data, while there was no difference in axon length on soft and stiff viscoelastic substrates, indicating that viscosity is an important regulator of axon growth. I found that the regulation of axon length may be correlated with substrate timescale rather than by substrate elasticity. The substrate timescale is a measure of how long it takes a material to respond to an applied force or displacement; the shorter the timescale the faster the material response.

Next, I used computer simulations to understand how the ratio of elastic and viscous tissue behaviour impacts axon growth. Exploiting the motor clutch model, which is well established for explaining the mechanical interactions of cells and their environment, I used physiological relevant mechanics I derived from the developing *Xenopus* brain and viscoelastic tissue culture substrates to simulate axon velocity, retrograde flow, and traction forces using

elastic and viscoelastic frameworks. I found that the viscoelastic motor clutch model better described differences in axon lengths from the *in vitro* explant experiments. Furthermore, I found that the viscoelastic motor clutch model better describes axon velocities as a function of substrate timescale rather than the elastic framework.

The characteristic substrate timescale appeared to be an important parameter in regulating axon growth. To further investigate if the viscoelastic motor clutch model was sufficient to explain axon growth, I investigated how traction forces and retrograde actin flow were regulated by substrate mechanics. To automate and simplify traction force microscopy (TFM) analysis, I developed custom software that enables users to perform TFM analysis with little prior understanding or knowledge. I found that growth cones mainly applied "pulling" forces to compliant substrates, and that the magnitude of the pulling force could be regulated by substrate timescale. Finally, I measured cytoskeletal dynamics of the growing axon and found that retrograde actin flow rates and microtubule polymerization rates were regulated by substrate mechanics. My results suggest that axon guidance is not only regulated by elasticity but also viscoelasticity and the viscous component should be considered when studying axon pathfinding. A better understanding of axon path finding could help us learn more about the role of mechanics in development and how to treat diseases in the central or peripheral nervous system.

List of publications

Ryan D. Greenhalgh. Eva K. Pillai, Eva Kreysing, Rachel McKeown, Kristian Franze. **Axon growth is regulated by tissue viscoelasticity**. *(in preparation)*

Ryan D. Greenhalgh, Aki Stubb, Andrea Dimitracopoulos, Wolfram Pönisch, Ewa K. Paluch, Kristian Franze. **PyTraction, automated end-to-end analysis software for traction force microscopy**. *(in preparation)*

Julia Becker, Heiko Tzschätzsch, Anna Morr, Helge Herthum, Mehrgan Shahryari, Ryan D. Greenhalgh, Jing Guo, Leif Schröder, Christian Alzheimer, Silvia Budday, Kristian Franze, Jürgen Braun, Ingolf Sack **Mechanical properties of the hippocampus and corpus callosum: a comparative study using atomic force microscopy and magnetic resonance elastography in the murine and human brain**. (submitted)

Eva Kreysing, Jeffrey Mc Hugh, Sarah K. Foster, Kurt Andresen, Ryan D. Greenhalgh, Eva K. Pillai, Andrea Dimitracopoulos, Ulrich F. Keyser, Kristian Franze. **Global membrane tension is independent of polyacrylamide substrate stiffness.** *bioRxiv doi: https://doi.org/10.1101/2021.11.09.467973 (2021)*

Table of contents

List of Figures

List of Tables

List of Abbreviations

AA	**Acrylamide**
AFM	Atomic force microscopy
APS	Ammonium persulfate
APTMS	(3-aminopropyl)trimethoxysilane
BA	Bis-acrylamide
CNS	Central nervous system
ECM	Extracellular matrix
HA	Hydroxy-acrylamide
KMC	Kinetic Monte Carlo
LPA	Linear polyacrylamide
LPHA	Linear poly(hydroxy-acrylamide)
MBS	Modified Barth’s saline
MMR	Marc’s Modified Ringers Solution
NT	Normal Table of stage of Xenopus laevis
PAA	Polyacrylamide
PBS	Phosphate buffered saline
PLR	Power-law rheology
SLM	Standard linear model
TEMED	Tetramethylethylenediamine
TFM	Traction force microscopy

Mechanical definitions

Here the key mechanical definitions that are used in this thesis are defined. The definitions are intended to serve as reference for the reader and make the relations between different concepts clear. I have arranged the definitions in a logical order that builds on the previous definition.

Force (F) is an influence that can change the motion of an object. It can cause an object with mass to change its velocity and is calculated by $F = ma$ where *m* is mass and *a* is acceleration.

Displacement (δ) is the movement of a point from an initial position to a new position. Therefore, it is the change in position. δ is interchangeably used for displacement and indentation in this thesis.

Stress (σ) a force that is acting across an area (A) and is given by the formular is $\sigma = F/A$.

Strain (ϵ) a ratio of the total displacement to the initial dimension of the material of which a force is applied ($\epsilon = \Delta L/L_0$). Where, $\Delta L = l_f - l_0$ is the change in length, where l_f is the final length and l_0 is the initial length (before the force is applied).

Elasticity the ability for a body to resist deformation when subjected to force and return to its original shape when the force is removed. Most elastic materials exhibit linear elasticity under small deformations which can be described by Hooke's law $F = kx$. Where, x is the displacement (denoted as δ above) and k is known as the spring constant and quantifies the ability to resist deformation.

Spring an element that can be used to model and elastic element with spring constant k

Young's modulus (E) a mechanical property that measures the elasticity of a linearly elastic material under small deformations in a tensile or compressive configuration ($E = \frac{\epsilon}{\sigma}$). It is the ratio of the strain (ϵ) and stress (σ).

Poisson's ratio (v) is a measure that quantifies the deformation of a material perpendicular to the specific direction of loading. It is defined by the ratio of the change in transverse strain ($d\epsilon_x$) to the change in axial strain ($d\epsilon_y$) and is calculated by $v = -\frac{d\epsilon_y}{d\epsilon_x}$.

Bulk modulus (K) is a measure of how resistant a material is to compression ($E = 3K(1 - 2v)$). Where, E is the Young's modulus and v is the Poisson's ratio.

Shear modulus (G) is a measure of the resistance to a deformation when a force is applied parallel to one of its surfaces. It is defined as $E = 2G(1 + v)$, where E is the Young's modulus and v is the Poisson's ratio.

Strain rate (γ) the rate at which a material is deformed over time ($\gamma = \frac{d\epsilon}{dt}$). Where, $d\epsilon$ is the change in strain and dt is the change in time.

Viscosity (η) a measure of a fluid to resist a deformation at a given strain rate (γ). For a Newtonian incompressible fluid, it is defined as $F = \eta \frac{d\epsilon}{dt}$.

Dashpot an element that can be used to model a viscous element with a viscous constant η.

Viscoelasticity a body which has properties of both elastic solid and viscous liquid.

Force history the changes in forces applied to a overtime ($\frac{dF}{dt}$). Where, dF is the change in force and dt is the change in time.

Creep is the strain response $\epsilon(t)$ at a constant stress σ_0. It can also be written as the displacement response $\delta(t)$ at a constant force F_0 which will be used throughout the thesis.

Creep compliance function ($J(t)$) is the strain as a function of time divided by a constant instantaneous stress (σ_0). It is a measure of instantaneous continuous deformation ($J(t) = \frac{\epsilon(t)}{\sigma_0}$).

Volterra integral a convolution integral that considers the force history ($\frac{dF}{dt}$) and creep compliance (dt) according to an arbitrary viscoelastic model as a function of time (t). It is written as $\delta(t) = \int_0^t J(t - t') \frac{dF}{dt'} dt$. The equation is also known as the Boltzmann hereditary integral.

Stress relaxation is the stress response $\sigma(t)$ at a constant strain ϵ_0. It can also be written as the force response $F(t)$ as a constant displacement δ_0.

Storage modulus (G') is a measure of a materials ability to store energy elastically at a specific frequency (ω) in a shear configuration. It can be converted to its equivalent in compression or tension using $E' = 3K'(1 - 2v)$ and $E' = 2G'(1 + v)$.

Loss modulus (G'') is a measure of a materials ability to dissipate stress through heat at a specific frequency (ω) in a shear configuration. It can be converted to its equivalent in compression or tension using $E'' = 3K''(1 - 2v)$ and $E'' = 2G''(1 + v)$.

Complex modulus (G^*) is a measure of the stored energy (elastic G') and energy dissipated (viscous G''). It is related to the elastic and viscous components by $G^*(\omega) = G' + iG''$.

Loss tangent ($\tan\delta$) is a measure the relative contributions between the storage and loss modulus. It is related to the storage and loss modulus by $\tan\delta = \frac{G''}{G'}$. Note that the δ here does not refer to indentation. It is the phase between the storage and loss modulus.

Maxwell model comprises of a spring element and dashpot in series. It can be used to predict the force and displacement response of a viscoelastic body.

Voigt model comprises of a spring element and dashpot in parallel. It can be used to predict the force and displacement response of a viscoelastic body.

Standard linear model comprises of a spring (with short term stiffness, k_s) and dashpot in parallel that is in series with a spring (with long term stiffness, k_l). It can be used to predict the force and displacement response of a viscoelastic body.

Long term stiffness (k_l) is the stiffness of a body at long time scales i.e. $t \to \infty$.

Short-term stiffness (k_s) is the instantaneous stiffness i.e. at $t = 0$.

Effective stiffness is the combination of the long term and short-term stiffness ($k_l + k_a$).

Characteristic timescale physically describes how quickly stresses or strains relax within the substrate. For the standard linear model $\tau = \frac{\eta(k_l+k_a)}{k_l k_a}$.

Power law model is a model that captures the viscoelastic response of a body according to a power-law scaling relation. In this thesis, the power-law is defined as $J(t) = k_0 \left(\frac{t}{t_0}\right)^{\beta}$. Where, k_0 is the elastic stiffness at t_0, t is the time, and β is used to capture the extend which the material behaves as an elastic solid or viscous liquid. If $\beta = 0$ then the material is an elastic solid and if $\beta = 1$ then the material behaves as a viscous liquid.

Introduction

1.1. Anatomy of the Central Nervous System

1.1.1. Central Nervous System and the Neuron

The nervous system is responsible for regulating and communicating signals in almost all multicellular animals. The nervous system is composed of the central nervous system (CNS) and peripheral nervous system (PNS). The PNS is responsible for carrying signals anywhere outside the CNS. While the CNS takes in sensory information, processes information, and sends out information. The CNS is made up of two major structures which are the brain and spinal cord. Tissue in the CNS is largely made up of cells called neurons (Ransohoff and Cardona, 2010) which are specialized in sending and receiving sensory information. The neuron consists of a soma (cell body), dendrites, an axon, and synapses (Figure 1). Protein synthesis predominantly occurs in the soma, and it contains the nucleus of the cell. Dendrites protrude from the soma and are mainly responsible for receiving sensory information from other neurons. A long thin protrusion called an axon extends away from the soma. The axon can extend very long distances away from the soma and it is mainly responsible for sending signals away from the neuron to other neurons. The tip of the axon contains synapses that are mainly responsible for communicating with target neurons using chemical neurotransmitters. Before synapses form connections with other neurons, they must grow from the soma to their dendritic targets. While the axon is growing towards its target the tip is known as the growth cone which I will introduce in the following section.

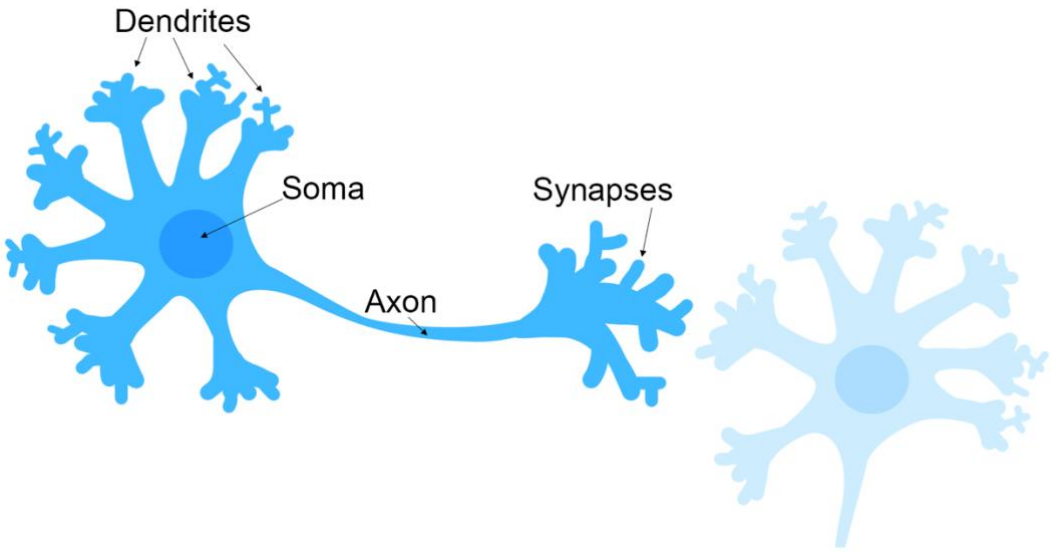

Figure 1 Schematic illustration of a neuron.

The four main components of the neuron are the soma, dendrites, an axon, and synapses. There are multiple dendrites that protrude from the soma. A long thin protrusion called the axon extends from the soma and is terminated with synapses that connect to dendrites of other neurons. Signals are sent by the neuron along the axon and dendrites receive signals from other neurons.

1.1.2. Anatomy of the growth cone

Santiago Ramon y Cajal, a renowned Spanish neuroscientist, made several discoveries in neuroanatomy. In 1887, he learnt how to stain neurons using Golgi's method in Barcelona. Cajal utilized Golgi's method to reignite his artistic side and meticulously made detailed drawings of the CNS from an extensive set of species. In the 1890s, he coined the term "growth cone" which refers to the structure at the tip of growing axons and dendrites. An original drawing from Santiago of a chick embryo growth cone can be seen in Figure 2a.

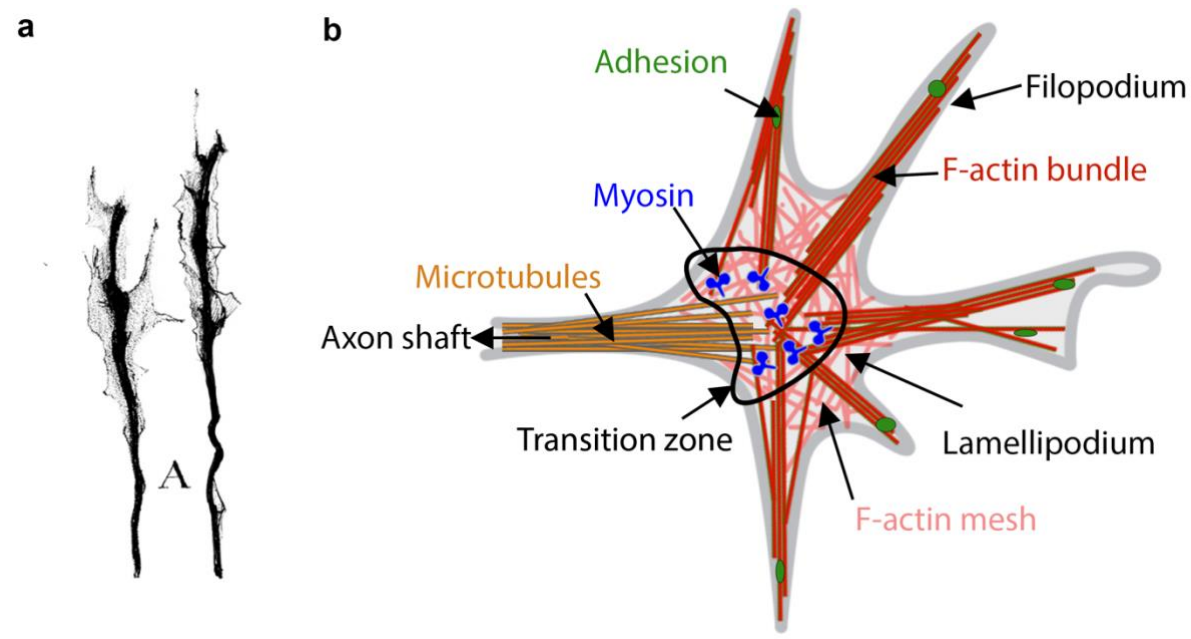

Figure 2 Anatomy of the growth cone.

a) Original drawings from Ramón y Cajal of growth cones in white matter reproduced from (Ramón y Cajal, 1909, García-Marín et al., 2009) b) Schematic illustration of growth cone adapted from (Franze, 2020) and the key cytoskeletal components. Microtubule bundles (orange) make up the axon shaft and grow into the transition zone (black circle). F-actin bundles (red) elongate into the filopodium while F-actin mesh (light red) form the flat lamellipodium. Myosin motors (blue) are in the transition zone and pull the F-actin bundles into the transition zone. Adhesion sites (green) link F-actin bundles to the ECM across adapter proteins and transmembrane proteins.

The growth cone is a highly dynamic and motile structure that can interact with chemical or mechanical stimuli (Gomez and Letourneau, 2014). The anatomy and key cytoskeletal components of the growth cone are illustrated in Figure 2b. At the base of the growth cone is the axon shaft which is composed of tightly bundled microtubules (Figure 2b, orange: microtubules) (Tanaka and Kirschner, 1991). Microtubules are polymers of tubulin and can grow micrometres in length (Jakobs et al., 2021). Microtubules generally grow up to the transition zone (Figure 2b, black circle: transition zone) at which point F-actin becomes the dominant cytoskeletal component (Figure 2b, red: actin). It is not shown in the diagram but an actin arc is formed in the transition zone which is made from a contractile actomyosin bundle (Schaefer et al., 2002). It should be noted that microtubules can polymerize into regions distal from the transition zone (Kahn and Baas, 2016). F-actin is prefixed with “F” to indicate the filament like structure that it exhibits. Flat regions of the growth cone are called lamellipodium

and contain mesh like F-actin filaments (Figure 2b, light red: F-actin filaments). Longer protrusions elongate from the growth cone which are known as filopodium and are composed of F-actin bundles (Figure 2b, red: F-actin filaments). A detailed analysis of the growth cone cytoskeleton can be found in a study from Atherton et al. (2021).

F-actin filaments are physically linked to the external environment at adhesion sites (Figure 2b, green: adhesion). Integrins which are transmembrane proteins link to binding sites in the extracellular matrix (ECM) (usually short amino acid sequences) (Jalali et al., 2001). Intracellularly, integrins are linked to actin by an adaptor protein and its respective binding partner (Elosegui-Artola et al., 2018). The physical link that is formed between the actin filament and ECM is often referred to as a "molecular clutch" (Plotnikov et al., 2012). F-actin is pulled towards the transition zone by myosin motors in the transition zone. At the same time, actin is further polymerized at tip of the filament against the membrane. As actin flows into the transition zone from the pulling force generated by myosin motors and it is depolymerized by ADF/cofilin (Tedeschi et al., 2019).

1.2. Development and axon pathfinding

1.2.1. Developing *Xenopus* optic tract as a model system

There are many developmental processes in which axons or bundles of axons grow to a target location which is known as axon pathfinding. There are a variety of model systems including mice, zebrafish, and fruit files that can be used to understand the mechanism of axon pathfinding. The most studied pathways are commissures and topographic maps. Commissures are regions of the CNS where axons cross the midline of the nervous system to reach their targets (Chédotal, 2014). Commissures are particularity interesting because axons must be first attracted to the midline and then immediately repulsed after crossing the midline. For example, axons crossing the ventral spinal cord in mice (Messersmith et al., 1995). Topographic maps are regions of the CNS where axons in one tissue project across another tissue in an organised manner. Generally, it is accepted that the organised projection of axons in topographic maps or guidance in commissures are regulated by chemical or mechanical cues or gradients of these cues.

The *Xenopus* as a model system has previously been used for studying topographic maps in neural development by many groups (Zhang et al., 1998). The *Xenopus* can be reared at room temperature over relativity quick timescales which makes it easy to do a higher turnover of experiments. Furthermore, optic tract development in the *Xenopus* has been extensively used to investigate axon pathfinding (Harris, 1986, Harris, 1989). During CNS

development, axons of retinal ganglion cells (RGCs), whose cell bodies are located in the retina (Figure 3a, retina), grow out of the retina, into the brain, and then through the brain to their targets in a region called the optic tectum (Figure 3a-b) (Harris, 1989). As the RGC axons grow along the optic pathway toward the tectum they undergo a stereotypical caudal turn in the mid-diencephalon (Figure 3b, turn highlighted with asterisk). It has been demonstrated that the turning processes in the mid-diencephalon may be regulated by both chemical and mechanical guidance cues.

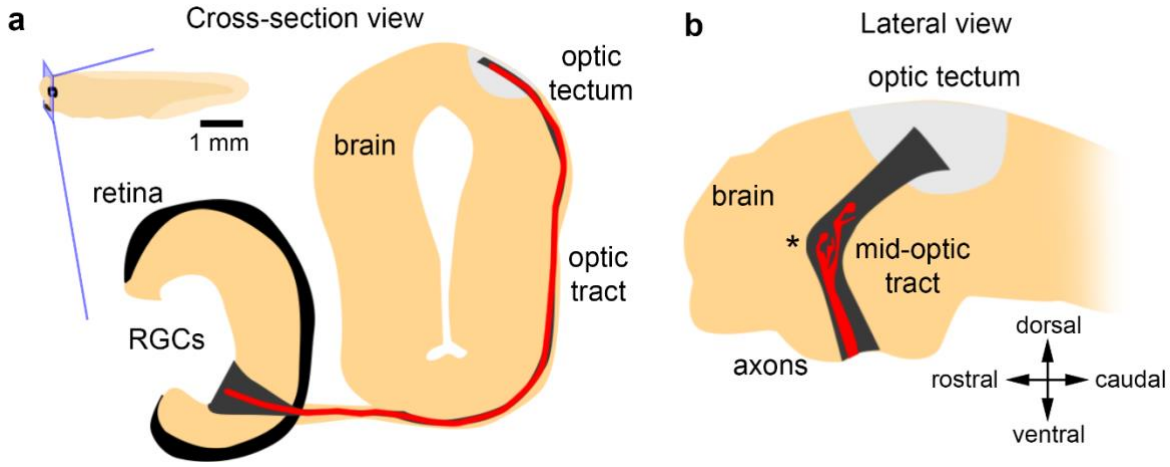

Figure 3 Anatomy of the developing *Xenopus* brain.

a) Cross-section view of Xenopus brain and retina. Axons grow from the cell bodies of RGCs in the retina to the optic tectum of the contralateral brain hemisphere. B) Lateral view of Xenopus brain. Axons grow into the brain and make a caudal turn towards the tectum. Asterisk denotes the turning point. Axons shown in red.

It has been shown in the Franze lab over the last few years that the *Xenopus* system is good for measuring the mechanical properties of the developing optic tract *in vivo* while the animal is still healthy (Koser et al., 2016, Thompson et al., 2019). It is also easy to remove the developing eye primordium at similar stages to *in vivo* and culture growing axons while controlling the mechanical and chemical environment (Koser et al., 2016). Thus, it is possible to measure the effects of chemical and mechanical cues in comparable environments *in vivo* and *in vitro* to untangle the axon pathfinding process.

1.2.2. Growth and guidance of the axon

During axon pathfinding both actin and microtubules, which are key cytoskeletal components, are highly dynamic and motile. Despite knowing that the motile cytoskeleton leads to the forward advancement of the growth cone, it is not clear what the specific mechanism is for axon advancement and how this is regulated. In 1899, Cajal proposed a chemotactic hypothesis

of axon growth and highlighted that mechanics may be important in the advancement of the growth cone (Ramon and Cajal, 1899). Despite, Cajal and others highlighting the importance of mechanics in the 19th century, the mechanistic details of how chemistry and mechanics regulate the advancement are still not fully understood. There are two main mechanisms of axon growth named "tip-growth" and "stretch growth". Tip growth refers to the process where mass addition occurs at the tip of the axon whereas stretch growth refers to the axon shaft stretching (Franze and Guck, 2010).

It has become accepted that the leading edge of the growth cone advances forwards mainly from actin polymerization. Within the transition zone actin is depolymerized and at the leading edge it is polymerized (Chan and Odde, 2008). The polymerization force of actin filaments in the filopodium are on the order of 10 pN/μm and therefore the addition of an actin monomer (~ 10 nm) would produce a pushing force of 0.1 pN which may not be sufficient to deform the membrane. Mogilner and Oster (1996) proposed the "elastic Brownian ratchet" model to explain the extension of filopodium. As long thin actin filaments bend due to thermal fluctuations monomers can polymerise without the steric hindrance of the plasma membrane. When the filament returns to its original position it pushes the membrane forwards leading to advancement of the filopodium.

The advancement of the actin filament from polymerization is counteracted by actin retrograde flow. Actin retrograde flow is stochastically modulated by forming links to the ECM by molecular clutches. When a linkage is formed between an actin filament and the ECM the pulling force of myosin is resisted by the ECM and the actin retrograde flow rate is reduced. Subsequently, more pushing forces are generated (by polymerization or elastic Brownian ratchet) on the filopodium resulting in enhanced advancement. Lin and Forscher (1995) demonstrated that retrograde flow rates are proportional to growth cone advancement.

It is established that the outgrowth is mainly a consequence of actin polymerization, however, there is some evidence that microtubules may play a key role regulating advancement (Dogterom and Koenderink, 2019). During growth, microtubules can penetrate into the transition zone and it is thought that they can mediate transport into protrusions and promote retrograde flow by RAC signalling (Dogterom and Koenderink, 2019). Actin filaments and microtubule bundles are important for the steering of the growth cone (Zhou et al., 2002). The actin arc in the transition zone inhibits microtubules from freely polymerizing into the growth cone and advancing (Santos et al., 2020, Dupraz et al., 2019). This suggests that the actin cytoskeleton plays a key role in the advancement of the growth cone by regulating the extent

which the microtubules can grow. Therefore, it is likely that both actin and microtubule polymerization is the key driver for axon advancement.

Along with axon outgrowth, the cytoskeleton regulates the direction in which the axon travels. The growth cone can turn towards attractive chemical guidance cues or away from repulsive guidance cues (Dent et al., 2011). The turning generally requires the coordination of actin and microtubules. Generally, attractive chemical guidance cues cause actin to asymmetrically incorporate on the side of the growth cone closest to the attractive chemical cue. Repulsive guidance cues generally disrupt the actin cytoskeleton closest to the repulsive chemical cue leading to repulsion. It has been shown that turning of the growth cone can occur by asymmetric invasion of microtubules into the growth cone periphery (Tanaka and Kirschner, 1995, Lee and Suter, 2008). Furthermore, it has been shown that if microtubules are stabilised or depolymerize the growth cone loses its ability to turn (Williamson et al., 1996). This demonstrates that turning of the growth cone is strongly regulated by cytoskeleton dynamics.

1.3. Regulation of axon pathfinding

1.3.1. Chemical regulation in axon pathfinding

Chemical signalling during optic tract development has been extensively studied across different vertebrates. The chemical signals involved in steering axons from RGCs to their targets in the optic tectum are evolutionary conserved (Erskine and Herrera, 2007). There is an established body of literature that demonstrates the important of chemical guidance cues during optic tract development.

When axons from the RGCs first sprout from the eye they grow towards the optic chasm where they are exposed to Netrin-1 (Deiner et al., 1997). Netrin-1 is a well-known example of an attractive chemical guidance cue (Serafini et al., 1996). It is named after the Sanskrit word “netr”, which means “one who guides”. Netrin-1 causes an upregulation of actin production on the side of the growth cone closest to the cue (Welshhans and Bassell, 2011). Therefore, RGC axons will grow towards netrin as they travel towards to optic chasm. The optic chasm is a prominent midline decision point where axons are directed contralaterally or ipsilaterally. During this stage of development, both Ephrins and Slits have been shown to guide axons (Nakagawa et al., 2000, Rasband et al., 2003) (Figure 4a, most ventral region of the optic tract ephrins are found rostral to the optic tract and slits caudal).

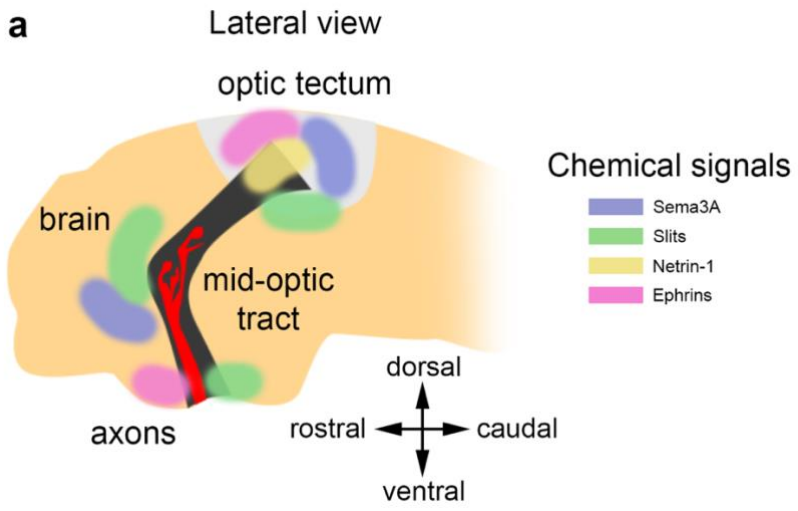

Figure 4 Chemical signalling cues in the developing *Xenopus* brain.

a) Lateral view of Xenopus brain. Axons grow into the brain and are exposed to different chemical signals including Sema3A (purple), Slits (green), Netrin-1 (yellow), and Ephrins (pink).

Once axons have crossed the optic chasm they grow towards the mid-diencephalon where they are exposed to gradients of Sema3A and Slits (Erskine and Herrera, 2014). Sema3A and Slits are expressed as RNAs at higher levels rostral to the optic tract and at lower levels caudal to the optic tract (Campbell et al., 2001, Piper et al., 2006). The gradient from high expression levels to low levels is thought to repel axons in the mid-diencephalon towards the tectum (Figure 4a Slits (green) and Sema3A (blue) are expressed rostral to the optic tract at the mid-diencephalon). There is evidence to suggest that the expression of Slits and Sema3A is regulated by fibroblast growth factor signalling (Atkinson-Leadbeater et al., 2010).

After axons have grown past the mid-diencephalon they grow into the tectum where they are exposed to several chemical cues including Sema3A, Slits, Netrin-1 and Ephrins (van Horck et al., 2004) (Figure 4a see chemical signals in optic tectum (grey region most dorsal)). When the RGC axons reach the tectum, they branch out and make their synaptic connections in a process known as retinotopic mapping. Netrin and Sema3A are mainly responsible for managing branching of axons in the tectum (Kalil and Dent, 2014). Netrin and Sema3A can both promote or inhibit branching (Dent et al., 2004) and hence make it possible to manage the branching in the tectum. Evidence suggests that Slits surrounds the tectum to prevent branching outside the tectum (Piper et al., 2006). Finally, Ephrins are mainly responsible for spatially

coordinating the termination of RGC axons to have the same neighbours in the tectum as they do in the retina (O'Leary and McLaughlin, 2005).

Despite there being a large body of literature surrounding chemical guidance cues they will intrinsically lead to a modulation of the forces that are applied by the growth cone to advance, retract, or stall. Subsequently, it is important to understand how the mechanics of the surrounding environment regulates the behaviour of the growth cone. In the following section (1.3.2), I will review how mechanics can regulate the growth and guidance of axons.

1.3.2. Importance of mechanics in the Central Nervous System

Classically, it has been established that axon pathfinding is regulated by chemical guidance cues (Kalil et al., 2011, Erskine and Herrera, 2007, Wen and Zheng, 2006). We are familiar with chemical signals from everyday life. For example, imagine you are lost in a forest with no food, but you suddenly smell campfire sausages coming from one direction. You would follow the chemical signal (i.e. the smell of sausages), just like the growing axon. If we think back to the sausage smelling example, when traveling towards the food, there are many different routes that could cover several terrains. For example, it could be a boggy marshland which is difficult to walk through because there's loads of resistance from the "soft" dirt or there could be a rigid stone pathway that is "stiff" and easy to walk on. Analogous to this real-life example, biological tissues have mechanically "soft" and "stiff" regions (Koser et al., 2015, Moeendarbary et al., 2017) which have been shown to regulate axon growth (Koser et al., 2016).

Previously in the Franze lab we have investigated the role of mechanics during the optic tract development. While other AFM studies on *ex vivo* live brain tissue have demonstrated that the brain tissue is heterogeneous (Elkin et al., 2007, Elkin et al., 2010, Christ et al., 2010) these studies did not capture an active development process and its relation to tissue mechanics. Koser et al. (2016) found that the RGC axons that grow along the optic pathway undergo a stereotypical caudal turn in the mid-diencephalon, which is correlated with a gradient in tissue stiffness (Figure 3b, turn highlighted with asterisk). The stiffness of the tissue was higher rostral to the optic tract (Figure 3b, right of asterisk) and softer caudal to the optic tract (Figure 3b, left of asterisk). The tissue rostral had stiffnesses on the order of ~200 Pa while the tissue stiffness caudal were on the order of ~175 Pa. It was hypothesised that the increase in stiffness caused axons to travel faster on the stiffer rostral side and slower on the softer caudal side. Subsequently, the axons were pulled towards the softer side due to the velocity mismatch. Koser et al. (2016) also found that there were higher cell densities rostral to the optic tract while

the cell densities were lower on the caudal side. Therefore, the turning behaviour could have also been regulated by a steric effect. In the Koser et al. (2016) study, tissue stiffnesses were only measured at two developmental stages. To capture how the stiffness temporally evolved during the optic tract development Thompson et al. (2019) made time-lapse measurements using AFM and fluorescent microscopy.

Thompson et al. (2019) investigated the evolution of the mechanical properties during optic tract development. It was found that the tissue rostral to the mid-diencephalon stiffened as the optic tract approached the turning point. Local tissue stiffness was largely regulated by cell proliferation similar to the observation from Koser et al. (2016). It was also found that tissue stiffened 20 minutes before the axons arrived at the turning point. Furthermore, when the tissue was treated with chondroitin sulphate, a polysaccharide that is known to chemically soften tissue, the axon trajectory was perturbed. This suggests that elasticity is important for regulating the guidance and growth of axons *in vivo*.

To investigate the role of elasticity *in vitro* researchers have developed substrates with tuneable chemical and mechanical properties that can be used to culture cells or tissues (Lutolf and Hubbell, 2005, Moshayedi et al., 2010). Koser et al. (2016) cultured axons from *Xenopus* eye primordia explants on soft (0.1 kPa) and stiff (1 kPa) polyacrylamide (PAA) substrates to investigate the effects of elasticity *in vitro*. It was found that explants cultured on stiff (1 kPa) substrates grew longer compared to explants on soft (0.1 kPa) substrates. Axons on stiffer substrates also had higher extension velocities and grew straighter. Therefore, it would be expected that gradients in tissue elasticity (observed *in vivo*) contribute to axon growth during development. Several other studies have investigated the role of elasticity on axon growth dynamics from different animal models. For example, Flanagan et al. (2002) cultured primary neurons from mouse spinal cord and found that substrate elasticity significantly regulated branching of neurons.

It is well established that chemical cues can regulate the growth of axons by changing the cytoskeletal dynamics (as discussed in 1.2.2). For axons to respond differently to substrate elasticity, it would be expected that cytoskeletal dynamics change in different mechanical environment. Chan and Odde (2008) extensively studied the role of stiffness in the regulation of actin retrograde flow and subsequently force generation in their seminal paper. Since 2008, there have been several publications investigating the role of tissue stiffness in axon growth and guidance. Miguel-Ruiz and Letourneau (2014) showed that Arp2/3, a complex that regulates actin dynamics, is dependent on substrate stiffness and growth cone dynamics. The

fact that chemical signalling is linked to mechanics suggests that the properties of the mechanical microenvironment are important for regulating cell behaviour. Literature suggests that substrate mechanics can regulate the growth and guidance of axons. However, many biological tissues are not purely elastic solids. They exhibit a property called viscoelasticity which I will introduce in the following section of the introduction.

1.3.3. The importance of viscoelasticity in biology

Both studies from Koser et al. (2016) and Thompson et al. (2019) have looked at the role of elasticity in developmental axon growth and guidance. The importance of elasticity and mechanics is becoming well-accepted in the context of development. Biological tissues are viscoelastic, and viscoelasticity has been shown to regulate the dynamics of the actin cytoskeleton. There is no work to date investigating the role of viscoelasticity during the optic tract development. However, others have measured viscoelasticity of biological tissues using AFM. Antonovaite et al. (2021) mapped the viscoelasticity of mouse brain tissue and found that tissue viscoelasticity was heterogeneous. However, these measurements were not performed on intact brain tissue, nor could the authors correlate the mechanics with a developmental process. For that reason, it would be interesting to understand the viscoelasticity of the developing *Xenopus* brain and how this could regulate axon growth and guidance.

Elastic materials can return to their original shape after been stretched. When viscous materials are deformed, they flow and do not return to their original shape. When a force is applied per unit area of material (stress, σ) the material will deform (strain, ϵ). For a linearly elastic material the stress is equal to the Young's Modulus (E) multiplied by the strain ($\sigma = E\epsilon$) in a tensile configuration (note that not many materials are linearly elastic and the strain rate, that is how quickly the material is deformed can have a large impact on the measured Young's Modulus). The Young's Modulus can be physically understood as a resistance to deformation when a material is stressed; the higher the modulus the stiffer the material.

For a viscous material, the stress is proportional to the viscosity (η) multiplied by the strain rate ($d\epsilon/dt$) and the stress can be written as $\sigma = \eta d\epsilon/dt$. Here, it is important to note that the stress in a viscous material will depend on how quickly the material is deformed (strain rate, $d\epsilon/dt$). The viscosity can be physically understood as the resistance to flow at a given strain rate: higher the viscosity higher the resistance to flow at a given strain rate. Therefore, a combination of elastic and viscous properties gives rise to time-dependent mechanical properties because the stresses of the viscous component depend on the strain rate.

Viscoelastic material properties can be quantitively described in terms of the complex modulus. The complex modulus is a measure of the stored energy (elastic) and energy dissipated (viscous). By convention, the stored energy is expressed as the storage modulus (G') and dissipated energy as the loss modulus (G''). The complex modulus exhibits time-dependent properties. For example, if silly putty is dropped from a height and hits the ground it will bounce. This is because when silly putty is deformed fast it exhibits elastic properties. When silly putty is deformed slowly it flows like a fluid. Rather than describing deformation rates as slow or fast it is convention to describe it in terms of frequency. Therefore, fast and slow deformation corresponds to high and low frequency, respectively. It has been demonstrated that tissues have a loss modulus that is 10 – 20 % of the storage modulus (Charrier et al., 2018, Lu et al., 2006). Therefore, a biological tissue with a storage modulus of 100 Pa should have a loss modulus in the range of 10 to 20 Pa. There is experimental (Charrier et al., 2018) and theoretical (Gong et al., 2018) evidence that cells respond to viscoelasticity, but this has not been explored *in vivo* or in any developmental context yet to my knowledge.

1.4. Modelling axon growth and guidance

There is evidence that suggests that both the chemical and mechanical environments regulate axon growth and guidance. Modelling and simulation enable us to hypothesise physical models and make predictions to better understand biological systems. Several studies have come up with computational chemical and mechanical models to explain axon growth (Oliveri et al., 2021, Craig, 2018). The most notable mechanical model was from Chan and Odde (2008). They proposed a stochastic model of the motor-clutch force transmission system, where clutch molecules link actin to the substrate and mechanically resist myosin driven actin retrograde flow. For example, the actin retrograde flow can be thought of as a treadmill that travels at a constant velocity if a spring is then attached to the treadmill the velocity will be reduced due to the spring resisting the flow. Springs with different stiffnesses will create different resistances. In the case presented here, the stiffness of the spring corresponds to the stiffness of the substrate. The model proposed by Chan and Odde (2008) predicts two key regimes “frictional slippage” and “load-and-fail”. Frictional slippage regime is associated with fast retrograde flow and low traction forces on stiff substrates. Whereas the load-and-fail regime is associated with slower retrograde flow and higher traction on soft substrates.

It is important to highlight that mechanistically the motor clutch model can be used to model both cell spreading and the dynamics of filipodium. Chaudhuri et al. (2015) first investigated the role of substrate stress relaxation on cell spreading and found that soft

viscoelastic substrates promoted cell spreading. A substrate that flows faster to release generated stresses has a faster stress relaxation. While a substrate with a slow stress relaxation retains the elastic energy for longer. If the stress relaxation tends to infinite time the body will behave elastically. Gong et al. (2018) and Chaudhuri et al. (2015) have explained these observations by extending the motor clutch model to simulate the effects of a cell interacting with a viscoelastic substrate. Interestingly, they found that on soft elastic substrates with a viscous component cell spreading would be enhanced. More recently, Adebowale et al. (2021) investigated the effects of substrate viscoelasticity on lamellipodial protrusions and filopodia. Adebowale et al. (2021) used the motor-clutch model to create a computational model to explain cell migration on a 2D viscoelastic substrate. They found that filopodia length and lifetime increase on substrates with a faster stress relaxation which was also explained by the motor-clutch model. Furthermore, they found that the mode of migration was dominated by filopodia on soft viscoelastic substrates. Given that axons form filopodia to probe their surroundings the current body of literature provides great motivation for investigating the effects of viscoelasticity on the regulation of axon growth and guidance.

1.5. Measuring viscoelasticity *in vivo* using AFM

1.5.1. Introduction to AFM

To understand how and if viscoelasticity regulates axon growth and guidance, the mechanics of viscoelastic biological tissues and synthetic substrates need to be measured at the correct spatiotemporal resolution. Mechanics can be measured in tissue by ultrasound (Sridhar and Insana, 2007) and microrheology (Guo et al., 2014) but these techniques do not provide the cellular and time resolution accessible by atomic force microscopy (AFM). Brillouin microscopy is faster and has a better resolution than AFM but requires careful calibration of material properties (refractive index and density). AFM measures the force interactions between a cantilever with a known stiffness and a substrate. AFM can be used in a variety of modes, here the focus will be on force and creep mapping. The premise of the technique is based on Hooke's law

$$F = -kx, \qquad \text{Eq 1}$$

where k is the spring constant and x is the deflection of the cantilever. The deflection of the cantilever is measured using a laser that is reflected on the surface to a photodiode. When the cantilever is above the sample the laser is reflected into the centre of the photodiode. As the cantilever is extended towards the sample, the cantilever is deflected shifting the position of the laser in the photodiode. Upon contact with a soft biological sample the cantilever will

indent the sample. Using Hooke's law (Eq. 1), the indentation is proportional to force over the elastic stiffness of the sample, the exact relationship depends on the cantilever geometry and is usually non-linear. When the stiffness of a material is higher there is more deflection in the cantilever and hence the substrate is stiffer.

When using AFM for mapping the elasticity of biological tissues, sharp AFM tips can cause damage to samples, therefore, cantilevers with spherical tips are generally used. However, indenting with spherical tips leads to a mechanics problem, that is with increasing indentation depth the contact area increases due to the geometry of the tip. Later in the thesis (section 3.2), I will cover the methods used to correct this problem.

1.5.2. Measuring viscoelasticity using AFM

Recent advancements in AFM permit viscoelastic characterisation (Schierbaum et al., 2019, Efremov et al., 2019, Rheinlaender and Schäffer, 2019). There are several different methods to measure viscoelasticity using AFM. In this section, I will introduce the different types of measurements that can be made which are schematically summarized in Figure 5.

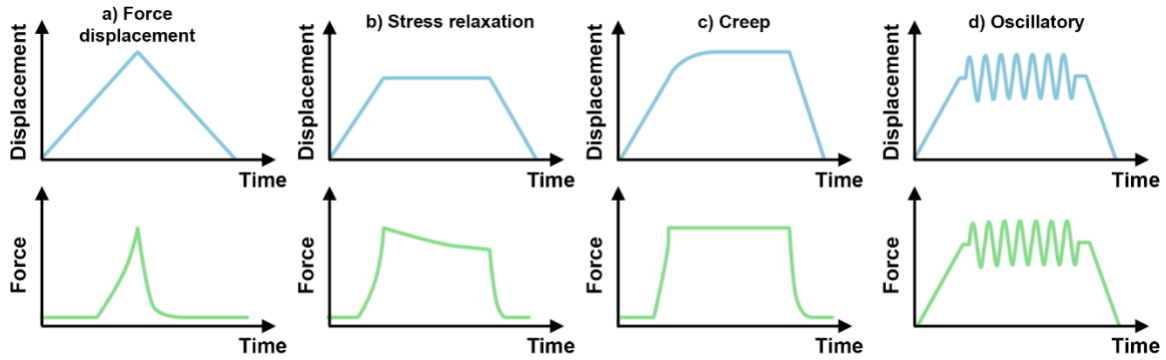

Figure 5 Different operating modes of AFM for measuring viscoelasticity.

a) Force displacement, b) stress relaxation, c) creep, and d) oscillatory. The top panel shows the displacement response over time and the bottom panel shows the force response over time.

Several authors have demonstrated that it is possible to recover viscoelastic information from force displacement curves (Figure 5a) (Garcia et al., 2020, Garcia and Garcia, 2018b, Efremov et al., 2017). When a tip is pushed into a viscoelastic sample to a set point and retracted there is hysteresis between the approach and retraction parts of the curve. This hysteresis is due to viscous loss and using this information it is possible to recover viscoelastic material properties. However, this method can be computationally expensive and hard to process due to tip adhesion on the retraction part of the curve.

Chim et al. (2018) reported the use of stress relaxation experiments using AFM. In a stress relaxation experiment, the cantilever is indented into the sample to a set indentation

point. The deflection of the cantilever is measured which can be used as a proxy for the current force (effectively stress) (Figure 5b, green curve). For viscoelastic materials, the force decreases overtime because the material is relaxing after being deformed. Silly putty can be used to understand this again. Imagine sticking your finger 1 cm into a ball of silly putty and holding it at that fixed position. At very short times you would feel the putty pushing back onto your finger and overtime you would feel less of a pushing action on your finger. Since silly putty will continue to flow there will be a point whereby your finger is no longer touching the material. Feeling less force overtime on your finger is a consequence of stress relaxation. Generally, the analysis for this type of experiment is simple, however, errors are introduced since it is assumed that the indentation reaches the set-point instantaneously which is often not the case. The stress relaxation that occurs generally exhibits an exponential decay which makes it easy to Fourier transform to recover the dynamic response (Chim et al., 2018).

Creep experiments are very similar to stress relaxation experiments (Figure 5c) but the force is held constant, and the indentation is measured as a function of time (Hecht et al., 2015, Hiratsuka et al., 2009, Schierbaum et al., 2019, Rheinlaender and Schäffer, 2019). A silly putty analogy can be used again to understand this experiment. If a pound coin was dropped on the top of silly putty it would apply a constant force on the surface ($F = ma$). Overtime, the coin would slowly sink into the putty which is a consequence of viscoelastic creep. Similar to stress relaxation, errors can be introduced because it's not possible to apply an instantaneous force ramp. Several publications from Rheinlaender (Hecht et al., 2015, Schierbaum et al., 2019, Rheinlaender and Schäffer, 2019) demonstrated that the force history could be accounted for by modelling the force ramp using a polynomial.

Finally, viscoelastic properties can also be measured using oscillatory AFM which unlike stress relaxation or creep experiments operate in the frequency domain (Figure 5d) (Antonovaite et al., 2021). Oscillatory measurements are very similar to those that are measured using a shear rheometer but the AFM configuration operates in a compression mode rather than shear. Such measurements require more sophisticated instruments and experimenters compared to other modes. The analysis is also more complex, but it is possible to get accurate frequency information about the viscoelastic material properties. Another limitation of oscillatory AFM measurements is that they take much longer compared to force-displacement, stress relaxation, and creep experiments which makes it challenging to map viscoelasticity *in vivo* of intact tissue.

1.6. This work

Here, I performed AFM measurements to map the viscoelastic properties of *Xenopus* brain tissue during development at cellular resolution. Currently, it is not possible to decouple the elastic and viscous component by perturbing the system *in vivo*. Thus, I produced viscoelastic gels with tuneable elasticity and viscosity to investigate the effects of viscoelasticity on axon guidance *in vitro*. I found that brain tissue exhibits heterogenous viscoelastic properties *in vivo* and soft viscoelastic and stiff elastic or viscoelastic gels promote axon growth *in vitro*. Therefore, viscoelasticity may play a critical role in axon guidance during development.

Methods and materials

2.1. Materials

All chemicals were obtained from Sigma-Aldrich unless stated otherwise. All animal experiments in this report were conducted in accordance with home office guidelines and the ethical review committee of the University of Cambridge.

Several stock solutions were made for *in vivo* and *in vitro Xenopus* experiments. The compositions of the stock solutions are outlined in Table 1.

Table 1 Table showing composition of stock solutions for *in vivo* and *in vitro Xenopus* experiments.

Solution	Composition
Marc's Modified Ringers Solution (MMR), 10× stock solution (pH 7.6, 10L volume)	NaCl (Cat: S9888, 584.4g), KCl (Cat: P9541, 14.9g), MgCl2.6H2O (Cat: M2670, 20.33g), CaCl2.2H2O (Cat: C7902, 29.4g), EDTA disodium salt 0.5M (Cat: 03690, 20 mL), HEPES (Cat: H3784, 119.4g), 10M NaOH (Cat: S8045, ~ 20 mL), filter sterilise.
Modified Barth's saline (MBS), 10× stock solution (pH 7.6, 1L)	NaCl (Cat: S9888, 51.3g), KCl (Cat: P9541, 0.738g), NaHCO3 (Cat: 401676, 2.02g), HEPES (Cat: H3784, 23.83g), MgSO4.7H20 (Cat: 63138, 2.02g), Ca(NO3)2.4H20 (Cat: C2786, 0.78g), CaCl2.6H2O (Cat: 21108, 0.9), 4M NaOH (~7 mL), filter sterilise.
Xenopus tissue culture medium (pH 7.6-7.8)	Leibowitz L15 medium (Cat: L1518, 60 mL), Pen Strep Fungizone 100x (1 mL), ddH2O (39 mL), 1 M NaOH (~90 uL), filter sterilise.
MS222 stock solution (pH 7.6-7.8)	1x MBS or MMR (198 mL), MS222 (Cat: E10521, 80 mg), Pen Strep Fungizone 2 mL (Lonza, Cat: 17-745E), 1M NaOH (~180uL), filter sterilise.

2.2. Elastic and viscoelastic substrates

2.2.1. Synthesis of linear acrylamides

Linear poly(hydroxy-acrylamide) (LPHA) or linear polyacrylamide (LPA) were synthesised using a modified protocol (Charrier et al., 2018). For LPHA, the acrylamide stock (AA, Acrylamide solution,40%, for electrophoresis, sterile-filtered, Cat: A4058, Lot: SLBW1664) solution was diluted to contain a 5 % (w/v) monomer (mol ratio = 1 : 0.19 for AA:H, where H = N-hydroxyethyl acrylamide, Cat: 697931, Lot: MKCG4369), whereas, for LPA only 5 % (w/v) of acrylamide monomer was used. The 5 % acrylamide solution was added to a round bottom flask, purged with nitrogen, and held under vacuum three times. The polymerization was initiated by adding 0.024% ammonium persulfate (APS, Honeywell, UK, Lot: H1670) and 0.05% tetramethylethylenediamine (TEMED, Fisher Scientific, UK, Lot: 121303292) and the reaction mixture was continuously stirred for 2 hrs at 37 °C. It was important to purge and degas the reaction mixture three times before adding the APS and TEMED else the polymerization was unsuccessful. A viscous liquid was obtained from the reaction and stored at 4 °C until further use.

2.2.2. Fabrication of elastic and viscoelastic substrates.

Elastic substrates were fabricated by polymerizing acrylamide and bis-acrylamide (Bis acrylamide Solution (2% w/v/Electrophoresis), Fisher BioReagents Thermo Fisher Scientific, Cat: BP1404-250) to make a crosslinked network. To make viscoelastic substrates linear polyacrylamide was introduced into the elastic network to introduce a viscous component. The table below (Table 2) outlines the compositions of elastic and viscoelastic substrates and further experimental details can be found in the current section (2.2). When fluorescent beads were introduced to the mixture (bead tracking experiments outlined in section 2.2.6) an equivalent volume of phosphate buffered saline (PBS) was removed.

Table 2 Showing volumes of premix used to make elastic and viscoelastic gels with tuneable elasticity and viscoelasticity.

G' = storage modulus, G'' = loss modulus.

Type / Target mechanics (G'/G'') [Pa]	Acrylamide (AA) 40 %w/v [µL]	Bis-Acrylamide (BA) 2% w/v [µL]	Linear polyacrylamide (LPA) 5% w/v [µL]	PBS [µL]	Fluorescent beads [µL]
Elastic 100 Pa / 0 Pa	24.7	12.35	0	362.9	+8 uL beads -8 uL PBS
Elastic 300 Pa / 0 Pa	63	17.5	0	419.5	+10 uL beads -10 uL PBS
Elastic 1 kPa / 0 Pa	36.4	18.2	0	345.3	+8 beads -8 PBS
Elastic 10 kPa / 0 Pa	76.4	38.2	0	285.3	0
Viscoelastic 100 Pa / 10 Pa	50	18	220	112	0
Viscoelastic 1 kPa / 100 Pa	80	25	220	75	0

Round bottom dishes 35 mm (uncoated) with a 20 mm glass diameter (FluoroDish World Precision Instruments or 35mm dish, No. 0 coverslip MatTek Corporation) were treated with 1 mL of 0.1 M NaOH and then aspirated. The dishes were then treated with (3-aminopropyl)trimethoxysilane (APTMS, Lot: BCBW4932) for 3 mins and then rinsed extensively with ddH2O. The dishes were then treated with glutaraldehyde (Cat: 340855 0.5%) for 30 mins, washed in ddH2O three times, and dried with argon. Round bottom glass coverslips (18 mm) were placed in Wash-N-Dry™ coverslip racks and sonicated in ethanol, ddH2O, and then RainX (amazon) for 5 minutes and then dried with argon.

Monomer solutions (as outlined in Table 2) with a volume of 400 uL were initiated by adding 1.2 uL of TEMED and 4 uL of APS. Samples with a volume of 500 uL of monomer solution were initiated with 1.5 uL of TEMED and 5 uL of APS. Once the polymerization had been initiated, 10 – 20 uL of solution was pipetted onto 20 mm glass treated round bottom dishes and the RainX treated 18 mm coverslips were dropped vertically onto the polymer solution and the round bottom dishes were inverted. After 30 minutes of polymerization the dishes were incubated with PBS for 30 minutes and then the RainX treated coverslips were removed. The PBS in the dishes were replenished and the gels were stored at room temperature until further use.

2.2.3. Fabrication of hydroxy elastic gels

An acrylamide stock (AA/HA) solution was made by adding 400 µL of 40 % acrylamide (AA, Lot: SLBW1664) to 65 µL of 100 % hydroxyl-acrylamide (HA, Lot: MKCG4369). A premix solution was made by adding 500 µL of the acrylamide stock solution to 250 µL of 2 % bis-acrylamide (BA, Fisher Scientific, UK, Lot: 182176). The storage modulus (G') of the gels was controlled by mixing the premix solution with different ratios of phosphate buffered saline (PBS, Fisher Scientific, UK). 400 µL of the premix corresponding to 0.1 kPa (2.471 %HA + 0.062 %BA), 1 kPa (3.644 %HA + 0.091 %BA), and 10 kPa (7.644 %AA + 0.191 %BA) were polymerised by adding 4 µL ammonium persulfate (APS, Honeywell, UK, Lot: H1670) and 1.2 µL of tetramethylethylenediamine (TEMED, Fisher Scientific, UK, Lot: 121303292). The solution was mixed gently with a pipette and 25 µL was transferred onto the treated glass coverslips then a RainX treated coverslip was placed on top. Gels were left for 30 minutes to polymerise and then covered in PBS until further use.

2.2.4. Fabrication of hydroxy viscoelastic gel

Viscoelastic gels were prepared by polymerising AA and BA (elastic component) in a solution of LPHA (viscous component). Similar to the elastic gels, different ratios of premix to PBS were used to control the storage modulus and LPA or LPHA was used to tune the loss modulus (G''). Gels were tuned to have a loss modulus around 10 % of the storage modulus. 400 µL of the premix corresponding to 0.1 kPa (5 %HA + 0.09 %BA + 2.75 %LPHA), 1 kPa (8 %HA + 0.125 %BA + 2.75 %LPHA), and 10 kPa (9 %HA + 0.2 %BA + 3.3 %LPHA) were polymerised by adding 4 µL ammonium persulfate (APS) and 1.2 µL of tetramethylethylenediamine (TEMED). The solution was mixed gently with a pipette and 25 µL was transferred onto the treated glass coverslips then a RainX treated coverslip was placed on top. Gels were left for 30 minutes to polymerise and then covered in PBS until further use.

2.2.5. ECM coating

Elastic and viscoelastic gels surfaces that had not been functionalized with a hydroxy group (2.2.3 and 2.2.4) were functionalised with hydrazine hydrate (Cat: 225819). PBS was replaced and surfaces were functionalised by treating the sample for 4 hrs with hydrazine hydrate. Hydrazine hydrate was removed and replaced with 5% acetic acid (Cat: A6283) and incubated for exactly 1 hrs. Acetic acid was removed and gels were washed 3× with PBS before being exposed to UV light. The PBS was removed and replaced with poly-D-lysine (Cat: P6407, 70–150 kDa, 100µg mL^{-1} overnight), washed twice with PBS for 30 min, and incubated in laminin (Cat: L2020, 1:100) for 2 hrs. Gels were washed twice in PBS and then replenished with the

desired cell culture medium. Elastic and viscoelastic gels that had been functionalised with N-hydroxyethyl acrylamide before polymerization were treated with poly-D-lysine (70–150 kDa, 100μg mL^{-1} overnight), washed twice with PBS for 30 min, and incubated in laminin (1:100) for 2 hrs.

2.2.6. Traction force microscopy gels

Far-red beads with diameters of 200 nm or 40 nm (FluoSpheres™ Carboxylate-Modified Microspheres, 0.2 µm, dark red fluorescent (660/680) , Thermo Fisher Scientific Cat: F8807, 2% solids and FluoSpheres™ Carboxylate-Modified Microspheres, 0.04 µm, dark red fluorescent (660/680), 5% solids, azide free, Thermo Fisher Scientific Cat: F8789). For elastic gels, 10 µL of beads were added to gel mixtures (500 µL) in place of 10 µL of PBS to obtain a final bead concentration of 2 %v/v as outlined in Table 2. Gel solutions were polymerised by adding 5 µL ammonium persulfate (APS) and 1.5 µL of tetramethylethylenediamine (TEMED). The solution was mixed gently with a pipette and 10 µL was transferred onto the treated glass coverslips then a RainX treated coverslip was placed on top. The dishes were then inverted so that the beads sunk to the surface of the RainX treated coverslip. Gels were left for 30 minutes to polymerise and then covered in PBS and coated according to section 2.2.5.

2.3. Rheology

The storage and loss modulus were determined with oscillatory rheology using a Kinexus pro+ rheometer (Malvern Panalytical, stress-controlled rheometer, UK). Polymerisation of gels was initiated using APS and TEMED as previously described (section 2.2), and 2 mL of sample was loaded onto the rheometer. Curing was monitored by measuring G' and G'' for 30 mins at 2 % strain and 0.159 Hz at 20 °C. After 30 mins, once the storage and loss moduli had plateaued the final values were taken.

2.4. Molecular biology

2.4.1. Constructs

pCMV/pCAG-LifeAct Plasmid Reference 60101: 20 µg of plasmid DNA containing the GFP2 tagged LifeAct sequence expressed under the CMV promoter was purchased from ibidi. To generate larger amounts of plasmid DNA 20 ng of plasmid was used to transform 50 µL of chemically competent DH5 alpha (Invitrogen/Fisher Scientific, cat no 18265017).

EB3-tdTomato plasmid from 'addgene' Reference 50708 (Merriam et al., 2013): plasmid were received in bacteria. The bacteria were streaked out on to LB agar plates

containing 50 μg/mL Kanamycin and single colonies were picked, and clones grown as described below (section 2.4.2). The plasmid yield from midi preps was about 150 μg per 50 mL prep.

2.4.2. Growing vectors

A frozen aliquot of competent cells in Eppendorf tube were thawed on ice, 1-2 μL of plasmid (20 ng) was added and gently mixed by finger tapping, left on ice for 30 mins, then heat shocked at 42 °C in heat block for 20 seconds and left to sit on ice for a further 2 minutes. The transformed bacteria were then added to 1 mL of prewarmed LB medium and left to shake at 200 RPM for 1 hour. 100 μL was plated out on to LB agar plates containing 50 μg/mL Kanamycin.

After overnight incubation at 37 °C single colonies were picked and grown overnight in 3 mL LB/50 μg/mL Kanamycin. 500 μL of this overnight culture was the used to infect 50 mL of LB/Kanamycin, and grown overnight at 37 °C. Plasmid DNA of the 50 mL culture was prepared using the QIAfilter Plasmid Midi Kit (cat no 12243). Bacteria were harvested by spinning the 50 mL culture at 6000rcf at 4 °C for 15 mins in a SIGMA-16K benchtop centrifuge, lysed, filtered and applied to a DNA binding column according to protocol. The 5 mL eluted fraction was precipitated with isopropanol and the DNA spun down in a Sorvall RC6+ at 15000 RCF 30 mins at 4 °C. After washing the pellet with 70 % ethanol it was dried and taken up in 50 μL Rnase/Dnase free water and the concentration measured by nanodrop. The plasmid map and sequence were downloaded from the ibidi and the plasmid from the regrown stock was sequenced with CMV F primer: 5′ – CGC AAA TGG GCG GTA GGC GTG – 3′ by sanger sequencing to confirm the plasmid identity. Growing of vectors were performed by Katrin Mooslehner (Franze lab, PDN, Cambridge).

2.5. Xenopus husbandry, dissection, and cell culture

2.5.1. *Xenopus* husbandry

Animal experiments were approved by the University's Ethical Review Committee and complied with guidelines set by the UK Home Office. *Xenopus* husbandry was conducted by Tomas, other members of the Franze lab, and myself. Single-cell-stage, wild-type *Xenopus laevis* embryos of both sexes were fertilised *in vitro* with mechanically crushed testes. Embryos were sourced from our frog facility at the Gurdon institute. In brief, eggs were transferred from the egg laying solution to a 50 mL falcon tube and washed with 1x MMR three times by inverting the falcon tube and removing the excess liquid. Eggs were then transferred into petri

dishes and all excess liquid was removed. A small piece of testes (25 % of whole testes) were cut and placed in an Eppendorf tube containing 1 mL of 1x MMR. Testes were either homogenized using a pestle and approximately 2 drops were added to the embryos. Otherwise, lumps of testes were mechanically rubbed across the embryos for a few tens of seconds. The dishes were left to sit for 8 – 10 minutes and then 0.1x MMR was used to flood the petri dish to lower the salt concentration which activates the sperm and allows fertilization to occur. Petri dishes were gently agitated to un-clump the eggs. Dishes were left for approximately 30 minutes until the embryos turned (fertilized embryos turn so the dark part of the embryo is facing upwards). Any embryos that didn't turn were removed and the liquid in the dish was replenished with fresh 0.1x MMR. Dishes were then transfer to the incubator between 12 °C and 18 °C to reach the desired developmental stage, as described by Nieuwkoop and Faber (1994). Embryos were cleaned daily, and all embryos used in this project were below stage 41.

2.5.2. Microinjection of constructs

Xenopus embryos at the four-cell stages were injected in a single or both dorsal blastomeres with LifeAct or EB3 as described in section 2.4.2. After fertilization, embryos were dejellied by incubation in 2% w/v L-cysteine (Cat: C7352) in 0.1x MBS, pH 8.00 for around 3 minutes. Once, the embryos had got to the four-cell stage they were transferred into an injection dish with a plastic mesh tapped to the bottom and Ficoll (400, Cat: F4375) solution (4 % w/v in 0.1x MBS, pH 7.5, with 1x PSF).

Injection needles were prepared by pulling glass capillary tubes (1.0 mm outer diameter by 0.5 mm internal diameter) and the tips were mechanically broken to make an orifice. Injection solutions (LifeAct or EB3) were added to the needle via capillary action and needles were loaded onto a micromanipulator. The needle was then calibrated by tuning the injection settings on the FemtoJet (Eppendorf) to yield a volume of ~ 5 nL per droplet in mineral oil according to a graticule in the stereoscope lens. Embryos were left in Ficoll for a few hours to recover and transferred into 0.1x MMR and placed in the incubator at 14 – 18 ºC and left to grow as per un-injected embryos (2.5.1). Before, dissection embryos were screened using a fluorescence stereoscope and embryos that were fluorescent were selected for further experiments. Injections were conducted by Eva Pillai and Rachel McKeown (Franze lab, PDN, Cambridge).

2.5.3. *Xenopus* exposed brain preparation for *in vivo* imaging

Xenopus exposed brain preparations were conducted according to Koser et al. (2016). Briefly, embryos were anesthetized in tricane methanesulfonate solution (0.04% MS222 in 1× MMR + 1× PSF, pH ~7.4) and pinned down in a Petri dish coated with polydimethylsiloxane (PDMS) using L-shaped 0.2 mm pins. The skin, dura, and eye primordium were removed using forceps and 0.1 mm dissecting pins, exposing the brain from the dorsal to ventral midline. For control samples, brains at stage 38/39 (Nieuwkoop and Faber, 1956) were exposed to modified Ringer's solution (MMR) and left for no longer than 1 hour before imaging.

2.5.4. *Xenopus* eye primordia explant cultures

Embryos at stage 34-36 NT were anesthetized in tricane methanesulfonate solution (0.04% MS222 in 1× MBS + 1× PSF, pH ~ 7.4). Whole eye primordia (stage 34 – 36 NT) were dissected using 0.15 mm insect pins on PDMS coated Petri dishes, transferred onto purely elastic or viscoelastic gels, and cultured overnight (14 – 24 hrs) in culture medium (60 % L-15 medium, 100 U/mL penicillin, 100 µg/mL streptomycin, and 2.5 µg mL amphotericin B at pH ~7.4). Explants were imaged using a Lecia Dmi8 (10× objective, NA = 0.4) or an inverted Nikon (Ti-E at room temperature) equipped with a sCMOS (Prime BSI Scientific, Photometrics), a CoolLED pE-4000, and ×10 objective (numerical aperture NA = 0.25, Nikon). Sholl analysis (Sholl, 1953) was performed to determine the medium axon length for each explant using an some custom software in Python that was built on top of ImageJ (Fuji, version 1.52i) plugin which is further described in section 2.12.6.

2.6. Rat husbandry and dissection

Animal experiments were approved by the University's Ethical Review Committee and complied with guidelines set by the UK Home Office. Rats were obtained from Charles River and kept under standard husbandry conditions on a 12/12 light dark cycle and on a standard laboratory rat chow ad libitum. Dissections and sample mounting were performed by Julia Becker (Franze lab, PDN, Cambridge).

2.7. Atomic force microscopy

AFM experiments were conducted using a JPK Nanowizard Cellhesion 200 (JPK Instruments AG, Germany) with a custom-fit fluorescence microscope (Zeiss AxioZoom V16) mounted above the AFM head (Thompson et al., 2019). Polystyrene beads (37 µm or 20 µm diameter, microParticles GmbH, Germany) were glued onto Arrow-TL1 tipless silicon cantilevers (NanoWorld, Switzerland) that had a stiffness of 0.004 – 0.036 N/m determined by thermal

noise. *Xenopus* embryos with exposed brains immobilised on PDMS coated Petri dishes (section 2.5.3) were loaded onto a x-y motorised stage below the AFM head. Data points were acquired every 25 µm in a raster scan to build up an elastic or viscoelasticity map with a maximum indentation force of 10 nN, approach speed of 5 µm s^{-1}, data rate of 2 kHz, with a constant-force step of 10 nN for 3 s using a custom-written script.

All mechanical parameters and their governing equations are summarised in Table 4. Figure 7 schematically shows the typical fitting procedure implemented. For a full mathematical description of all models and data analysis refer to section 2.12.2, section 3.2, and section 3.3. All data was fitted using a custom library summarized in section 2.12.2.

2.8. Optical imaging

After culturing explants for 16 – 24 hrs cells were imaged using phase contrast illumination on an inverted microscope (Leica Dmi8) with a digital sCMOS camera (ORCA-Flash4.0, Hamamatsu Photonics), an EL6000 illuminator (Leica), and an ×10 objective (numerical aperture NA = 0.4, Leica). Measurements were also performed using an invested Nikon (Ti-E at room temperature) equipped with a sCMOS (Prime BSI Scientific, Photometrics), a CoolLED pE-4000, and ×10 objective (numerical aperture NA = 0.25, Nikon).

2.9. Traction force microscopy

After culturing explants for 16 – 24 hrs explants were imaged using an inverted Nikon microscope (Ti-E at room temperature) equipped with a sCMOS (Prime BSI Scientific, Photometrics), a CoolLED pE-4000, and ×60 oil objective (numerical aperture NA=1.4, Nikon). Fluorescent images of beads (FluoSpheres™ Carboxylate-Modified Microspheres, 0.2 µm, dark red fluorescent (660/680)) and wide-field images were taken every 5 mins for 1 hour. After time-series image acquisition, the culture media were exchanged with trypsin (Thermo Fisher Scientific, Cat: 25300054) or sodium dodecyl sulfate (Cat: L3771) to detach the explants from the gel. Reference images of fluorescent beads were taken 15 min after trypsinization or immediately after sodium dodecyl sulfate treatment.

2.10. Time lapse imaging of actin retrograde flow and microtubule polymerization

Cytoskeletal flow dynamics of actin and microtubules were captured using an inverted Nikon (Ti-E at room temperature) equipped with a sCMOS (Prime BSI Scientific, Photometrics), a CoolLED pE-4000, and ×60 oil objective (numerical aperture NA=1.4, Nikon). Images of fluorescently transfected explants were recorded every 4 seconds for 4 minutes.

2.11. Kinetic Monte Carlo Simulations

2.11.1. Elastic motor clutch model

The motor clutch model first developed by Chan and Odde (2008) simulates the traction dynamics of F-actin bundles, myosin motors, and molecular clutches that are mechanically interacting with an elastic substrate. In essence, the myosin motors pull the actin filament towards the cell body (retrograde flow) at a maximum unloaded velocity (v_u) which occurs when the actin filament is not bound to the substrate though a molecular clutch. Clutch engagement is modelled using an effective association rate (r_{on}) and once engaged a force is transmitted between the actin filament and the substrate. As myosin continues to pull tension develops within an engaged clutch until failure, here failure is modelled using an effective dissociation rate (r_{off}) according to the Bell model

$$r_{off} = r_{off}^0 e^{F_{clutch}/F_b}, \quad \text{Eq 2}$$

where r_{off}^0 is the unloaded dissociation rate of the molecular clutch, F_b is the characteristic threshold force for rupture, and F_{clutch} is the force within a given clutch that can be expressed as

$$F_{clutch(i)} = k_{clutch}(x_i - x_{sub}), \quad \text{Eq 3}$$

where the clutch is modelled as a Hookean spring with a stiffness k_{clutch} at position x_i in relation to the substrate at position x_{sub}. As the tension increases that acts against the myosin motors and slows the velocity of the actin filament which is modelled using a linear force-velocity relation as

$$v_f = v_u\left(1 - \frac{k_{sub}x_{sub}}{N_m F_m}\right), \quad \text{Eq 4}$$

where N_m is the number of myosin motors and F_m is the characteristic stalling force for a single myosin motor, and k_{sub} is the stiffness of the substrate. Following the work of Elosegui-Artola et al. (2014) and Gong et al. (2018) experimental and computational work has demonstrated that focal adhesions grow on stiff substrates via the recruitment of integrins. Athamneh et al. (2015) demonstrated that Aplysia growth cones undergo a reinforcement mechanism like other cell types. I incorporated reinforcement into the model as an option argument to run simulation with or without reinforcement. To model focal adhesion reinforcement, I employed the approach of Gong et al. (2018) by modifying the effective association rate constant by

$$r_{on} = r_{on}^0\big(1 + \alpha(F_a - F_{cr})\big), \quad \text{Eq 5}$$

where r_{on}^{0} is initialized binding rate, F_a is the average clutch force and F_{cr} is the clutch reinforcement threshold. Therefore, the association rate (r_{on}) is given by $r_{on}^{0}(1 + \alpha(F_a - F_{cr}))$ when the average clutch force (F_a) exceeds the clutch reinforcement threshold (F_{cr}) else is given by r_{on}^{0}. The α parameter characterises the sensitivity of the association rate with increasing clutch force. Notably, Elosegui-Artola et al. (2014) model the effective association rate as $r_{on} = r_{on}^{0} d_{int}$, where d_{int} is the density of integrin. Therefore, it can be assumed that the effective adhesion can be modelled by $(1 + \alpha(F_a - F_{cr}))$. Using the above analysis, it was possible to perform Kinetic Monte Carlo (KMC) simulations to predict the average clutch tension (F_a) and effective adhesion (d_{int}) as a function of substrate stiffness.

For each time step, molecular clutches are first enabled to associate with F-actin according to the association rate constant (r_{on}) and then tested against the dissociation rate (r_{off}). This is achieved by stochastically computing the binding and unbinding times by for engaged clutches to unbind (t_{unbind}) or unbound clutches to engage (t_{bind}), respectively. The binding times are calculated by $t_{bind/unbind} = \frac{-\log\left(URN(n_{ceng/cdiseng})\right)}{r_{on/off}}$ where URN is a uniform random number generator, n_{ceng} is the number of engaged clutches, and $n_{cdiseng}$ is the number of disengaged clutches. Upon engagement, the forces in the clutches (F_{clutch}) must balance with the forces in the substrate (F_s)

$$F_s = F_{clutch} \implies k_{sub} x_{sub} = k_{clutch} \sum_{i=0}^{n_{eng}} \left(x_{clutch,i} - x_{sub}\right), \qquad \text{Eq 6}$$

where $x_{clutch,i}$ is the position of engaged clutch i and k_{clutch} is the stiffness of the clutch. Eq. 6 can be rearranged to give,

$$x_{sub} = \frac{k_{clutch} \sum_{i=0}^{n_{eng}} x_{clutch,i}}{k_{sub} + n_{eng} k_{clutch}}, \qquad \text{Eq 7}$$

where n_{eng} is the number of engaged clutches. From the position of the substrate, it is possible to update the force and therefore the velocity of the actin filament (v_f) using Eq.4. The clutch position is then updated by multiplying the velocity by the time step ($v_f \Delta t$) which can be used to update the force in each clutch and the disassociation rate for the next time step. For each simulation, 10,000 events were computed with a time step of 5 ms. Each simulation was repeated 100 times to yield the mean behaviour. General model parameters are discussed in section 2.11.3 and a characteristic length scale of focal adhesions was selected to be 1 μm meaning that 1 kPa = 1 pN/nm.

2.11.2. Viscoelastic motor clutch model

For the viscoelastic case, the spring in the elastic case (2.11.1, Eq. 6) can be replaced with a standard linear model (SLM) element. For the spring and dashpot in series the force in each element should be equal hence

$$\eta \frac{dx_\eta}{dt} = k_a x_a. \quad \text{Eq 8}$$

Where, η is the viscosity of the dashpot, dx_η is the change in displacement in the dashpot, k_a is the addition stiffness of one of the springs in the SLM, and x_a is the displacement of that spring. The sum of the displacement in the spring (x_a) and dashpot (x_η) must be equal to the displacement of the substrate ($x_{sub} = x_a + x_\eta$) and Eq.8 can be rewritten as

$$\eta \frac{dx_\eta}{dt} = k_a\left(x_{sub} - x_\eta\right). \quad \text{Eq 9}$$

Where x_η is the position of the dashpot. When a clutch is linked to the SLM element the forces must be balanced ($F_{clutch} = F_{SLM}$). Therefore, the force equilibrium between the SLM element and clutch can be written as

$$k_l x_{sub} + k_a\left(x_{sub} + x_\eta\right) = k_{clutch} \sum_{i=0}^{n_c} (x_{clutch,i} - x_{sub}). \quad \text{Eq 10}$$

Where k_l is the long-term stiffness in the SLM and n_c is the number of engaged clutches. The summation term on the right-hand side will depend on the probability of the clutch binding to the substrate $F_{clutch} = k_{clutch} n_c P_B (x_{clutch} - x_{sub})$ where x_{clutch} is the position of the clutch, hence

$$k_l x_{sub} + k_a\left(x_{sub} + x_\eta\right) = k_{clutch} n_c P_B (x_c - x_{sub}). \quad \text{Eq 11}$$

Where, P_B is the probability of the clutch binding. It is calculated in each time step by sampling from continuous uniform distribution as defined in the previous section i.e. $t_{bind/unbind} = \frac{-\log\left(URN\left(n_{ceng/cdiseng}\right)\right)}{r_{on/off}}$. Eq. 11 can be rearranged to give,

$$x_s = \frac{k_{clutch} n_c P_B x_{clutch} + x_\eta}{k_l + k_{clutch} n_c P_B + k_a}, \quad \text{Eq 12}$$

it is possible to solve for x_η by substituting Eq.12 into Eq.9,

$$\eta \frac{dx_\eta}{dt} = k_a \left(\frac{k_{clutch} n_c P_B x_{clutch} + x_\eta}{k_l + k_{clutch} n_c P_B + k_a} - x_\eta \right). \quad \text{Eq 13}$$

The KMC is initialized by setting the initial displacement in the SLM element and clutches to zero. Hence, x_η can be solved numerically by taking the forward difference j for each time step dt. Therefore, x_η can be written as

$$x_\eta = \begin{cases} \dfrac{a_1 k_{clutch} \sum_{i=0}^{n_c} x_{clutch,i}}{k_a - a_1 k_a + a_2}, & j = 0 \\ \dfrac{a_1 k_{clutch} \sum_{i=0}^{n_c} x_{clutch,i} + a_2 x_\eta (j-1)}{k_a - a_1 k_a + a_2}, & j > 0 \end{cases} \quad \text{Eq 14}$$

where $x_\eta(j-1)$ is the position of the dashpot in the previous time step a_1 and a_2 are defined as

$$a_1 = \frac{k_a}{k_l + k_{clutch} n_c P_B + k_a} \; and \; a_2 = \frac{\eta}{dt}.$$

Using the force balance between the clutch and SLM element the substrate position can be calculated for each time step

$$x_{sub} = \frac{k_{clutch} \sum_{i=0}^{n_c} x_{clutch,i} + k_a x_\eta}{n_c k_{clutch} + k_l + k_a}. \quad \text{Eq 15}$$

From x_{sub} it is possible to calculate the total force in the system (F_s) by

$$F_s = F_{SLM} = F_{clutch} = k_{clutch} \sum_{i=0}^{n_c} (x_{clutch,i} - x_{sub}). \quad \text{Eq 16}$$

From the position of the substrate, it is possible to update the force and therefore the velocity of the actin filament (v_f) using Eq.4 in the previous section (2.11.1). The simulations were computed in the same way as outlined in 2.11.1. Briefly, 10,000 events were computed with a time step of 5 ms. Each simulation was repeated 100 times to yield the mean behaviour. General model parameters are discussed in section 2.11.3 and a characteristic length scale of focal adhesions was selected to be 1 μm meaning that 1 kPa = 1 pN/nm.

2.11.3. Motor clutch parameters

In this thesis, I used the motor clutch parameters that were reported by Chan and Odde (2008) that were optimized for embryonic chick forebrain growth cones. I used the parameters reported by Gong et al. (2018) for the threshold reinforcement force (F_{cr}) and reinforcement rate (α) that were optimize for Human bone marrow derived MSCs. Gong et al. (2018) noted

that the reinforcement rate (α) is not very sensitive for the model. Therefore, the threshold reinforcement force (F_{cr}) could have been a source of error in the simulations presented in this thesis. In future work, the threshold reinforcement force should be calculated experimentally using the methods presented by Elosegui-Artola et al. (2016). There is some evidence from Athamneh et al. (2015) that Aplysia growth cones have a reinforcement mechanism that is similar to other cell types. Therefore, I included a reinforcement mechanism in the motor clutch simulations presented in this work. Here, I assumed that the model parameters for embryonic chick forebrain growth cones were the same for RGC axons in *Xenopus* and that *Xenopus* RGCs undergo a reinforcement mechanism. Ideally, each model parameter should be optimized for the specific cell type by fitting the motor clutch model to experimental data. As model parameter were not optimized for *Xenopus* RGCs I will qualitatively discuss the impact of model parameter on the simulations in section 5.5.3.

Table 3 General model parameters for elastic and viscoelastic Kinetic Monte Carlo simulations.

Parameter	Description	Value	Reference
n_m	Number of myosin motors	75	Embryonic chick forebrain neurons (Chan and Odde, 2008) and Human bone marrow-derived MSCs (Gong et al., 2018)
F_m	Stall force of myosin motors	2 pN	Chan and Odde, 2008
v_u	Unloaded actin retrograde flow	120 nm/s	Chan and Odde, 2008
n_c	Number of molecular clutches	75	Chan and Odde, 2008
r_{on}^0	Unloaded association rate	1 s^{-1}	Chan and Odde, 2008
r_{off}^0	Unloaded disassociation rate	0.1 s^{-1}	Chan and Odde, 2008
F_b	Molecular clutch breakage force	2 pN	Chan and Odde, 2008
k_c	Molecular clutch stiffness	5 pN/nm	Chan and Odde, 2008
F_{cr}	Threshold reinforcement force	3 pN	Gong et al., 2018
α	Reinforcement rate	0.2 pN^{-1}	Gong et al., 2018

2.12. Data analysis

2.12.1. Software

Figures were prepared using the latest version of Adobe Photoshop and Illustrator Creative Cloud. ImageJ FIJI (version 2.1.0/1.53c, open-source) was used for handling microscopy images. Python (v.3.8) was used for all statistical analysis and preparing plots. Mathematica (version 12.2) was used for solving equations symbolically.

2.12.2. AFM and motor clutch python package

A large part of my PhD focused on developing the mathematics and analysis workflow for obtaining viscoelastic parameters of the substrate in question according to a variety of

mechanical models. Much of the workflow for different mechanical models was replicated and only the governing equations needed to be updated. For that reason, I created a python library that makes it easy to load, pre-process, and analyse AFM data according to different viscoelastic models and visualize the results. The code runs on Python 3.8 and is available on GitHub https://github.com/rg314/pyforce. Table 4 summarizes the different models that can be fitted using the Python package and their corresponding mechanical parameters. Please refer to the results section (3.2) where I report the analytical solutions for the Maxwell, Voigt, and SLM models.

Table 4 Parameters obtained from AFM creep experiment and corresponding model.
k is the elastic stiffness according to the Hertz model. $k_{Maxwell}$ is the elastic stiffness according to the Maxwell model. $\eta_{Maxwell}$ is the viscosity according to the Maxwell model. k_{Voigt} is the elastic stiffness according to the Voigt model. η_{Voigt} is the viscosity according to the Voigt model. τ_{Voigt} is the characteristic time-scale according to the Voigt model. k_l is the long term elastic stiffness according to the SLM model (i.e. the stiffness at long timescales). k_a is the additional elastic stiffness according to the SLM model (i.e. the stiffness at short timescales). η is the viscosity according to the SLM model. k_0 is the elastic stiffness at time zero according to a PLR model. β is the fluidity parameter according to a PLR model and describes the viscosity.

Model	Parameters
Hertz	k
Maxwell	$k_{Maxwell}, \eta_{Maxwell}$
Voigt	$k_{Voigt}, \eta_{Voigt}, \tau_{Voigt}$
SLM	$k_l, k_a, \eta, \tau_{slm}$
PLR/FCFM (Schierbaum et al., 2019)	k_0, β

2.12.3. Traction force microscopy analysis

Several different traction force microscopy packages exist in ImageJ (FIJI) and MatLab. However, many of these packages require the user to have a deep understanding of several parameters that determine the final force or stress fields. Subsequently, it can be challenging to analyse traction force data despite it being relatively simple to perform experimentally. For that reason, I developed a custom piece of software for analysis of traction force data without the need tune hyperparameters. The software was also written in Python a modern and

opensource programming language along with examples showing users how to work through different cases. The TFM analysis package was implemented based on the work presented by Huang et al. (2020). Based on the methods from Huang et al. (2020) the substrate was assumed to be a homogeneous, isotropic, linearly elastic semi-infinite half space. The continuous displacement field was assumed to be acting across the whole substrate surface and forces are applied parallel to the surface and there are negligible traction forces normal to the substrate surface. The code runs on Python 3.8 and is available on GitHub https://github.com/rg314/pytraction.

2.12.4. Axon and growth cone velocity analysis

Axon and growth cone velocities were calculated according to the methodology reported by Koser et al. (2016). The axon velocity was calculated by

$$v_{\text{axon}} = \frac{|\overrightarrow{p_0} - \overrightarrow{p_n}|}{t}, \qquad \text{Eq 17}$$

where $\overrightarrow{p_0}$ is the starting position of the axon and $\overrightarrow{p_n}$ is the ending position of the axon and t is the total time elapsed during imaging. The growth cone velocity was calculated by measuring the absolute path of the growth cone during the imaging period

$$v_{gc} = \frac{\sum_{i=0}^{n} |\overrightarrow{p_i} - \overrightarrow{p_{i-1}}|}{t}, \qquad \text{Eq 18}$$

where $\overrightarrow{p_i}$ is the position of the growth cone at the ith frame. The velocities were calculated for force generating growth cones during TFM experiments as outlined in section 2.12.4. Therefore, the imaging interval was every 5 minutes for at least 1 hour.

2.12.5. Actin and microtubule kymograph analysis

After imaging actin and microtubule dynamics using LifeAct and EB3, respectively, 2 channel time-lapse data was obtained. To measure the velocities of the cytoskeletal components, 2 channel images were split into the respective channels for LifeAct and EB3. Using the single channel time-lapse image, the ‘Analyse>Multiple Kymograph>StackDifference’ function in FIJI was used to generate tracks, that is where pixels move in space and time. Tracks were traced using the segment line tool and added to the ROI manager. For each trace, the ‘Analyse>Multiple Kymograph>Multiple Kymograph’ function was used to generate kymographs. For each kymograph, the segment line tool was used to trace the tracks in the kymograph and saved using the FIJI ROI manager as zip files. ROI files were read into python

using the read-roi library (pip, v1.6.0) and slopes of the lines were calculated to obtain the velocities of the cytoskeletal components.

2.12.6. Sholl analysis

Sholl analysis was performed using the 'Sholl Analysis' plugin on FIJI (https://imagej.net/plugins/sholl-analysis). Before, the plugin was used images were filtered via a FFT bandpass filter to correct for uneven background illumination and thresholded. Often debris occurred in the image after thresholding which needed to be removed by Photoshop manually. A circle was fitted to the eye primordia and the outer radius was set as the starting point for the Sholl analysis plugin. The outer point was set greater than the image dimensions to ensure that all axons were captured in the analysis. Concentric circles were drawn with 5 μm spacings for the analysis. The data shown here is the median axon length radius from the Sholl analysis curve. To automate this process, I trained a convolutional neural network that could perform semantic segmentation and used scyjava to create Python to Java bindings to perform the Sholl analysis on FIJI headless. The code runs on Python 3.8 and is available on GitHub https://github.com/rg314/autoballs.

2.12.7. Statistics

All experiments were performed on at least three biological replicates and as many technical replicates as reasonably possible. A Shapiro-Wilk Test was used to test for normality of the underlying data. For data that followed a normal distribution, a two-tailed one or two sample t-test was used. For data that was not normally distributed a Mann-Whitney test was used for between-groups comparisons and with Bonferroni correction for multiple comparisons. All statistical tests were performed using statannotations (v0.4.2) which uses statsmodels (v0.12.2) to calculate underlying statistics.

Chapter 3: Measuring viscoelasticity in biological tissues

3.1. Background

Over the last decade it has become established that elasticity is important in regulating cellular behaviour in a number of different contexts (Guimarães et al., 2020). Tissue elasticity can be measured *in situ* using several different methods including AFM, optical/magnetic tweezers, and others (Sugimura et al., 2016). Koser et al. (2016) and Thompson et al. (2019) demonstrated that *in vivo Xenopus* brain tissue elasticity can be measured during development. However, tissue is not purely elastic but also exhibits a viscous component. In this chapter, I focus on how AFM can be used to measure tissue viscoelasticity and measure the viscoelasticity of the developing intact *Xenopus* brain.

3.2. A theoretical introduction to measuring viscoelasticity using AFM

Previous efforts in the group have focused on measuring tissue elasticity. To determine the true mechanics of tissues both the elastic and viscous constants must be determined. Therefore, to measure the viscoelasticity of biological tissues I developed a technique using AFM. For an elastic solid and spherical indenter, the contact mechanics can be described using the Hertz model

$$F = \frac{4}{3}\frac{E}{1-v^2}R^{1/2}\delta^{3/2} = \frac{4}{3}kR^{1/2}\delta^{3/2}, \qquad \text{Eq 19}$$

here E is the elastic modulus of the sample, v is Poisson's ratio (which describes the proportional decrease in a horizontal measurement to the proportional increase in length), R is the radius of the indenter, δ is the indentation depth, and k is the reduced apparent stiffness ($k = E/(1-v^2)$). Therefore, the Hertz model can be fitted to AFM force vs indentation curves to determine the reduced apparent stiffness or elastic modulus (note that the apparent stiffness k can be derived without knowing the Poisson's ratio (v)). However, biological tissues are viscoelastic materials, comprising both of an elastic and viscous component. During an AFM creep experiment using a spherical indenter, the indentation is related to the creep compliance by the following Volterra integral

$$\delta(t)^{3/2} = \frac{3}{4}r^{-1/2}\int_0^t J(t-t')\frac{dF(t')}{dt'}dt'. \qquad \text{Eq 20}$$

Eq.20 is only valid for a monotonic increase in indentation limiting its application to the approach and constant force segments of the AFM curve (Schierbaum et al., 2019). According to Eq.20 the indentation depth also depends on the force history ($dF(t')/dt$) before the creep measurement begins, that is when a constant force is maintained. Schierbaum et al. (2019) reported that the force ramp can be modelled using a piecewise polynomial function:

$$F(t) = F_{clamp} \begin{cases} 0, & t < t_c \\ \left(\frac{t - t_c}{\Delta t_A}\right)^{\alpha}, & t_c \leq t < t_c + \Delta t_A \\ 1, & \Delta t_A + t_c \leq t \end{cases} \quad \text{Eq 21}$$

where F_{clamp} is the constant force applied during the creep measurement, t_c is the contact time, Δt_A is the time to ramp the force from the baseline to F_{clamp}, and α is a free parameter describing the shape of the force ramp ($1 < \alpha < 2$). Therefore, to measure the creep response of difference materials a creep compliance function $J(t)$ needs to be derived for a specific viscoelastic model and solve Eq. 20. Creep is the strain response to a constant stress and recovery is the stress response to a constant strain. Viscoelastic models are formalized using a spring element (elastic: $\sigma = E\epsilon$ or $F = -kx$) and a dashpot element (viscous: $\sigma = \eta\, d\epsilon/dt$ or $F = -k\frac{dx}{dt}$). Depending on the configuration of these elements it is possible to model material responses for constant stresses or strains and extract material constants.

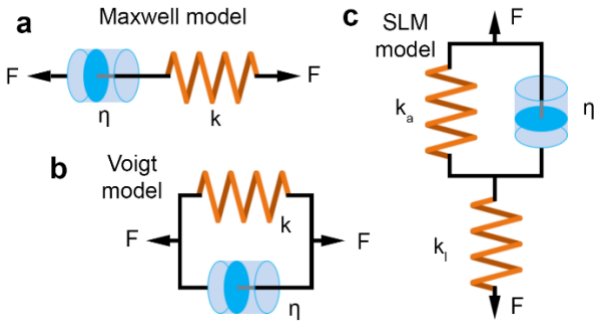

Figure 6 Schematic diagrams of viscoelastic models.

a) Maxwell element configuration consisting of a spring and dashpot in series. B) Voigt element configuration consisting of a spring and dashpot in parallel. C) Standard linear model (SLM) element consisting of a spring in series with a Voigt element.

The configuration of springs and dashpots can give rise to different viscoelastic behaviour, I will introduce the four main models used in this work which are the Maxwell, Voigt, SLM and power-law rheology (PLR) models. First, the Maxwell configuration consists of a spring and dashpot in series (Figure 6a). When subjected to a force, each element will

experience an equal stress ($\sigma = \sigma_1 = \sigma_2$) and additive strain ($\epsilon = \epsilon_1 + \epsilon_2$ and $\dot{\epsilon} = \dot{\epsilon_1} + \dot{\epsilon_2}$). Therefore, it can be written that

$$\frac{d\varepsilon}{dt} = \frac{\sigma}{\eta} + \frac{1}{k}\frac{d\sigma}{dt}. \quad \text{Eq 22}$$

To predict the strain response ($\epsilon(t)$) at a constant stress ($\sigma(t) = \sigma_0$) with the boundary condition $\epsilon(0) = \epsilon_0 = \sigma_0/k$, the solution to the differential equation is

$$\varepsilon(t) = \frac{\sigma_0}{\eta}t + \frac{\sigma_0}{k}. \quad \text{Eq 23}$$

The Maxwell model poorly predicts the strain response for real materials (the strain linearly increases as a function of time). The Voigt model consists of a spring and dashpot in series (Figure 6b). When subjected to a force, each element will experience an additive stress ($\sigma = \sigma_1 + \sigma_2$) and equal strain ($\epsilon = \epsilon_1 = \epsilon_2$). For a constant stress ($\sigma'(t) = 0$ and $\sigma(t) = \sigma_0$) the following first order linear differential equation is obtained

$$\eta\frac{d\varepsilon}{dt} + \mathrm{k}\varepsilon - \sigma_0 = 0, \quad \text{Eq 24}$$

which has the solution

$$\varepsilon(t) = \frac{\sigma_0}{k}\left(1 - \exp\left(-\frac{kt}{\eta}\right)\right). \quad \text{Eq 25}$$

The Voigt model accurately predicts the creep behaviour of materials at long time scales but inaccurately predicts the instantaneous elastic response. The Maxwell and Voigt models can be combined together to yield the SLM that consists of a spring in series with a Voigt element (Figure 6c) which is governed by the following equations

$$\sigma = \sigma_1 + \sigma_2\ ;\ \epsilon = \epsilon_1 + \epsilon_2\ ;\ \sigma = k_l\epsilon_1\ ;\ \sigma_1 = k_a\epsilon_2\ ;\ \sigma_2 = \eta\dot{\epsilon_2}. \quad \text{Eq 26}$$

By taking the Laplace transform $\mathcal{L}\{f\}$ and rearranging,

$$(k_a + k_l)\mathcal{L}\{\sigma\} + \eta s\mathcal{L}\{\sigma\} = k_a k_l\mathcal{L}\{\epsilon\} + k_a\eta s\mathcal{L}\{\epsilon\}, \quad \text{Eq 27}$$

which can be transformed back into the governing SLM equation,

$$(k_a + k_l)\sigma + \eta\dot{\sigma} = k_a E_2\epsilon + k_l\eta\dot{\epsilon}. \quad \text{Eq 28}$$

for a step application of stress $\sigma(t) = \sigma_0 H(t)$ and $\sigma'(t) = \sigma_0\delta(t)$, where $H(t)$ is the Heaviside function and $\delta(t)$ is the Dirac delta function it can be written that,

$$(k_a + k_l)\sigma_0 H(t) + \eta\sigma_0\delta(t) = k_a k_l\epsilon + k_l\eta\dot{\epsilon}, \quad \text{Eq 29}$$

and corresponding Laplace transform,

$$(E_1 + E_2)\sigma_0/s + \eta\sigma_0 = E_1E_2\mathcal{L}\{\epsilon\} + E_1\eta s\mathcal{L}\{\epsilon\}. \quad \text{Eq 30}$$

Eq. 30 can an easily be rearranged with respect to $\mathcal{L}\{\epsilon\}$ and then the inverse Laplace transformation yields,

$$\epsilon(t) = \sigma_0 \left(\frac{1}{k_l}\, e^{-\frac{k_l}{\eta}t} + \frac{\eta(k_l + k_a)}{k_a k_l} \left(1 - e^{-\frac{k_l}{\eta}t} \right) \right). \qquad \text{Eq 31}$$

The SLM model accurately predicts the creep behaviour of materials and considers the instantaneous elastic response. The exponent in Eq.25 and Eq.31 contains a characteristic time scale ($\tau = E/\eta$) that explains how stresses decay. Creep compliance ($J(t)$) describes the rate at which the strain increases for a constant stress (σ_0) and is related to the strain by $J(t) = \epsilon(t)/\sigma_0$.

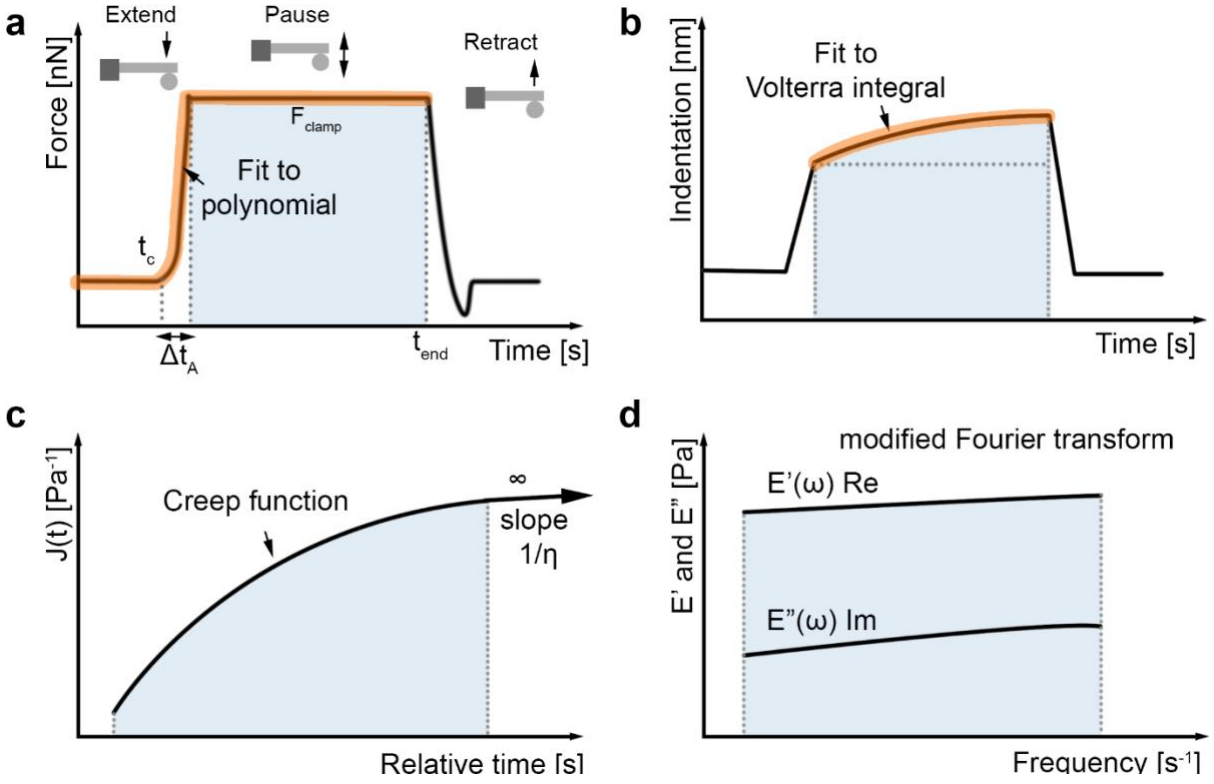

Figure 7 Fitting AFM creep measurements to viscoelastic models.

a) The cantilever is extended and contacts the surface at t_c until the force clamp setpoint is reached after Δt_A. Here, the force clamp is maintained for 3s and then the cantilever is retracted. B) For $t > t_c$ the AFM tip indents into the sample until the force setpoint (F_{clamp}). When the tissue is viscoelastic, deformation occurs, and further indentation is required to maintain the force setpoint. In the case the material is purely elastic the indentation would remain constant as illustrated by the horizontal dotted line. C) Indentation data for $t > t_c + \Delta t_A$ is transformed into creep compliance using and the steady state viscosity (η) is extrapolated by fitting the last 10 % of data. Maxwell, Voigt, SLM, and power models can be fitted to the creep compliance to determine theoretical material constants. D) The storage and loss modulus are recovered by taking a modified Fourier transform of the creep compliance between w_{min} ($\sim t_n^{-1}$) and w_{max} ($\sim t_1^{-1}$).

Despite the accuracy of the SLM model it assumes that relaxation occurs at a single timescale (τ). However, relaxation and deformation can occur at a set of discrete times scales (τ_i) that correspond to molecular segments with varying lengths. The generalized Maxwell or generalized Voigt models address this issue by assembling *N* Maxwell or Voigt configurations in parallel, respectively. Implementation of these models leads to a relaxation time distribution

$P(\tau_i)$. Tissues and cells are essentially a complex network of molecular segments, spanning length scales from micrometres to nanometres. It is reasonable to assume that the length scale (l) of these segments are distributed according to a power law, l^{-d} for $d > 0$ where d is the fractal dimension. Correspondingly, it would be expected that the characteristic time scales of the molecular segments would also follow a power law ($\tau_i \propto l_i^{\beta}$) and their distribution ($P(\tau_i) \propto \tau_i^{d/\beta-1}$). Balland et al. (2006) demonstrated that the corresponding creep compliance also follows a power law as a function of time

$$J(t) = k_0 \left(\frac{t}{t_0}\right)^{\beta}, \qquad \text{Eq 32}$$

where β describes the fluidity ($0 < \beta < 1$), k_0 is the stiffness at t_0, and $t_0 > 0$. For $\beta = 0, J(t) = k_0$ and hence would behave as an elastic solid. For $\beta = 1, J(t) \propto k_0 t$ exhibiting fluid behaviour. Returning to our Volterra integral (Eq. 20), the power law rheology (PLR) model can be substituted into the creep term ($J(t)$, Eq. 32) and use Eq. 21 for the force history (Schierbaum et al., 2019). By performing a piecewise integration, we arrive at

$$\delta(t) = \left[\frac{3}{4}\frac{1}{k_0\sqrt{R}}\frac{\alpha\,(t-t_c)^{\alpha+\beta}}{\Delta t_A^{\alpha} t_0^{\beta}} B\left(\frac{\Delta t_A}{t-t_c}; \alpha,\, \beta+1\right)\right]^{2/3}, \qquad \text{Eq 33}$$

where $B(x: \alpha, \beta)$ is the incomplete beta function. By fitting Eq.33, it is possible to extract the fluidity parameter (β) and the apparent modulus at $t = 0$ (k_0) to describe the viscoelastic properties of the material. Eq.33 can be used to obtain force clamp force maps.

However, this method does not consider the frequency-dependent behaviour of viscoelastic materials. The frequency dependent behaviour of viscoelastic materials is measured in terms of the complex modulus, $G^*(\omega)$. It has previously been reported that the cellular machinery responsible for exerting forces on substrates occurs on the time scales of ~ 10 s (< 1 Hz) (Charrier et al., 2018). Obtaining frequency maps of the *Xenopus* brain using AFM is time consuming since a frequency spectrum must be obtained at each pixel. The creep experiment obtains information in the time domain and hence the frequency dependency should be retrievable by a Fourier transform of the creep compliance

$$G^*(\omega) = G'(\omega) + iG''(\omega) = \frac{1}{i\omega \dot{J}(\omega)} \qquad \text{Eq 34}$$

where

$$\dot{J}(\omega) = \mathcal{F}[J](\omega) = \int_{-\infty}^{\infty} J(t) e^{-i\omega t} dt. \qquad \text{Eq 35}$$

The creep compliance is a divergent integral and it is not possible to take the Fourier transform. Evans et al. (2009) established a simple approach to convert creep compliance data into the frequency domain to obtain the complex modulus using a modified Fourier transform with the following equation

$$\frac{i\omega}{G^*(\omega)} = i\omega J_0 + \left(1 - e^{-i\omega t_1}\right)\frac{J_1 - J_0}{t_1} + \frac{e^{i\omega t_N}}{\eta} + \sum_{k=2}^{N}\left(\frac{J_k - J_{k-1}}{t_k - t_{k-1}}\right)\left(e^{-i\omega t_{k-1}} - e^{-i\omega t_k}\right). \quad \text{Eq 36}$$

Where J_0 is the creep compliance at $t = 0$ and η is the steady state viscosity that is extrapolated from $J(t)$ as $t \to \infty$. The spectral bandwidth is constrained by the resolution of the AFM and the length of the creep experiment, that is $w_{min} = t_n^{-1}$ and $w_{max} = t_1^{-1}$. For a spherical indenter the creep compliance is defined as

$$\delta(t)^{3/2} = \frac{3}{4\sqrt{R}}\int_0^t J(t - t')\frac{dF(t')}{dt'}dt'. \quad \text{Eq 37}$$

Thus, the creep compliance should be recovered by taking the derivative of both sides

$$\frac{d}{dt}\left[\delta(t)^{\frac{3}{2}}\right] = \frac{3}{4\sqrt{R}}\frac{dF(t')}{dt'}J(t). \quad \text{Eq 38}$$

Taking the derivative of such noisy experimental AFM data leads to large oscillations. Even when sophisticated smoothing algorithms (i.e. total-variation regularization (Chartrand, 2011)) are used, the indentation and force derivative are divided that still results in large oscillations. To obtain the frequency-dependent behaviour, I needed to approximate the creep compliance function which could be done by using the analytical solution as per a viscoelastic model. Then it is possible to use Eq. 36 or directly Fourier transform the analytical solution for the creep compliance to obtain the storage and loss modulus. I found that the SLM model fitted the indentation data the best (refer to section 3.4 for further details) and for that reason I took the Fourier transform of the SLM parameters to obtain the storage and loss moduli, which had the following analytical form

$$G^* = \frac{\eta i\omega k_a \eta}{\eta + k_a \eta i\omega} + k_l,$$

where $\omega = 0.1$ Hz. A frequency of 0.1 Hz was chosen as cells probe their surrounding environment in the frequency range of 0.1 – 1 Hz (Charrier et al., 2018). To be able to fit the indentation curves using different viscoelastic models, I needed to solve Eq. 20 by substituting the appropriate creep compliance function and polynomial force ramp (Eq. 21). Table 5 shows the different creep functions according to the Maxwell, SLM, Voigt, and PLR that I wanted to

solve Eq. 20 for to obtain the viscoelastic parameters. Furthermore, Figure 8 shows the typical behaviour of these functions over an arbitrary time with fixed constants illustrating how different models predict different behaviour. In the following section, I will derive the analytical solutions for the equations summarised in Table 5 if it has not already been provided in literature.

Table 5 Summary of creep compliance functions to solve analytically.

Model name	Creep compliance function
Maxwell	$J(t) = \frac{1}{\eta}t + \frac{1}{k}$
SLM	$J(t) = \frac{1}{k_l + k_a} + \left(\frac{1}{k_l} - \frac{1}{k_l + k_a}\right)\left(1 - e^{-t\frac{k_l k_a}{\eta(k_l + k_a)}}\right)$
Voigt	$J(t) = \frac{1}{k}\left(1 - \exp\left(-\frac{kt}{\eta}\right)\right)$
PLR	$J(t) = k_0\left(\frac{t}{t_0}\right)^{\beta}$

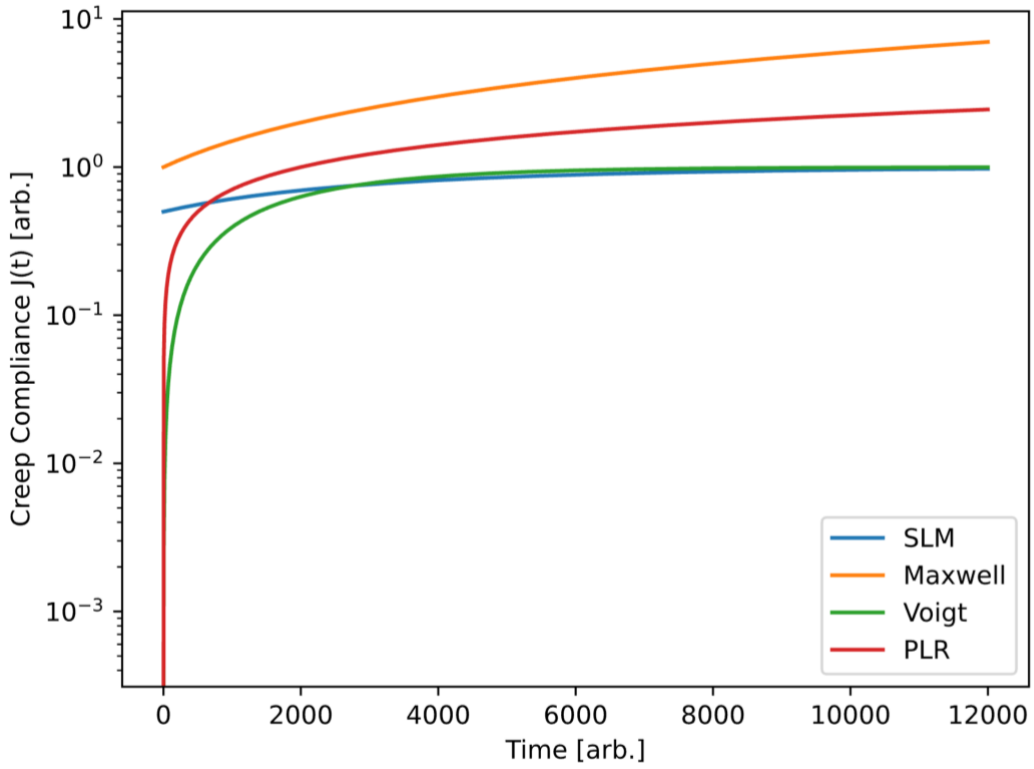

Figure 8 The viscoelastic response of a material depends on the model that is used to explain its behaviour.

Creep compliance response of viscoelastic models outlined in Table 5. SLM and Maxwell models have an instantaneous elastic response while Voigt and PLR models rapidly deform. All models exhibit creep behaviour but at different rates. Maxwell ($k = 1, \eta = 1[arb.]$), SLM ($k_a = 1, k_l = 1, \eta = 1\ [arb.]$), Voigt ($k = 1, \eta = 1[arb.]$), and PLR ($k_0 = 1, \beta = 0.5\ [arb.]$). All models were plotted with arbitrary units as a function of time.

3.2.1. Analytical solutions for creep compliance functions

To be able to fit raw AFM data to different viscoelastic models and obtain the elastic and viscous constants, the Volterra integral must be solved analytically for each case. In the following section I solve the Volterra integral analytically for the Maxwell, SLM, and Voigt models which can then be used to fit raw AFM indentation time ($\delta(t)$) data.

3.2.1.1. Analytical solution Maxwell model

The Maxwell model is easy to solve. If Eq. 20 and Eq. 21 are combined with the Maxwell creep compliance function

$$\delta(t)^{3/2} = \frac{3}{4} r^{-1/2} \frac{\alpha F_{clamp}}{\Delta t_a} \int_0^{\Delta t_a} \left(\frac{1}{\eta}(t - t') + \frac{1}{k}\right) \left(\frac{t'}{\Delta t_A}\right)^{\alpha - 1} dt'. \qquad \text{Eq 39}$$

Which gives the following result

$$\delta(t) = \left[\frac{3}{4} r^{-\frac{1}{2}} \frac{\alpha F_{clamp}}{\Delta t_a} \left(\frac{1}{k} - \frac{\alpha \Delta t_A}{\eta + \alpha\eta} + \frac{t}{\eta}\right)\right]^{2/3} \quad \text{Eq 40}$$

3.2.1.2. Standard linear model

To simplify the SLM equation, $C_0 = \frac{1}{k_l + k_a}$, $C_1 = \frac{1}{k_l}$, and $C_2 = \frac{k_l k_a}{\eta(k_l + k_a)}$ can be substituted to give

$$J(t) = C_0 + (C_1 - C_0)(1 - e^{-tc_2}). \quad \text{Eq 41}$$

Then if Eq. 20 and Eq. 21 are combined with the SLM creep compliance function and since the force derivative ($F'(t')$) at $t < t_c$ and $\Delta t_A + t_c \leq t$ is zero the following integral is obtained

$$\delta(t)^{3/2} = \frac{3}{4} r^{-1/2} \frac{\alpha F_{clamp}}{\Delta t_a} \int_0^{\Delta t_a} \Big(C_0 + (C_1 - C_0)\big(1 - e^{-(t-t')c_2}\big)\Big)\left(\frac{t'}{\Delta t_A}\right)^{\alpha - 1} dt'. \quad \text{Eq 42}$$

Hence, there are two integrals to solve with the general form

$$I_1 = \int_0^t e^{-ct} t^{\alpha - 1}\, dt \;\; and \; I_2 = \int_0^t t^{\alpha - 1}\, dt. \quad \text{Eq 43}$$

The second integral (I_2) is easy to solve, yet the first integral (I_1) is hard to solve. By inspection, the first integral has the form of an incomplete gamma function

$$I_1 = \alpha t^{\alpha} (-ct)^{-1} \big(\Gamma(\alpha) - \Gamma(\alpha, ct)\big). \quad \text{Eq 44}$$

The incomplete gamma function returns a complex number which is not a valid solution for the problem. The gamma function can also be related to the hypergeometric function (${}_1F_1$) of the first kind

$$\Gamma(\alpha, x) = \alpha^{-1} x^{\alpha}\, {}_1F_1(\alpha, 1 + \alpha, -x). \quad \text{Eq 45}$$

Therefore, through the confluent hypergeometric function identity the complex component is cancelled out which results in the following general solution

$$I_1 = e^{ct} t^{\alpha}\, {}_1F_1(\alpha, \alpha + 1, t). \quad \text{Eq 46}$$

By using the above solution, the result of the integral is as followed

$$\delta(t) = \left[\frac{3}{4}\frac{F_{clamp}}{\sqrt{r}}\alpha^{1-\alpha}\Delta t_a^{\alpha-1}\left(C_0 + (C_0 - C_1)\, e^{-tC_2}{}_1F_1(\alpha, \alpha + 1, \Delta t_a C_2)\right)\right]^{2/3} \quad \text{Eq 47}$$

3.2.1.3. Voigt model

To simplify the Voigt equation $C_0 = \frac{1}{k}$, and $C_1 = \frac{k}{\eta}$ can be substituted into the creep compliance function to give

$$J(t) = C_0(1 - e^{-tc_1}) \quad \text{Eq 48}$$

Then if Eq. 20 and Eq. 21 are combined with the Voigt creep compliance function and since the force derivative ($F'(t')$) at $t < t_c$ and $\Delta t_A + t_c \leq t$ is zero the following integral is obtained

$$\delta(t)^{3/2} = \frac{3}{4}r^{-1/2}\int_0^{\Delta t_a} C_0(1 - e^{-tc_1})\frac{\alpha F_{clamp}}{\Delta t_a}\left(\frac{t'}{\Delta t_A}\right)^{\alpha-1} dt'. \quad \text{Eq 49}$$

Which can be solved by using the same analysis in 3.2.1.2 with the hypergeometric function

$$\delta(t) = \left[\frac{3}{4}\frac{F_{clamp}}{\sqrt{r}}C_0(1 - e^{-tC_1}{}_1F_1(\alpha, \alpha + 1, \Delta t_a C_1))\right]^{2/3} \quad \text{Eq 50}$$

3.3. Measuring viscoelasticity using AFM

To be able to measure the viscoelastic properties of brain tissue, I first had to formulate the mathematics and analysis to make this possible. During an AFM experiment, the cantilever is lowered towards the sample and indented until a target set point is reached. In an ideal case, this set point would be reached instantaneously as shown in Figure 9a. At $t = 0$ the force is already at the maximum and there will be an instantaneous elastic response followed by creep (Figure 9b). The viscoelastic model (Maxwell, Voigt, SLM, or PLR) determines the indentation response to a constant force. However, due to the time-dependent behaviour of viscoelastic materials the force history is important when modelling the indentation response. In experimental conditions, the AFM cantilever cannot apply an instantaneous force to the substrate, and it takes some time (Δt_A) to reach the setpoint. For that reason, I had to consider the force history of the substrate by using the Volterra integral for viscoelastic bodies ($C\int_0^t J(t - t')F'(t')\ dt'$), which I provide the analytical solutions for the Maxwell, SLM, and Voigt models in sections 3.2.1.1 to 3.2.1.3 which, to the best of my knowledge, have not been

reported to date for a polynomial force ramp. It's noteworthy to mention that Hecht et al. (2015) solved the Volterra integral for the PLR case.

In Figure 9c, a linear time ramp over 1 second ($\Delta t_A = 1$ and $\alpha = 1$) is shown and the corresponding viscoelastic response for Maxwell, Voigt, SLM and PLR models. The red dashed line shows the time whereby the maximum force is reached in Figure 9c-d. A deeper understanding of each of the function can be obtained by inspection. For the Maxwell model (3.2.1.1), the indentation is linearly proportional to time ($\delta(t) \propto t$) which is generally a poor approximation of viscoelasticity. The Voigt and SLM models exhibit indentation that is exponentially proportional to time ($\delta(t) \propto e^{-tC_2}$). From inspection it can also be deduced that $\delta(t) \geq 0$. For the SLM solution, Eq. 48 can be rewritten in a simpler form of $[C_0 + (C_0 - C_1)\, e^{-tC_2}\, {}_1F_1(\alpha, \alpha + 1, \Delta t_a C_2)]^{2/3}$ if the prefactor is omitted and at $t = 0$ and $C_1 > C_0$ then

$$C_0 + (C_0 - C_1)\, B < 0 \;\Rightarrow \delta(t) < 0, \qquad \text{Eq 51}$$

where $B = {}_1F_1(\alpha, \alpha + 1, \Delta t_a C_2)$ and $B > 1$ for $\Delta t_a C_2 > 0$. Therefore, the following boundary condition must be satisfied for the SLM model to be valid for $t \leq \Delta t_A$

$${}_1F_1(\alpha, \alpha + 1, \Delta t_a C_2) \leq \frac{-C_0}{C_0 - C_1}. \qquad \text{Eq 52}$$

It is also possible to prove that the Voigt model is invalid for $t \leq \Delta t_A$. If a similar analysis for the Voigt model is applied, Eq. 51 can be rewritten as $[C_0(1 - e^{-tC_2}\, {}_1F_1(\alpha, \alpha + 1, \Delta t_a C_1)]^{2/3}$ and if the prefactor is omitted the following boundary condition holds

$${}_1F_1(\alpha, \alpha + 1, \Delta t_a C_1) \leq 1, \qquad \text{Eq 53}$$

since ${}_1F_1(a, b, z)$ has the range $1 < {}_1F_1(a, b, z) < \infty$ for $z > 0$ and hence it can be concluded that the indentation for the Voigt model is not valid for $t \leq \Delta t_A$.

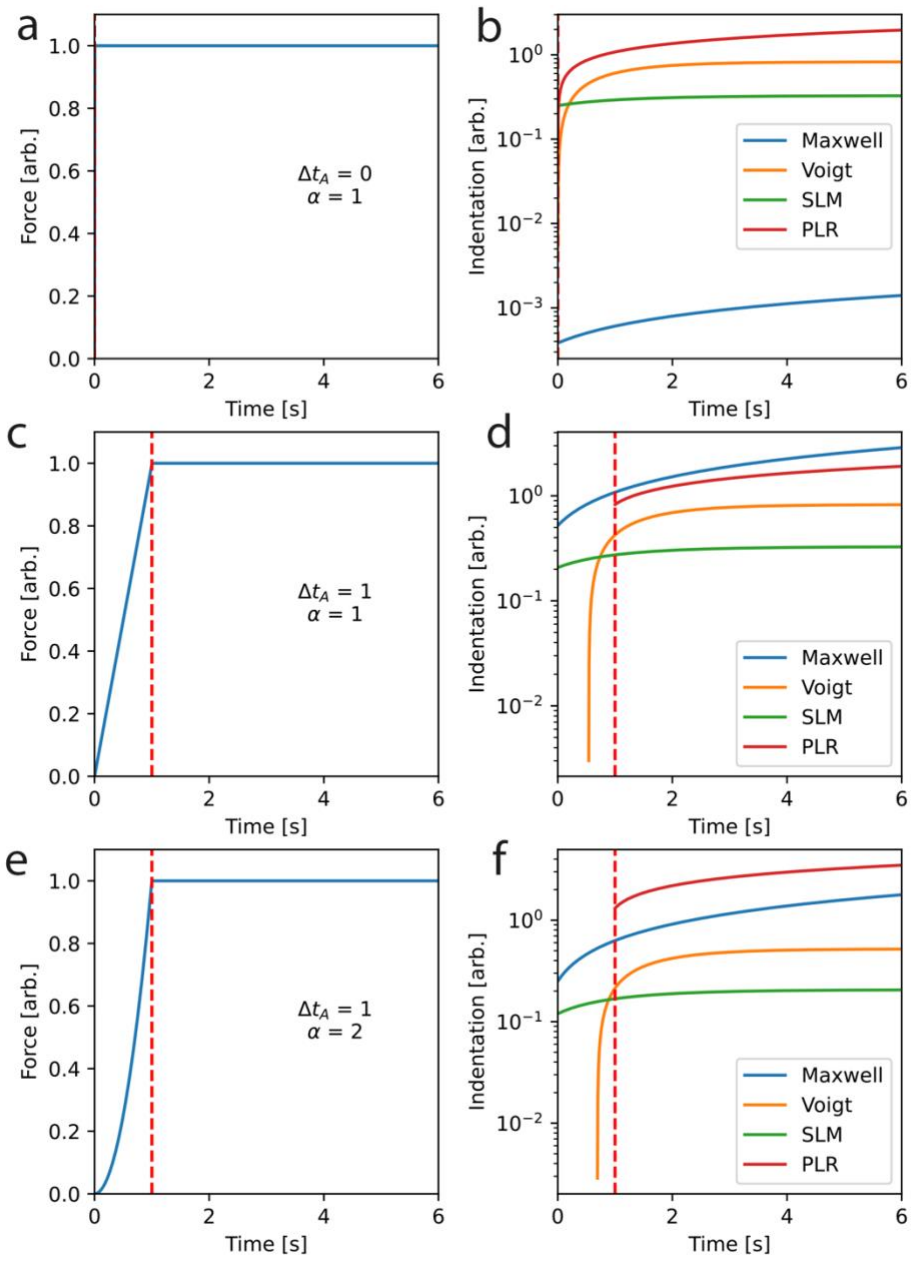

Figure 9 Response of viscoelastic models to different force ramps.

a) an instantaneous application of force and corresponding b) indentation, c) linear force ramp (first-degree polynomial) and corresponding d) indentation, and e) non-linear force ramp (second-degree polynomial) and corresponding f) indentation. Maxwell model parameters; $k = 1$ *and* $\eta = 1$*, Voigt model parameters;* $k = 1$ *and* $\eta = 1$*, SLM model parameters;* $k_a = 1$*,* $k_l = 3$*, and* $\eta = 1$*, and PLR parameters* $k_0 = 1$ *and* $\beta = 1$*. The red dashed line indicates the constant force regime.*

Figure 9c shows that the PLR model has no solutions for $t \leq \Delta t_A$. This is because the incomplete beta function $B\left(\frac{\Delta t_A}{t}; \alpha, \beta + 1\right)$ cannot be evaluated for $t < \Delta t_A$ since $\frac{\Delta t_A}{t} > 1$ and

$B(x, a, b)$ is only valid for $0 \leq x \leq 1$. Figure 9e shows a non-linear force ramp (second-degree polynomial) and the corresponding indentation response (Figure 9f). Solving each of the models for the general polynomial force ramp makes it possible to use the α parameter to model different force ramps from AFM experiments and subsequently fit different viscoelastic models to indentation curves.

In the current section (3.3), I have provided the theoretical framework to analyse the viscoelasticity of substrates in AFM creep experiments. In the following section, I will apply this to experimental data on biological tissues and polymer substrates.

3.4. Viscoelasticity of biological tissues and substrates

After developing the theoretical grounding for measuring viscoelasticity using AFM, I wanted to measure the viscoelastic properties of biological tissues. I achieved this by using a custom AFM set-up that had previously been designed in the group (Thompson et al., 2019). To extract the viscoelastic properties, I conducted creep experiments by holding the AFM tip in the tissue at a constant force (10 nN) for different time periods (3 s up to 60 s) and measured the corresponding indentation. By using the analysis explained in the previous sections (3.2 and 3.3), it was possible to measure the viscoelasticity using different viscoelastic models. It is important to note that many different viscoelastic frameworks measure the viscoelasticity. For that reason, I fitted the indentation-time data to several viscoelastic models and measured the quality of the model using the root mean square error (RMSE) on different substrates.

Figure 10 shows the error associated with different viscoelastic models. For the viscoelastic models, the PLR and SLM had a significantly lower RMSE compared to the Voigt model, meaning that they are the most appropriate viscoelastic models to fit to *Xenopus* tissue (Figure 10a). Depending on the mechanical response of a material, a specific viscoelastic model might be more suited to model the stress and strain response. For that reason, I also measured the goodness of fit for rodent tissue and PAA gels. Similar to the mechanical response of the *Xenopus* tissue, I found that the SLM significantly had the lowest RMSE out of the viscoelastic models for rodent tissue and PAA gels respectively (Figure 10b-c).

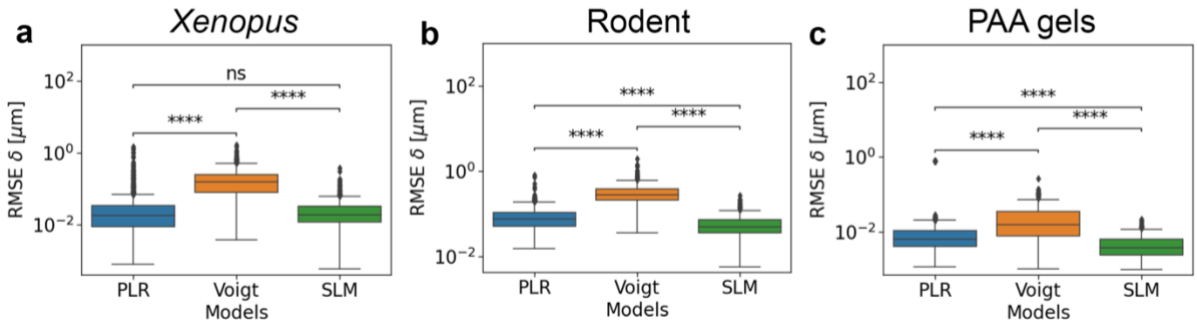

Figure 10 The SLM best models viscoelasticity of biological and synthetic materials.

Goodness of fit for different viscoelastic models. Root-mean-square error of indentation-time curves for PLR, Voigt, and SLM models for a) Xenopus (PLR, N=2281, SLM, N=2205, Voigt= 2271), b) rodent (PLR, N=696, SLM, N=659, Voigt, N=695), and c) PAA gels (PLR, N=340, SLM, N=338, Voigt, N=340). Viscoelastic models were fitted to the indentation-time curves. Mann-Whitney U-test with a Bonferroni correction were used to compare the means. $Ns: p > 0.05$ *and* $****: p \leq 1 \times 10^{-4}$*. The box shows the quartiles (calculated by the interquartile range (IQR)) and the whiskers show the rest of the distribution (1.5 IQR) except for points that are determined to be outliers. Outliers are considered as* $Q \pm 1.5\ IQR$*.*

From analysing the goodness of fit for different viscoelastic models in Figure 10, I found that the SLM was the most appropriate viscoelastic model to use across different tissues and substrate types (*Xenopus*, rodent, and PAA gels). The SLM has several mechanical constants, including k_l, k_a, and η, which can be used to describe the mechanical response. The long-term stiffness (k_l) and additional stiffness (k_a) can be used in combination ($k_l + k_a$) to describe the instantaneous elastic response. That is, when a force of F_0 is applied at t_0 then the displacement in the substrate would be $F_0/(k_a + k_l)$. The long-term stiffness (k_l) can be used to describe the stiffness of the substrate at $\lim_{t\to\infty}$ when a force of F_0 is applied, and hence, the substrate displacement would be $F_0 k_l$. The viscous component η describes how the material creeps from the initial displacement ($F_0/(k_a + k_l)$) to the final displacement (F_0/k_l). Since it can be difficult to interpret all the viscoelastic constants, I decided that it's easier to take the Fourier transform of the SLM model to express the elasticity and viscosity in a single parameter of the storage modulus (G') and loss modulus (G''), respectively.

3.5. Spatial viscoelasticity of *Xenopus* brain

In the previous section (3.4), I demonstrated that it is possible to fit AFM data to a variety of viscoelastic models to retrieve information about substrate elasticity and viscosity. From previous work within the lab, the developing *Xenopus* brain exhibits heterogeneous elasticity,

but there is no information about viscosity. For that reason, I mapped the viscoelasticity of the developing *Xenopus* brain using AFM. The intact *Xenopus* brain was exposed and mounted on an x-y stage underneath the AFM (Figure 11a). At each x-y position, the AFM cantilever was held at a constant force of 10 nN for 3 seconds leading to a constant force hold step (as illustrated in Figure 11b left). During the force hold step the cantilever sank further into the tissue which could be measured with the indentation-time data which is illustrated in Figure 11b right. The corresponding indentation curves were fitted to the SLM model to obtain k_l, k_a, and η. To make the measurements of viscoelasticity more intelligible I converted the SLM model parameters into the storage (G') and loss (G'') modulus.

Figure 11c shows the relationship between the storage and loss modulus in the developing *Xenopus* brain. I found that as the stiffness (storage modulus) increased the viscosity (loss modulus) also increased. Therefore, as the tissue becomes stiffer, that is requiring more energy to be displaced, the tissue is also more resistant to flow. In accordance with previous experiments in the lab (Koser et al., 2016, Thompson et al., 2019), I found that tissue stiffness is heterogeneously distributed within the developing brain as shown in the maps of the storage modulus (G') in Figure 11d. I also found that tissue viscosity is heterogeneously distributed within the brain as shown in the loss modulus (G'') map in Figure 11d. In this work, the tissue viscoelasticity was measured at stage 38/39 when it is expected that the stiffness gradient has developed. To quantify the differences in viscoelasticity in soft and stiff regions of the brain, I compared the storage and loss modulus rostral to the optic tract (denoted by the dotted white oval label with 1 in Figure 11d) the stiffer region of the brain and caudal to the optic tract (denoted by the dotted white oval label with 2 in Figure 11d) the softer region of the brain. The caudle region of the brain ($G' = 28.39 \pm 22.4$ Pa) was significantly softer ($P < 1 \times 10^{-4}$) than the rostral region ($G' = 51.1 \pm 45.87$ Pa). Furthermore, the caudle region of the brain ($G'' = 0.53 \pm 0.35$ Pa) was significantly less viscous ($P < 1 \times 10^{-4}$) than the rostral region ($G'' = 0.79 \pm 0.66$ Pa).

The ratio between the loss and storage modulus, known as the loss tangent ($\tan\delta = G''/G'$), can be used to measure the relative contributions between the elasticity and viscosity. If the loss tangent is above one, then the material is a viscous liquid and if the loss tangent is below one the material is an elastic solid. Closer the loss tangent is to zero more elastic dominant the material is. The caudal region of the brain had a significantly ($P = 1.6 \times 10^{-3}$) higher loss tangent ($\tan\delta = 0.023 \pm 0.01$) compared to the rostral region ($\tan\delta = 0.021 \pm$

0.007). Therefore, the stiffer regions of the brain (rostral of the optic tract) are more elastic compared to softer regions and therefore closer to an elastic solid than a viscous liquid.

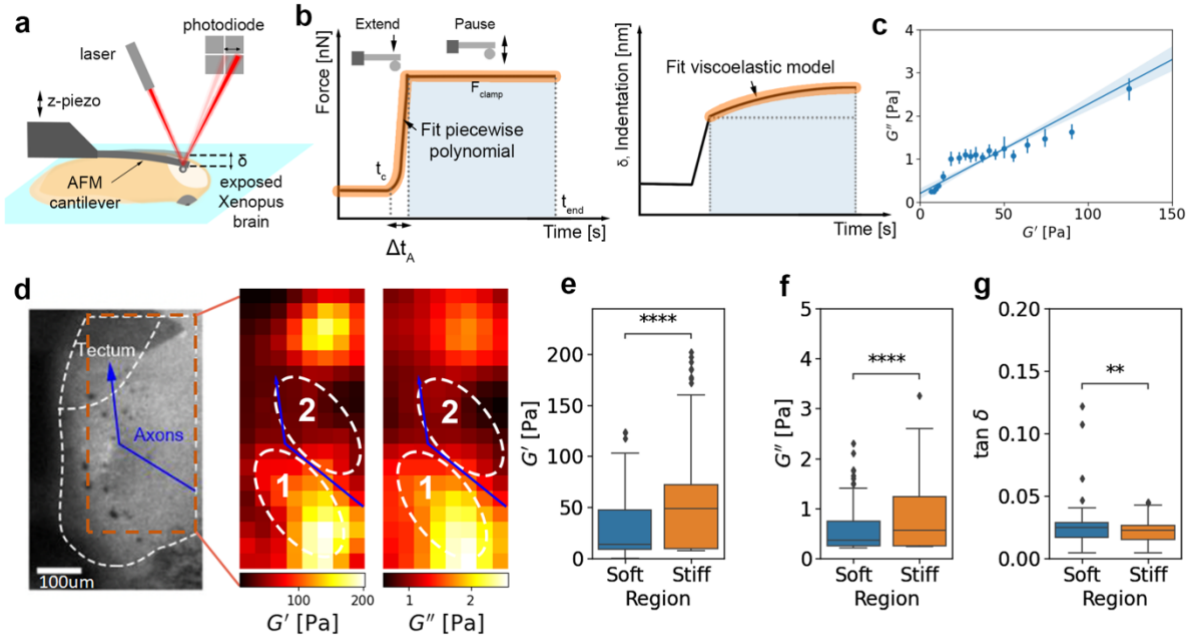

Figure 11 The developing *Xenopus* brain exhibits heterogenous viscoelasticity.

a) Schematic of typical AFM force mapping experiment. Xenopus brain is exposed and z-piezo is used to indent tissue to a predetermined force setpoint. During indentation (δ) the cantilever deflection is monitored using a laser and photodiode. B) The cantilever is extended and contacts the surface at t_c until the force clamp setpoint is reached after Δt_A. Here, the force clamp is maintained for 3s and then the cantilever is retracted. For $t > t_c$ the AFM tip indents into the sample until the force setpoint (F_{clamp}). When the tissue is viscoelastic, deformation occurs, and further indentation is required to maintain the force setpoint. In the case the material is purely elastic the indentation would remain constant as illustrated by the horizontal dotted line. C) SLM element consisting of a spring in series with a Voigt element with long-term stiffness k_l, additional stiffness k_a, and viscosity η. D) Bright field image of brain region mapped. White dashed line shows outline of brain. The approximate pathway of axons is indicated with a blue line. The first map shows the storage modulus (G') and the second map shows the loss modulus (G''). The rostral region of the optic tract (stiffer) is denoted as region 1 in the white dotted oval and the caudal region (softer) of the optic tract is denoted as region 1 in the white dotted oval. Scale bar 100 µm. e) Storage modulus of Xenopus brain tissue between soft (caudual of the optic tract, N= 399) and stiff (rostral of the optic tract, N=417) regions of the brain at 0.1 Hz. f) Loss modulus of Xenopus brain tissue between soft (N=398)

and stiff (N=390) regions of the brain at 0.1 Hz. g) $\tan\delta$ of Xenopus brain tissue between soft (N=397) and stiff (N=390) regions of the brain at 0.1 Hz. 12 biological replicates were used for e-g. Mann-Whitney U-test $Ns: p \leq 1$, $*: 1 \times 10^{-2} < p \leq 5 \times 10^{-2}$, $**: 1 \times 10^{-3} < p \leq 1 \times 10^{-2}$, $***: 1 \times 10^{-4} < p \leq 1 \times 10^{-3}$, $****: p \leq 1 \times 10^{-4}$. *The box shows the quartiles (calculated by the interquartile range (IQR)) and the whiskers show the rest of the distribution (1.5 IQR) except for points that are determined to be outliers. Outliers are considered as* $Q \pm$ *1.5 IQR.*

3.6. Discussion

3.6.1. Measuring viscoelasticity using AFM

There are several ways of measuring viscoelasticity at the nano and microscale including AFM, optical/magnetic tweezers, and others (Sugimura et al., 2016). AFM has the main advantage of mapping tissue mechanics at cellular resolution. Furthermore, there are a number of different ways to determine the viscoelastic properties of materials using AFM including force-displacement measurements (Viljoen et al., 2021), force-relaxation experiments (Chim et al., 2018), creep experiments (Hecht et al., 2015, Schierbaum et al., 2019, Rheinlaender and Schäffer, 2019), and oscillatory experiments (Alcaraz et al., 2003). The best case would be to use oscillatory AFM whereby at each measurement position the AFM tip is oscillated over a range of frequencies. During such measurements, a stiff cantilever is required, and the instrument must be able to oscillate the cantilever at a large range of frequencies and at each pixel it can take several minutes per measurement. It was showed by Thompson et al. (2019) that local tissue mechanics changed within a few tens of minutes making. Therefore, it may not be possible to capture the local tissue elasticity / viscoelasticity using an oscillatory technique. For that reason, only methods whereby the viscoelasticity can be obtained in the seconds timescale are amendable in this project.

There are a number of ways of obtaining viscoelastic information across shorter timescales such at extracting the viscoelastic elasticity from the force displacement curves which has been reported by Efremov et al. (2017), Garcia and Garcia (2018a), and Garcia et al. (2020) by fitting the extension and retraction parts of the force-displacement curves to different viscoelastic models. However, such methods are sensitive to adhesion between the sample and tip unless they are corrected for which requires more analysis (Efremov et al., 2020). For that reason, it was only possible to extract the viscoelastic properties of developing tissues with creep or stress relaxation experiments. Chim et al. (2018) reported a method for measuring the viscoelastic properties of biological materials using ‘step-displacement’ which

is unrealistic because it takes time (Δt_A) for the AFM to reach the step-point and therefore a deconvolution of the force history should be computed ($\int_0^t J(t-t')\frac{dF(t\prime)}{dt\prime}dt'$, Eq. 20). The authors validate their technique using PDMS which is rheologically "well-behaved" compared to cells which further supports the case to take into account the force-history.

It has been shown that the force history can be considered by analytically solving Eq. 20 by modelling the force-ramp using a polynomial during a creep experiment (Hecht et al., 2015, Schierbaum et al., 2019, Rheinlaender and Schäffer, 2019). Here, I applied the same analysis but extended the models to include the Maxwell, Voigt, and SLM models. Although, it has been reported that cells can be modelled using a PLR model as a soft glassy material, I found that a SLM better fitted indentation time curves compared to a PLR model for *Xenopus* tissue, rodent tissue, and PAA gels. It would also be possible to fit a generalized SLM model, consisting of N SLM models in series and taking $\lim_{N\to\infty}$ of a generalized model which leads to a better fitting accuracy but is more computationally expensive (Calhoun et al., 2019).

Furthermore, it has been shown that fractional viscoelastic or non-linear viscoelastic models can be used, but again this leads to much more complexity and requires highly specialized fractional calculus (Bonfanti et al., 2020, Koser et al., 2015, Weber et al., 2017). It is also not possible to use fractional or PLR models in the motor clutch model which is discussed in later chapters (5.2). For that reason, I decided that the SLM would be a good first approximation of the indentation-time data which is also supported with the low RMSE score. Although, it was possible to analytically solve Eq. 20 for different viscoelastic models while also including the force history there are some limitations to the method. When using a polynomial force ramp with degree of $1 \leq \alpha \leq 2$, where α is the degree, does not account for when the AFM overshoots the force setpoint. In future work, it would be interesting to model the force ramp using more complex functions, but this will inevitability make it harder to analytically solve Eq. 20. At each pixel the cantilever is held into the sample which could have caused damage to the tissue, or a non-linear cell response could occur giving rise to artifacts. In summary, the SLM was a good first approximation to obtain the viscoelasticity of a variety of substrates including biological tissues.

3.6.2. Viscoelasticity of the developing *Xenopus* brain

Wang and Wineman (1972) demonstrated in the early 1970s that brain tissue exhibits viscoelasticity at the bulk scale for intact brain tissue. Many more recent studies have used magnetic resonance elastography (MRE) to characterise the viscoelasticity of brain tissue (Bigot et al., 2018) and even how viscoelasticity changes during visual tasks (Lan et al., 2020).

The viscoelasticity of brain tissue can be used to help physicians to diagnose disease (Murphy et al., 2019) and others have shown that tissue mechanics changes during disease (Segel et al., 2019). However, techniques such as MRE capture the viscoelastic at larger length scales compared to AFM which can capture cellular and sub-cellular resolution (Alekya et al., 2019), and time scales way beyond that of cellular mechanosensing. AFM provides a good experimental technique to measure the spatial elasticity of the developing *Xenopus* tissue which has been shown to be heterogenous (Koser et al., 2016, Thompson et al., 2019). For that reason, I extended the AFM technique using the methodology developed in this chapter (refer to section 3.4) to map the spatial viscoelasticity of the intact developing *Xenopus* brain.

I found that that the loss modulus increases with an increase in the storage modulus, which means that tissue that has a higher stiffness also has a higher viscosity. Hecht et al. (2015) reported that cells with a higher elastic stiffness had a higher viscosity (note in the paper they report a lower fluidity which is inversely proportional to viscosity). At the tissue level, Canovic et al. (2016) reported that pig brain tissue has a storage modulus in the range of hundreds of Pa while the loss modulus was in the range of tens of Pa using bulk rheology. The range of viscoelastic properties is consistent with the values reported here for *Xenopus* brain tissue. Lu et al. (2006) reported that mammalian hippocampus at the tissue and cellular scale had a storage and loss modulus in a similar range to that reported here. Furthermore, I found that the storage modulus was always higher than the loss modulus, suggesting that brain tissue is predominantly elastic, in agreement with previous literature (Lu et al., 2006).

Notably, it is unreasonable to assume that the values of the storage and loss modulus can directly be compared to literature since there are many experimental parameters that can impact the measurements. For example, Canovic et al. (2016) measure the creep compliance function using AFM but they do not take into consideration the force history and assume that the force ramp is instantaneous. It has also been shown that the viscoelastic properties of the CNS vary at the tissue and cellular level (Lu et al., 2006) and it would be expected that different regions of the CNS have different properties. Furthermore, many non-linear effects can occur in tissue due to the ECM fibrous like network and cells (van Oosten et al., 2019). Therefore, differences in experimental measurements and CNS tissue architecture make it difficult to directly compare results.

Along with characterising the storage and loss modulus I also calculated the loss tangent, which describes the relative contributions of elasticity and viscosity. I found that elastically stiffer regions of the brain had a lower loss tangent Figure 11g, suggesting that stiffer

tissue has a small viscous contribution. Antonovaite et al. (2021) found that regions of the mouse brain that were elastically stiffer also had a lower loss tangent in agreement with the results presented here. It is noteworthy to mention that Antonovaite et al. (2021) did report higher absolute values of the loss tangent compared to the values here and those cited by Charrier et al. (2018), which were in the range of 0.1 to 0.2. Again, the differences in absolute values could be due to difference in measurement techniques or post-mortem artefact.

Previously, it has been demonstrated that local tissue elasticity of the developing *Xenopus* brain is correlated with axon path finding during optic tract development. In this chapter, I found that the developing *Xenopus* brain exhibits heterogeneous viscoelasticity. It could be that local tissue viscoelasticity is important for axon path finding. However, to understand how viscoelasticity contributes to axon path finding I would need to perturb tissue elasticity and viscosity independently. It is challenging to perturb viscosity and elasticity independently because the properties are intrinsically linked (i.e. chemically crosslinking to increase tissue stiffness would reduce tissue flow). Albeit, my work does provide a methodology for further investigating the role of viscoelasticity during development and axon path finding.

3.6.3. Limitations of AFM procedure

When measuring the viscoelastic behaviour of materials, the loading rate is an important experimental parameter that can influence the creep response (or stress relaxation). The loading rate is the same as the force history ($\frac{dF}{dt}$) defined in Eq. 20. During my experiments, I only used a single loading rate to fit the viscoelastic models as the loading rate is captured in the analytical solutions presented for the Maxwell, Voigt, and SLM models by the force history. More explicitly, the loading rate is captured by fitting the force ramp part of the indentation time curve to the piecewise polynomial function defined in Eq. 21. Theoretically, this means that the viscoelastic model parameters should be consistent independent of the loading rate given that Eq. 21 is a good approximation of the force history. However, I did not experimentally test this assumption in my thesis. In future work, the assumptions around the loading rate could be tested by measuring the viscoelastic properties of a reference material at different loading rates. Such experiment would not only confirm if the models were appropriate to capture different loading rates but also the robustness of the parameters obtained using the analytical solution.

Furthermore, when analysing the viscoelastic properties of brain tissue (Figure 11), I presented the storage and loss modulus at a fixed frequency of 0.1 Hz by applying a Fourier transform to the SLM. Generally, both the storage and loss modulus are dependent on the

frequency and therefore the viscoelastic maps may have different characteristics at different frequencies. In future work, the viscoelastic brain maps could be compared at different frequencies to determine if frequency is important for brain tissue rheology. I had selected a frequency of 0.1 Hz based on the work of Charrier et al. (2018) who suggested that cells probe their substrate in the range of 0.1 to 1 Hz. In future work it would be good to more rigorously define a biologically relevant frequency range that is correct in the context of axon growth and guidance. Such frequency range could be calculated by analysing the loading rates obtained from the motor clutch simulations which are presented later in this work (see Chapter 5).

As previously mentioned, the robustness of the parameters obtained at different frequencies could further be validated by using a reference material. When first developing the AFM protocols shown in this thesis, I tried to use silly putty (that has well characterized properties) to validate the robustness of the parameters. However, I was unable to collect processable indentation time data due to very large force overshoots during the force ramp part of the measurement. This meant that it was not possible to fit the force ramp function (Eq. 21) to the data that considered the loading history to solve Eq. 47 analytically. In future work, it would be good to develop a reference material that models the rheological properties of soft biological tissues.

3.7. Summary

In this chapter, I have presented analytical solutions for to the Volterra integral that connect the force and indentation relationship for the Maxwell, Voigt, and SLM models of viscoelasticity. I measured the goodness of fit for each of the models and found that the SLM was the best approximation of the creep behaviour for *Xenopus* tissue, rodent tissue, and PAA gels. Using the developed analysis, I mapped the viscoelasticity of the intact and developing *Xenopus* brain and found that tissue viscosity increases with increasing tissue stiffness. The *Xenopus* brain tissues exhibited heterogeneous viscoelasticity and regions with a higher tissue stiffness had a smaller viscous contribution.

3.8. Acknowledgements

A.J. Thompson (Franze lab, PDN, Cambridge) and E. K. Pillai (Franze lab, PDN, Cambridge) assisted with *Xenopus* brain exposure. J. Becker (Franze lab, PDN, Cambridge) performed AFM creep experiments on rodent CNS tissue. I'd like to thank J. Rheinlaender (Tübingen University, Tübingen, Germany) for discussions about AFM analysis.

Chapter 4: Viscoelasticity *in vitro*

4.1. Background

In chapter 3, I measured viscoelasticity of biological tissues and hydrogels using AFM. I found that both elasticity and viscosity are spatially heterogeneous within the developing *Xenopus* brain. Therefore, during the development of the optic tract, axons are not only exposed to elasticity gradients but also viscosity gradients. Previous work in the group has investigated the effects of elasticity on the growth of RGC axons yet no experiments have investigated the effects of the viscous component. To investigate the effects of viscosity on axon growth I developed substrates with tuneable viscosities and cultured *Xenopus* eye primordia explants to measure the influence of viscosity.

4.2. Elastic and viscoelastic substrates

Charrier et al. (2018) previously demonstrated that addition of linear polyacrylamide (LPA) to PAA hydrogels can yield hydrogels with tuneable elasticity and viscosity. Here, I modified the formulations to produce gels with an increasing storage modulus and ~1-10 % loss modulus using PAA and poly(hydroxy-acrylamide) (PHA). Furthermore, in the original protocol from Charrier et al. (2018) they used acrylic acid N-hydroxysuccinimide (AA-NHS) to chemically functionalize PAA and LPA. After trying the NHS chemical modification, I found that the *Xenopus* eye primordia explants had poor adhesion to the substrates, and it was not possible to increase the degree of functionalization due to the poor solubility of AA-NHS in water.

For that reason, I synthesised linear poly(hydroxy-acrylamide) by adding hydroxyl-acrylamide into the acrylamide reaction mixture to introduce hydroxy groups onto the polymer backbone which also led to suboptimal explant adhesion. To improve adhesion to substrates, I reacted linear polyacrylamide with acrylamide and bis-acrylamide to make viscoelastic gels and then I functionalized the surface with hydrazine hydrate to introduce amine groups onto the surface which led to good explant adhesion.

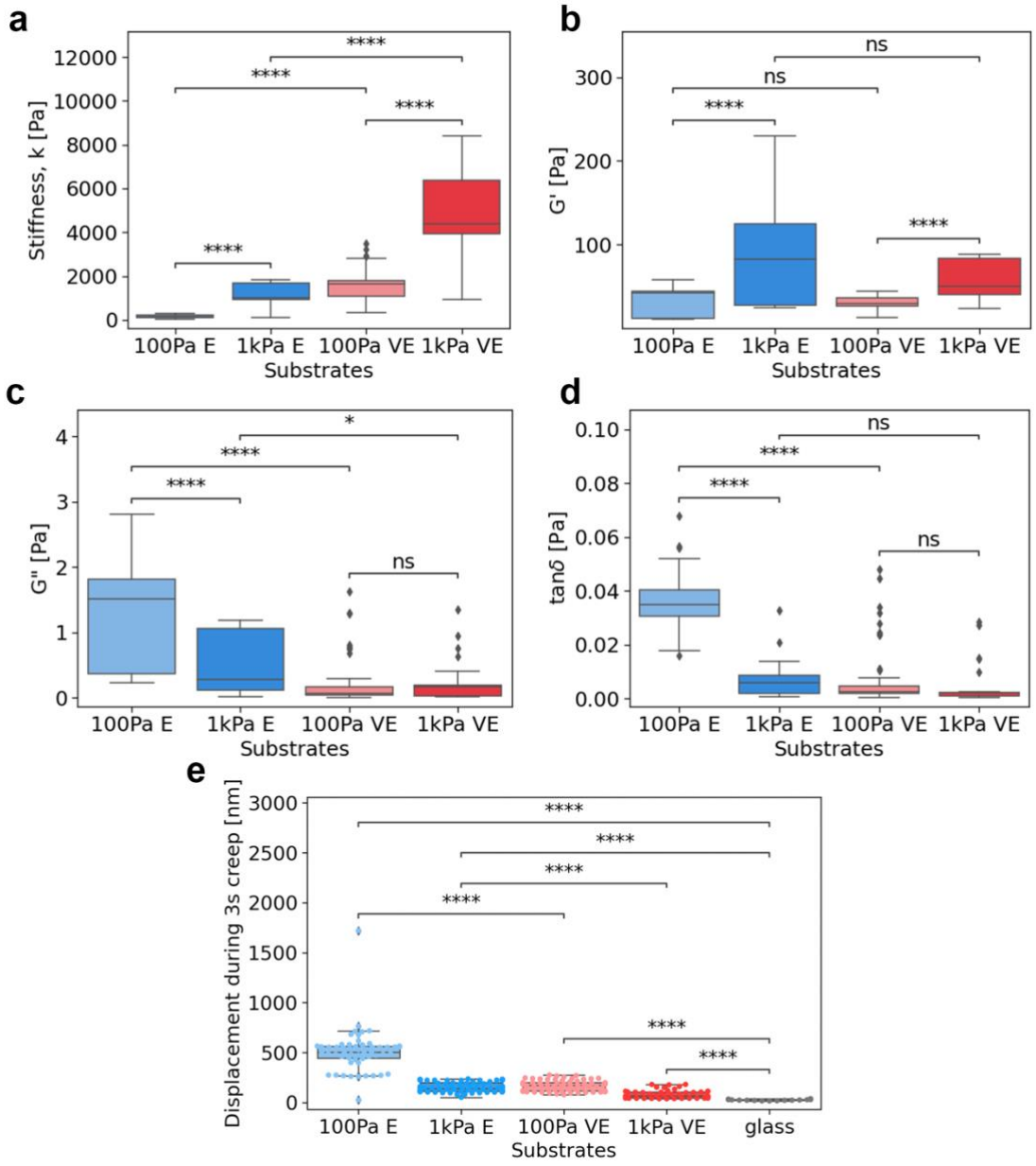

Figure 12 Polyacrylamide substrates can exhibit elastic and viscoelastic and elastic mechanics.

Mechanical properties of elastic (blue) and viscoelastic (red) gels. Each plots represents a different mechanical parameter. a) Hertz stiffness, b) shear storage modulus, c) shear loss modulus, and d) loss tangent. e) shows the displacement of the substrate during a 3s creep measurement with a force application of 10 nN for each substrate compared to a class control. Mann-Whitney U-test with Bonferroni correction. $Ns: p \leq 1, *: 1 \times 10^{-2} < p \leq 5 \times 10^{-2}, **: 1 \times 10^{-3} < p \leq 1 \times 10^{-2}, ***: 1 \times 10^{-4} < p \leq 1 \times 10^{-3}, ****: p \leq 1 \times 10^{-4}$. *E = elastic and VE = viscoelastic. 100Pa E N=45 gels, 100Pa VE N=62 gels, 1kPa E N=59 gels, 1kPa VE N= 24 gels, glass N=15. The box shows the quartiles (calculated by the interquartile*

range (IQR)) and the whiskers show the rest of the distribution (1.5 IQR) except for points that are determined to be outliers. Outliers are considered as $Q \pm 1.5$ IQR.

In the previous section, I found that the Hertz model best fitted the data when modelled as an elastic substrate and the SLM fitted the indentation-time data the best for a viscoelastic model (section 3.4). For that reason, I measured the different mechanical constants for the elastic and viscoelastic substrates for the Hertz and SLM models. I will refer to soft as 100 Pa and stiff as 1 kPa for the elastic and viscoelastic substrates. Soft elastic substrates were significantly softer ($k = 163.73 \pm 73.15$ Pa) compared to stiff elastic substrates ($k = 1174.44 \pm 451.71$ Pa) as shown in Figure 12a when fitted to the Hertz model. Soft viscoelastic gels also had a lower Hertz model stiffness ($k = 1573.75 \pm 792.07$ Pa) compared to stiff viscoelastic gels ($k = 4629.91 \pm 2281.91$ Pa) (Figure 12a). According to the Hertz model, viscoelastic gels were significantly stiffer compared to their elastic equivalents.

To get comparable values to the AFM maps reported in section 3.5, indentation-time curves were also fitted to the SLM and transformed to obtain the storage (G') and loss (G'') moduli (Figure 12b-c). The soft elastic substrates had a significantly lower storage modulus ($G' = 31.04 \pm 16.33$ Pa) compared to the stiff elastic substrates ($G' = 82.18 \pm 46.25$ Pa). The soft viscoelastic substrates also had a significantly lower storage modulus ($G' = 29.03 \pm 8.56$ Pa) compared to the stiff viscoelastic substrates ($G' = 56.69 \pm 23.23$ Pa). There was no significant difference between the storage or loss modulus for the soft elastic and viscoelastic substrates and the stiff elastic and viscoelastic substrates (Figure 12b).

The soft elastic substrates had a significantly larger loss modulus ($G'' = 1.19 \pm 0.79$ Pa) compared to the stiff elastic substrates ($G'' = 0.53 \pm 0.46$ Pa) as shown in (Figure 12c). There was no significant difference between the soft viscoelastic substrates ($G'' = 0.21 \pm 0.34$ Pa) and stiff viscoelastic substrates ($G'' = 0.25 \pm 0.33$ Pa). The loss tangent can be used to measure the proportions of the elastic and viscous component (Figure 12d). The closer the loss tangent is to one the more the substrate resembles a viscous liquid. The soft elastic substrates had a significantly larger loss tangent ($\tan\delta = 0.04 \pm 0.01$) compared to stiff elastic substrates ($\tan\delta = 0.01 \pm 0.01$), suggesting that the stiffer substrate more closely resembled an elastic solid. The soft viscoelastic substrates ($\tan\delta = 0.01 \pm 0.01$) were not significantly different compared to the stiff viscoelastic substrates ($\tan\delta = 0.01 \pm 0.01$).

For each substrate I measured the displacement of the surface after a 3 second creep experiment with a 10 nN force hold to confirm creeping of the substrates compared to a glass control. Since glass is a rigid elastic solid there should be close zero displacement at forces of

10 nN with a soft cantilever (median 24.61 nm for glass Figure 12e). Soft elastic substrates were displaced 505.46 nm during the creep experiment while stiff elastic substrates displaced 141.88 nm (Figure 12e). Soft viscoelastic substrates creeped 173.13 nm and stiff viscoelastic substrates creeped 64.91 nm (Figure 12e).

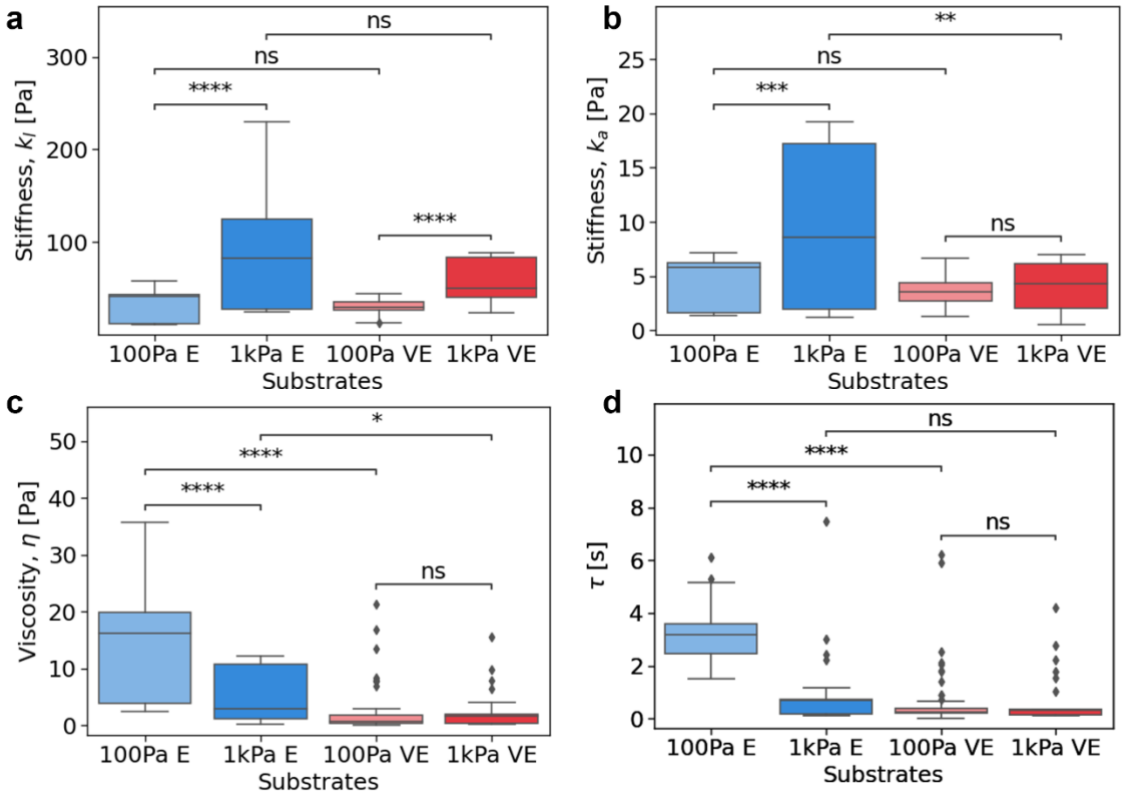

Figure 13 Mechanical constants from the SLM of elastic (blue) and viscoelastic (red) gels.

a) long-term stiffness, b) additional stiffness, c) viscosity, and d) characteristic timescale. Mann-Whitney U-test with Bonferroni correction. Ns: $p \leq 1$, *: $1 \times 10^{-2} < p \leq 5 \times 10^{-2}$, **: $1 \times 10^{-3} < p \leq 1 \times 10^{-2}$, ***: $1 \times 10^{-4} < p \leq 1 \times 10^{-3}$, ****: $p \leq 1 \times 10^{-4}$. *E = elastic and VE = viscoelastic. 100Pa E N=45 gels, 100Pa VE N=62 gels, 1kPa E N=59 gels, 1kPa VE, N= 24 gels. The box shows the quartiles (calculated by the interquartile range (IQR)) and the whiskers show the rest of the distribution (1.5 IQR) except for points that are determined to be outliers. Outliers are considered as* $Q \pm 1.5$ *IQR.*

To understand the mechanical response of the elastic and viscoelastic substrates more comprehensively I also compared the different mechanical constants that were obtained from fitting the indentation-time curves with the SLM (Figure 13). The SLM has three parameters k_l, k_a, and η which I described in detail in section (3.4). The soft elastic substrates had a significantly lower long-term stiffness ($k_l = 30.66 \pm 16.08$ Pa) compared to the stiff substrates

($k_l = 82.13 \pm 46.24$ Pa) (Figure 13b). The soft viscoelastic substrates also had a significantly lower long-term stiffness ($k_l = 28.98 \pm 8.53$ Pa) compared to the stiff viscoelastic substrates ($k_l = 56.65 \pm 23.25$ Pa). There was no difference between the long-term stiffness for the soft elastic and viscoelastic substrates and stiff elastic and viscoelastic substrates (Figure 13b). The soft elastic substrates had a significantly lower ($k_a = 4.34 \pm 2.29$ Pa) additional stiffness compared to the stiff elastic substrates ($k_a = 10.05 \pm 6.88$ Pa) (Figure 13a). There was no significant difference in the additional stiffness between soft viscoelastic substrates ($k_a = 3.55 \pm 1.33$ Pa) and stiff viscoelastic substrates ($k_a = 4.19 \pm 2.18$ Pa) (Figure 13a).

The soft elastic substrates had a significantly higher viscosity ($\eta = 13.18 \pm 9.22$ Pa) compared to the stiff elastic substrates ($\eta = 5.42 \pm 4.73$ Pa) (Figure 13c). While there were no significant differences in the viscosity between the soft ($\eta = 2.25 \pm 4.03$ Pa) and stiff ($\eta = 2.58 \pm 3.68$ Pa) viscoelastic substrates (Figure 13c). The viscoelastic parameters can also be used to calculate a characteristic timescale ($\frac{1}{\tau} = \frac{k_l k_a}{\eta(k_l + k_a)}$) which can be used to physically describe how quickly stresses or strains relax within the substrate. The characteristic timescale of soft elastic substrates was significantly higher ($\tau = 3.13 \pm 0.97$ s) compared to the stiff elastic substrates ($\tau = 0.73 \pm 1.04$ s) as shown in (Figure 13d). There were no significant differences between the characteristic timescale for soft ($\tau = 0.62 \pm 1.14$ s) and stiff ($\tau = 0.71 \pm 1.03$ s) viscoelastic substrates (Figure 13d). Substrates with a higher characteristic timescale respond slower to an applied force and exhibit more fluid like behaviour.

Table 6 Viscoelastic properties of elastic and viscoelastic gels measured using oscillatory shear rheometry. N=3 gels.

Target	Storage modulus (G') [Pa]	Loss modulus (G'') [Pa]	Loss tangent ($\tan\delta$)
100 Pa E	60.71 ± 0.75	0.38 ± 0.07	0.006
1 kPa E	524.62 ± 2.9	3.47 ± 11.84	0.007
100 Pa VE	335.85 ± 221.2	24.29 ± 4.11	0.072
1 kPa VE	2401 ± 705.69	180.15 ± 46.6	0.075

Along with the AFM measurements, I also assessed the rheological properties of the gels using an oscillatory shear rheometer during polymerization (Table 6). In a shear configuration, the soft and stiff elastic substrates had higher storage modulus (soft: $G' = 60.71 \pm 0.75$ Pa and stiff: $G' = 524.62 \pm 2.9$ Pa) compared to the AFM measurements (soft: $G' = 31.04 \pm 16.33$ Pa and stiff: $G' = 82.18 \pm 46.25$ Pa). The soft elastic substrate had a lower

loss modulus ($G'' = 0.38 \pm 0.07$ Pa) compared to that obtained with the AFM ($G'' = 1.19 \pm 0.79$ Pa). The stiff elastic substrates had a higher loss modulus ($G'' = 3.47 \pm 11.84$ Pa) compared to the AFM measurements ($G'' = 0.53 \pm 0.46$ Pa). The storage modulus of the soft and stiff viscoelastic substrates were considerably higher when measured with a shear rheometer (soft: $G' = 335.85 \pm 221.2$ Pa and stiff: $G' = 2401 \pm 705.69$ Pa) compared to the AFM measurements (soft: $G' = 28.66 \pm 8.96$ Pa and stiff: $G' = 56.69 \pm 23.23$ Pa). Furthermore, the soft and stiff viscoelastic substrates exhibited a greater loss modulus (soft: $G'' = 24.29 \pm 4.11$ Pa and stiff: $G'' = 180.15 \pm 46.6$ Pa) compared to AFM measurements (soft: $G'' = 0.20 \pm 0.34$ Pa and stiff: $G'' = 0.25 \pm 0.33$ Pa).

4.3. *In vitro* eye primordia explants

To investigate the influence of elasticity and viscosity on the substrates described in the previous section (4.2) I cultured *Xenopus* eye primordia explants on mechanically distinct substrates. Eye primordia from the developing *Xenopus* were explanted at stages 34-36 NT onto different substrates (i.e. elastic and viscoelastic) (Figure 14a). The retina of the eye primordia were explanted facing upwards so axons were able to grow radially across the 2D substrate for 24 hours.

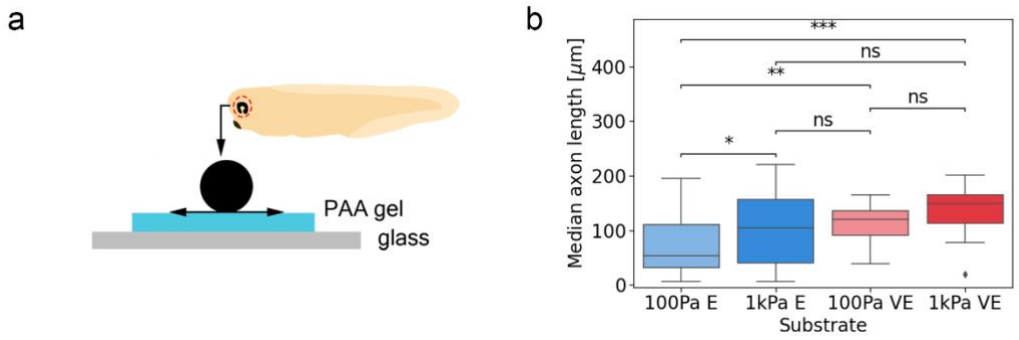

Figure 14 RGC median axon length changes on elastic (blue) but not on viscoelastic (red) substrates *in vitro.*

a) Schematic of Xenopus eye primordia culture system. Eye primordia are removed at stage 34-36 NT and plated onto purely elastic or viscoelastic PAA substrates. b) Median axon length of axons on elastic (blue) and viscoelastic (red) gels for soft and stiff substrates. Axons were significantly longer on stiff elastic substrates compared to soft elastic. There were no significant differences between the viscoelastic substrates. Oneway ANOVA = 0.0001 followed by a Post hoc Bonferroni. $Ns: p \leq 1$ $*: 1 \times 10^{-2} < p \leq 5 \times 10^{-2}$, $**: 1 \times 10^{-3} < p \leq 1 \times 10^{-2}$, $***: 1 \times 10^{-4} < p \leq 1 \times 10^{-3}$. *100Pa E N=68 eyes, 1kPa E N=54 eyes, 100Pa VE N=16 eyes, 1kPa VE N=11 eyes for at least three biological replicates. The box shows the quartiles (calculated by the interquartile range (IQR)) and the whiskers show the rest of the distribution (1.5 IQR) except for points that are determined to be outliers. Outliers are considered as* $Q \pm 1.5$ *IQR.*

I first cultured explants on soft and stiff elastic substrates and found that axons were significantly longer (Post hoc Bonferroni, $p = 0.011$) on stiff elastic substrates (101.32 ± 67.53 µm) compared to soft elastic substrates (68.90 ± 45.28 µm) (Figure 14b), confirming our previous data (Koser et al., 2016). I also cultured explants on soft and stiff viscoelastic substrates. There were no differences in median axon lengths on soft viscoelastic substrates (113 ± 35.69 µm) compared to stiff viscoelastic substrates (132.63 ± 50.63 µm). While median axon lengths were significantly longer on soft (Post hoc Bonferroni, $p = 0.002$) and stiff (Post hoc Bonferroni, $p = 0.0003$) viscoelastic substrates compared to soft elastic substrates. Median axon lengths were not significantly different between stiff elastic, soft viscoelastic, and stiff viscoelastic substrates (Figure 14b).

4.4. Discussion

4.4.1. Mechanics of compliant substrates

As shown in Chapter 3, the developing *Xenopus* brain exhibits viscoelasticity and I wanted to understand how viscoelasticity may be regulating axon growth. To test if viscosity influenced axon growth, I cultured *Xenopus* eye primordia explants on substrates with tuneable viscoelasticity. I followed a procedure reported by Charrier et al. (2018) to fabricate viscoelastic gels. However, in the original paper the shear modulus of the substrates were in the range of 5 kPa and the loss moduli were increased from 10 Pa, 260 Pa, and 490 Pa to give tuneable viscoelasticity (Charrier et al., 2018). AFM measurements in the previous section demonstrated that *in vivo* brain viscoelasticity was much lower compared to the mechanics of the gels reported by Charrier et al. (2018). For that reason, I modified the formulations to obtain hydrogels with mechanical properties close to *in vivo* values.

There was a large disparity between the mechanical properties measured at the macroscopic (shear rheology) and microscopic (AFM) length scales which could have been due to several reasons including variations in bulk and microscale mechanics, sample preparation, and/or differences in measurement technique. Shear rheology and AFM probe the mechanical properties of substrates at the bulk and local scales and have different loading geometries. In shear rheology, the substrate is loaded between a cone and plate and the cone is oscillated at a set frequency and the shear displacement is measured. In shear rheology, the contact area between the instrument and substrate is usually tens of millimetres, whereas, in AFM the contact area is in the range of nanometres or micrometres. Therefore, the mechanical properties are probed at very different length scales. When forces are applied at the millimetre scale, they will be transmitted over many polymer chains crosslinked together. In this case, the average density of crosslinks within the material will determine the mechanics measured.

AFM probes the mechanical properties at a local scale (nano/micro-meters) compared to shear rheology (millimetres) which means the local crosslinking density will be important. Di Lorenzo et al. (2015) demonstrated that the elastic stiffness of homogeneous or heterogenous polymer gels are different at the 100 nm, 2 μm, and > 1mm length scales. It was suggested that the differences in mechanics could have been due to nonaffine deformation which can occur in PAA gels (Basu et al., 2011). Di Lorenzo et al. (2015) found that elasticities were lower for heterogenous polymer gels when measured with shear rheology (E = 5.7 kPa) compared to AFM at 100 nm (E = 11.8 kPa) and 2 μm (E = 9.6 kPa). Whereas I found that

substrates had a much lower shear modulus when using AFM compared to shear rheology. Therefore, it is unlikely that gel heterogeneity is responsible for the differences in mechanics.

Another possible explanation for the differences in mechanics could have been due to loading geometry and poroelastic effects. Poroelasticity is the interaction between fluid flow and solids within a porous substrate. The PAA substrates used in this work consist of a solid phase (polyacrylamide) and liquid phase (water). The deformation of poroelastic materials is limited by the rate at which fluid can redistribute. For example, a dry sponge can deform faster compared to a wet sponge because there is no fluid redistribution. It has been shown that polyacrylamide gels exhibit poroelasticity (Esteki et al., 2020). I found that soft elastic gels exhibited very large amounts of displacement during a 3 second force hold step compared to all other substrates. If poroelastic effects were responsible for these differences, it would be plausible since the soft elastic substrates have the lowest polymer content and theoretically the lowest crosslinking density. A lower crosslinking density would result in larger porosity facilitating fluid flow and redistribution. The viscoelastic gels have a higher polymer content due to the addition of the linear polyacrylamide which could lead to a smaller mesh size, and therefore less poroelasticity. Therefore, it's not surprising that soft viscoelastic substrates exhibit different displacements during a 3s creep hold compared to the soft elastic substrates.

Finally, the difference in mechanics could also have been due to differences in sample preparation. For AFM measurements it was possible to make the gels on glass coverslips in petri dishes in accordance with explant experiments. For shear rheology measurements, gels were polymerized *in situ* and the mechanics were measured overtime (30 mins) once the storage and loss moduli had plateaued the final values were recorded. Substrates measured by AFM were incubated in PBS during and after polymerization before they were measured by AFM. The mechanics of substrates were measured by AFM several hours after polymerization. Therefore, substrates prepared for AFM will have had time to undergo swelling which can alter the mechanical properties. Subramani et al. (2020) investigated the effects of swelling on PAA gels using shear rheology and AFM over time. Immediately, after polymerization the mechanical properties of PAA substrates matched when measured by AFM and bulk rheology. However, substrates with an initial stiffness of E = ~600 Pa (measured by AFM and shear rheology) softened to E = ~300 Pa after 3 hours of incubation in PBS. The authors found that stiffer substrates (> 10 kPa) did not undergo the same changes in mechanics when measured by AFM. Subramani et al. (2020) illustrate that the mechanics of PAA substrates can change

due to swelling in a few hours. Therefore, swelling could have been one of the reasons for differences in mechanical properties between AFM and shear rheology.

In summary, the disparity between mechanical properties measured using shear rheology and AFM could have been due to several reasons including loading geometry, poroelasticity, and swelling. It would take a much more detailed rheological investigation to figure out the main reason for the differences between measurements. In future work, the swelling behaviour of both elastic and viscoelastic gels could be measured overtime to determine the effects of swelling on viscoelasticity. The methods from Esteki et al. (2020) could be used to measure the poroelasticity of each substrate to quantify if there is a poroelastic contribution when measured using AFM.

4.4.2. Viscoelasticity regulates axon growth

Koser et al. (2016) demonstrated that the elasticity of PAA substrates regulated the median distance travelled by axons on soft (100 Pa) and stiff (1 kPa) substrates. Axons on 100 Pa substrates had a median length of ~100 μm, whereas axons on 1 kPa substrates had a median length of ~160 μm (Koser et al., 2016). The median length of axons reported here on 100 Pa and 1 kPa substrate were shorter than those reported by (Koser et al., 2016) which could be due to variations in the analysis procedure, which is qualitative when thresholding the image for Sholl analysis.

When I cultured *Xenopus* eye primordia on soft and stiff viscoelastic substrates, there were no significant differences between the median axon lengths on soft and stiff substrates. There was a 2 kPa difference in stiffness between the soft and stiff viscoelastic substrates (shear rheology: soft: $G' = 335.85 \pm 221$ Pa vs stiff: $G' = 2401 \pm 705.69$ Pa and AFM: soft $k = 1573.75 \pm 792.07$ Pa vs stiff: $k = 4629.91 \pm 2281.91$ Pa). While a difference in stiffness of ~ 500 – 1000 Pa on soft and stiff elastic substrates (shear rheology: soft: $G' = 60.71 \pm 0.75$ Pa vs stiff: $G' = 524.62 \pm 2.9$ Pa and AFM: soft $k = 163.73 \pm 73.15$ Pa vs stiff: $k = 1174.44 \pm 451.71$ Pa) lead to a significant difference in medium axon length. The median axon lengths were similar for stiff elastic, soft viscoelastic, and stiff viscoelastic suggesting that the there was something fundamentally different in the mechanics of the soft elastic substrates that may be regulating axon growth.

Both AFM (Figure 12a) and shear rheology (Table 6) confirmed that there were differences in the stiffnesses for the soft and stiff versions of the elastic and viscoelastic substrates. One property that is consistent with medium axon lengths is the loss tangent and characteristic substrate timescale measured by AFM (Figure 12d and Figure 13d). It is

noteworthy to mention that the loss tangent measured using shear rheology (Table 6) is different to that measured by AFM (Figure 12d). However, the differences in the loss tangent could be due to swelling, poroelasticity, and loading geometry of the measurements (as discussed in the previous section 4.4.1). Substrates that were mechanically characterized by AFM were incubated in PBS as were substrates used to measure median axon length. Furthermore, AFM measures mechanics at length scales in the nanometre and micrometre range which is similar to the length scales that axons mechanically interact with the substrate. The shear rheology measurements were conducted *in situ* during polymerization meaning that gels were not equilibrated in PBS before measurements. Substrates measured using shear rheology were also measured at much longer length scales compared to AFM. Therefore, it could be argued that the mechanics measured by AFM more realistically capture the mechanical conditions in the *in vitro* explant experiments compared to shear rheology. However, it could be argued that the analysis and mathematics used for shear rheology is more established and validated compared to that used for AFM.

There have been several publications suggesting that substrate timescales regulate mechanical interactions with cells (Adebowale et al., 2021, Gong et al., 2018, Chaudhuri et al., 2020) and not their stiffness alone. For that reason, I used the parameters from the SLM to calculate the characteristic timescale for each of the substrates and found that all the substrates except for the soft elastic gel had characteristic timescales below one second. The substrates with a timescale below one second also resulted in longer median axon lengths. The soft elastic substrate had a timescale in the order of 3 seconds and led to a shorter median axon length. Substrates with a characteristic timescale less than one also had a lower loss tangent suggesting that the substrates behaved more like an elastic solid compared to a viscous liquid. My results suggest that the loss tangent and characteristic substrate scale may be related to the median axon length. It would be interesting to measure the median axon length across a larger characteristic timescale range.

One of the limitations of the work that I have presented here is that it was not possible to test a large range of viscoelastic substrate properties. It was difficult to synthesize substrates with a fixed elasticity and varying viscosity that are relevant to the mechanics of brain tissue. In future work, it would be good to have a culture system whereby it is easier to control a broader range of viscoelastic properties. This can be achieve using systems such as hyaluronic acid (Hui et al., 2019), ionic gels (Nam et al., 2019), or supramolecular hydrogels (Whitaker et

al., 2021). Yet, these culture systems are not as inert as PAA meaning there might be interference of chemical signalling molecules.

In conclusion, I found that the medium axon length was shorter on soft elastic substrates compared to stiff elastic, soft viscoelastic, and stiff viscoelastic substrates. There were no differences between axon lengths on soft and stiff viscoelastic substrates suggesting that adding a viscous component changed the way in which axons grew. While axons grew significantly longer on stiff elastic substrates compared to soft elastic substrates. It was only on soft elastic gels that median axon lengths were significantly shorter, and the soft elastic substrate had a larger characteristic timescale (~ 3 s) compared to other substrates. Previous literature suggests characteristic substrate timescale can regulate cell responses. My provisional results suggest that this could also be the case for axons, but further work is required to demonstrate causality. The results suggest that it may be important to consider the role viscoelasticity in axon growth and not only elasticity.

4.4.3. Limitations and other interpretations

In this chapter there were large discrepancies between the rheological data obtained using AFM and rheometer measurements. In section 4.4.1, I discussed some possible explanations of why there were differences between the two measurements. However, these discrepancies also mean that the results can be interpreted in two different ways depending on which measurements are used. Substrates that were designed to be purely elastic had higher viscosities compared the viscoelastic substrates when compared using AFM. This would then suggest that viscosity suppresses axon growth according to Figure 14b. However, when using the shear rheology data (Table 6) there is a negligible viscous component for the purely elastic substrates. Therefore, it could be suggested that introducing a viscous component promotes axon growth according to Figure 14b. If we look at only the elastic parameters that are obtained using AFM and shear rheology, they both follow a similar trend. For example, based on the shear rheometer data the gels have the following shear modulus elastic 0.1 kPa: $G' \approx 60$ Pa, elastic 1 kPa: $G' \approx 524$ Pa, viscoelastic 0.1 kPa: $G' \approx 335$ Pa, and viscoelastic 1 kPa: $G' \approx 2401$ Pa. Therefore, it could also be concluded that the elastic stiffness is regulating the axon length and not the viscosity. However, in this thesis I have suggested that viscosity may play a role in axon regulation. In future work, to investigate the role of viscosity more rigorously, substrates with more tuneable viscosities and elasticities should be developed.

The discrepancies between the AFM and shear rheology raise the question of which method is best to classify the rheological behaviour of the gels. It could be argued that AFM measurements probe the substrate at cellular length scales and therefore better capture the mechanics that cells would "feel". However, AFM measurements are conducted in a compressive configuration meaning that the mechanics are measured when pushing into the substrate. When cells interact with substrates, they generally apply shear forces. Subsequently, it could then be argued that the measurements from the shear rheometer better represent the mechanical interaction albeit the length scales are different. Ideally it would be good if a shear measurement could be made at the correct length scale. In future work, both measurement techniques should be validated using a reference material (as discussed in 3.6.3) to confirm if either of the procedures are erroneous. If either of the methods disagree with the results presented in this thesis the conclusions would need to be revisited.

4.5. Summary

In this section, I fabricated elastic and viscoelastic substrates with tuneable mechanical properties. I also explored the viscoelastic response of the elastic and viscoelastic PAA substrates with AFM and shear rheology. The Hertz and SLM models were used to characterize the behaviour of the substrates. When *Xenopus* eye primordia were cultured on stiff elastic substrates, axons grew significantly longer compared to soft elastic substrates. However, on viscoelastic substrates there were no differences between axon lengths on substrates with higher and lower storage moduli. I found that the mechanical properties of the elastic and viscoelastic substrates varied on the bulk (measured by shear rheology) and local length scales (nanometres to micrometres). These differences could have been due to substrate swelling, poroelasticity, or different loading geometries. I found that axons grew longer when the underlying substrate had a shorter characteristic timescale, suggesting that not only elasticity is important for axon growth but also viscoelasticity. In future work, it would be good to produce viscoelastic gels with a larger range of substrate timescales and measure the influence on axon growth.

4.6. Acknowledgements

S. K. Foster (Franze lab, PDN, Cambridge) initially help me learn eye primordia cultures and provided guidance on Sholl analysis.

Chapter 5: Simulating retrograde flow and traction forces

5.1. Background

As shown in the previous chapters, the developing *Xenopus* brain exhibits heterogenous viscoelasticity (section 3.5) and modulating the mechanical properties of PAA substrates regulates axon growth (section 4.3). At the tip of the axon, the growth cone mechanically interacts with the external environment which can have varying mechanical properties. To better understand how elasticity and viscoelasticity regulate this mechanical interaction, I decided to run simulations based on mechanistic interactions between the growth cone and its substrate. To this end, I used the motor clutch model that was previously developed by Chan and Odde (2008) and Gong et al. (2018) in an elastic and viscoelastic framework.

Gong et al. (2018) reported a viscoelastic motor clutch model that predicted maximum cell spreading is achieved when the substrate timescale is approximately equal to the clutch binding rate. The clutch binding rate is the rate at which clutch molecules link actin filaments to integrins, whereby a force is transmitted. Here, I investigate how the motor-clutch model could be responsible for regulating the median axon length on substrates with varying mechanics. It has been shown that substrate viscoelasticity can regulate cell differentiation (Charrier et al., 2018), mesenchymal stem cell behaviour (Cameron et al., 2011), cell spreading (Chaudhuri et al., 2015), and hepatocyte morphology (Mandal et al., 2020). However, there has been no report on how viscoelasticity regulates the growth of axons. In this chapter, I used the motor clutch model to predict traction forces, actin retrograde flow rates, and axon growth velocity based on the mechanics of the elastic and viscoelastic substrates (section 4.2) and the developing *Xenopus* brain mechanics (section 3.5).

5.2. Elastic and viscoelastic responses according to the motor clutch model

To understand how the brain tissue and substrate mechanics regulate the interaction between the growth cone and substrate I explored how the motor clutch model predicts different responses based on the mechanical environment. In short, when a force is transmitted through a clutch molecule in an elastic case the substrate is instantaneously displaced according to Hooke's law (Figure 15a, elastic case leading to an instantaneous displacement from the red position to the blue position). For the viscoelastic case, when the clutch molecule engages there is an instantaneous elastic displacement like the elastic case that is followed by a time-

dependent displacement from the viscous component which is indicated by the red arrow in Figure 15b (viscoelastic case).

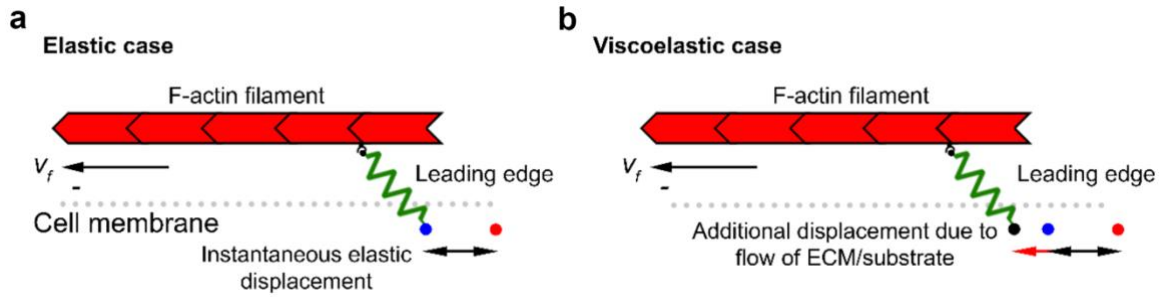

Figure 15 Viscoelastic substrates creep when under a constant force while elastic substrates instantaneously deform.

In both bases a) elastic and viscoelastic b) the actin filaments flow away from the leading edge (V_f). When a clutch engages between the substrate and actin filament the substrate is displaced. In the elastic case, the position of the substrate is moved from its initial position (red dot) to its final position (blue dot) which is proportional to the stiffness of the substrate. However, in the viscoelastic case the substrate is displaced from its initial position (red dot) to the blue dot instantaneously due to the elastic response. The substrate is then further displaced due to viscous flow of the substrate to its final position (black dot) over a given time interval. Schematic adapted from (Chaudhuri et al., 2015).

I modelled the mechanical interaction between a growth cone (Figure 16a) and a substrate for the two cases illustrated in Figure 15 using an elastic and viscoelastic substrate in the motor clutch model. A schematic of the viscoelastic motor clutch model is illustrated in Figure 16b. The main difference between the two cases is that in the elastic case the substrate mechanics are modelled as a single spring, whereas, in the viscoelastic case the substrate is modelled using SLM element (Figure 16b). In the viscoelastic case, there are three parameters used to describe the material response which are k_l, k_a, and η which I have describe in detail in previous sections (section 3.2 and 3.4).

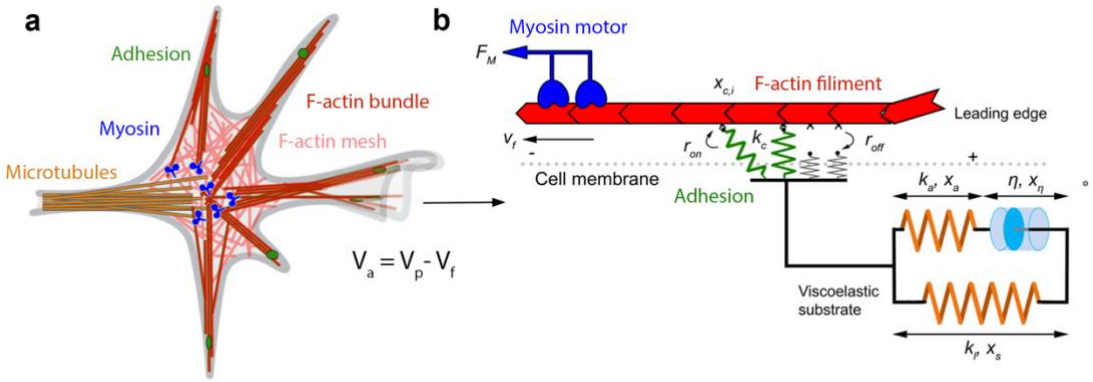

Figure 16 The advancing growth cone can be modelled using the motor clutch model.

a) Schematic of growth cone adapted from Franze (2020). Microtubules (orange) grow into the transition zone. Within the transition zone, myosin motors pull on F-actin filaments where they are depolymerized. At the tip of the growth cone, adhesion sites are formed between the external environment and the lamellipodium which leads to traction forces and reduced retrograde flow of F-actin filaments. b) Schematic of motor clutch model. n_m Myosin motors pull actin filaments with a force (F_M) towards the transition zone leading to a resting velocity of the actin filament (V_f). n_c Molecular clutches, with stiffness (k_c), stochastically link the actin filament to the viscoelastic substrate with an association and disassociation rate of r_{on} and r_{off}, respectively. Notably, this schematic is the same for the elastic case, however, a single spring with stiffness, k, is used to model the substrate response.

To understand the effect of viscosity on retrograde flow rates and traction forces, I performed a grid search using the viscoelastic motor clutch model for multiple long-term stiffnesses ($10^{-3} \leq k_l \leq 10^3$ kPa) and viscosities ($10^{-3} \leq \eta \leq 10^3$ kPa) with increasing additional stiffnesses ($k_a = 0.1, 0.5, 1$ kPa) (Figure 17a-b). Therefore, for each additional stiffness I simulate the retrograde flow and traction forces for every combination of long-term stiffness and viscosity which gives a traction force surface and retrograde flow surface which are shown in Figure 17a-b. To interpret the surface, if a random point is selected, the specific colour refers to the Z value (which is the retrograde flow rate or traction force). From the Z value, the corresponding Y value at that point specifies the viscosity (η) and the X value gives the long-term stiffness (Figure 17a-b).

Combinations of different SLM model parameters stochastically produced variations in the average simulated retrograde flow rates and traction forces as shown in Figure 17a-b. Since the simulated retrograde flow rates are related using the Hill relationship (Eq. 4), there is a

linear relationship between the two parameters. When a higher number of clutch molecules engage with the substrate higher traction forces are generated which reduces the retrograde flow of actin. Therefore, at higher retrograde flow rates there are lower traction forces and at lower retrograde flow rates there are higher traction forces.

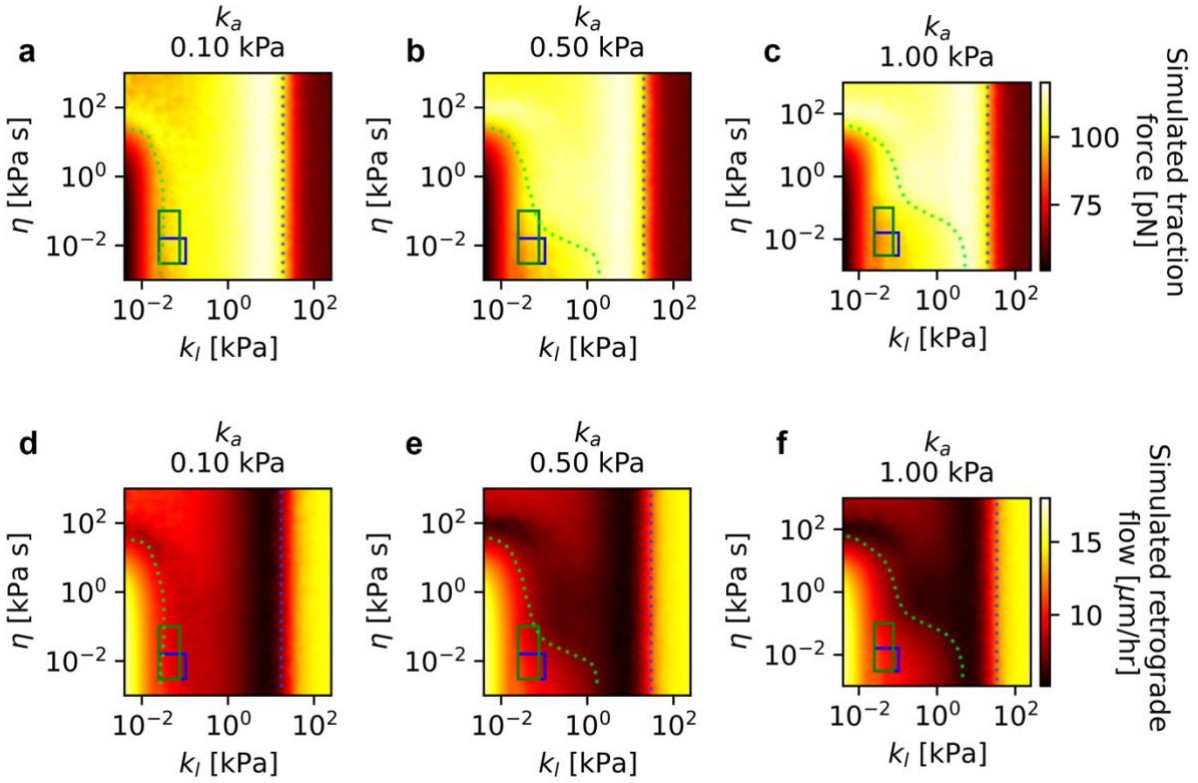

Figure 17 Viscosity regulates *in silico* retrograde flow and traction forces at physiologically relevant viscoelasticities.

Simulated traction forces with an addition stiffness (k_a) of a) 0.1 kPa, b) 0.5 kPa, and c) 1 kPa. Simulated retrograde flow rates with an addition stiffness (k_a) of d) 0.1 kPa, e) 0.5 kPa, and f) 1 kPa. as a function of viscosity (η) and long-term stiffness (k_l). Green dotted line (left hand side (LHS)) corresponds to a regime where simulated retrograde flow is increased with increasing long-term stiffness, while on (right hand side (RHS)) retrograde flow is reduced. Blue dotted line corresponds to regime where retrograde flow rates and traction forces become insensitive to viscosity. The green boxes correspond to the bounds of the parameters obtained from AFM experiments on gels. The blue boxes correspond to the bounds of the parameters obtained from AFM experiments of the developing Xenopus brain.

With increasing additional stiffness, simulated retrograde flow rates increase for low viscosities and long-term stiffnesses (Figure 17b green dotted boundary left hand side) while simulated traction forces are reduced (Figure 17a). On the right-hand side of the green dotted

boundary (Figure 17a) retrograde flow rates are reduced with increasing additional stiffness while simulated traction forces increase. At all additional stiffnesses, when the long-term stiffness exceeds a threshold (~10^2 kPa, Figure 17 black dotted line) simulated retrograde flow rates are maximised and become independent of viscosity. These results suggest that at higher effective stiffnesses ($k_a + k_l$), viscosity has no effect on retrograde flow rates and traction forces, while at lower effective stiffnesses viscosity becomes and important parameter.

I also overlayed the typical viscosity and long-term stiffness ranges for *Xenopus* (blue boxes, Figure 17) and PAA substrate (green boxes, Figure 17) mechanics on top of the simulated retrograde flow and traction force surfaces. Interestingly, at higher additional stiffness ($k_a = 0.5$ kPa) the viscosity begins to regulate the retrograde flow rates and traction forces as denoted by the green dotted boundary which grows with increasing additional stiffness (Figure 17a-f). In the current section, I investigated the effects of viscoelasticity across a large parameter space which might not be observed in physiologically relevant conditions. For that reason, I will take a closer look at the simulated responses with the mechanical constants obtained from AFM measurements outlined in section (3.5) and section (4.2).

5.3. Simulated cytoskeletal dynamics on PAA substrates

In the previous section, I investigated the retrograde flow and traction force response to a broad range of mechanical parameters using the viscoelastic motor clutch model (section 5.2). To gain a deeper understanding of how axons grew on the elastic and viscoelastic substrates (section 4.2) I simulated the axon velocity according to their specific mechanical properties (Figure 18a-d). For each substrate type (soft and stiff elastic (100 Pa E and 1 kPa E) and viscoelastic (100 Pa VE and 1 kPa VE) gels), I measured the mechanical properties using AFM (Figure 18a) and then fitted the force-indentation or indentation-time curves to a Hertz model or SLM (Figure 18b-c), and finally with these parameters I simulated axon velocity on that substrates according to the Hertz parameters (elastic) or SLM parameters (viscoelastic) (Figure 18d). It was possible to measure the Hertz and SLM parameters for elastic and viscoelastic gels as shown in section 4.2.

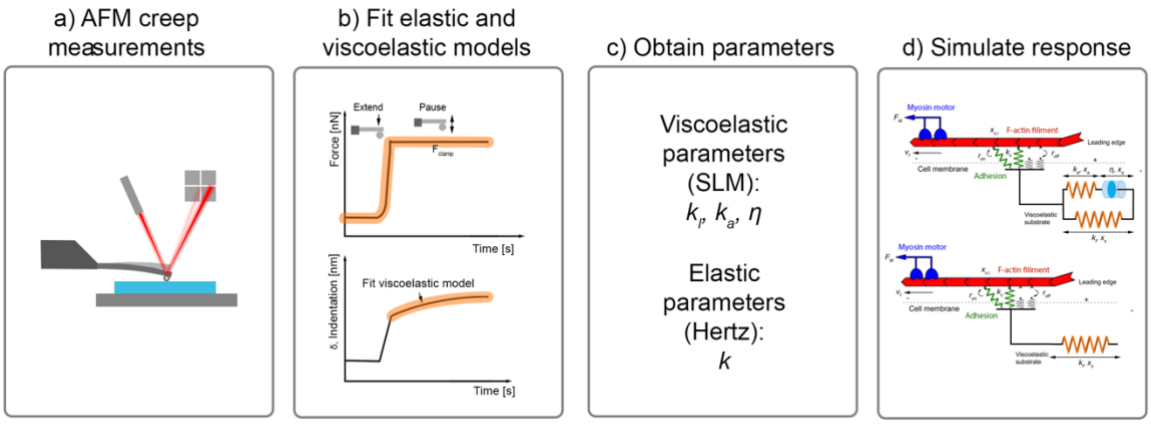

Figure 18 Workflow for predicting axon velocities on difference substrates.

a) AFM creep measurements were first made on elastic and viscoelastic substrates. b) AFM creep was modelled using different elastic and viscoelastic models. c) Viscoelastic (SLM) and Elastic (Hertz) parameters were obtained from mechanical models. d) Mechanical parameters were used to simulate axon response for interactions with elastic and viscoelastic substrates.

According to the elastic motor clutch model (using the Hertz stiffness only to model the substrate), simulated axon velocities were predicted to be lower on soft elastic substrates (median = 13.10 nm/s) compared to stiff elastic substrates (median = 15.68 nm/s) The elastic motor clutch model (using the Hertz stiffness only to model the substrate) also predicted higher simulated axon velocities on stiff viscoelastic substrates (median = 17.81 nm/s) compared to soft viscoelastic substrates (median = 16.45 nm/s) (Figure 19a, red). Therefore, the elastic model predicted higher axon velocities on stiff elastic and viscoelastic substrates suggesting that axons should travel further (Figure 19a, blue). Given that all the substrates exhibited some degree of creep during the AFM experiments (Figure 12e), it was possible to simulate the axon velocity for the viscoelastic case (Figure 19b). To simulate axon velocities in a viscoelastic case I fitted displacement-time data for each substrate (elastic and viscoelastic) to the SLM and then used the SLM parameter to simulate axon velocities.

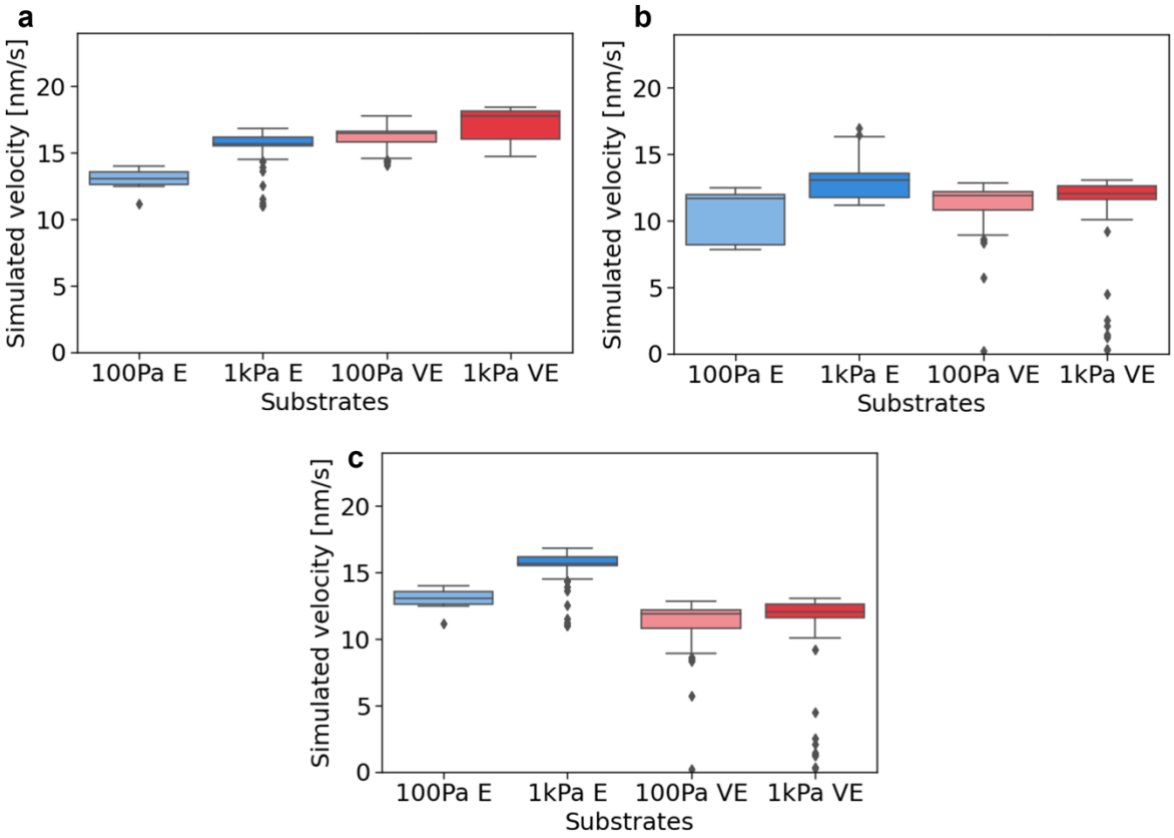

Figure 19 Simulated axon velocities based on the motor clutch model on elastic and viscoelastic substrates.

a) Simulated axon velocities using an elastic motor clutch model for each substrate (100 Pa E and 1 kPa E N=147, 100 Pa VE and 1 kPa VE N=124). The Hertz stiffness from AFM measurements were used to model substrate mechanics for the elastic motor clutch model. b) Simulated axon velocity using viscoelastic motor clutch model for each substrate (100 Pa E and 1 kPa E N=147, 100 Pa VE and 1 kPa VE N=124). The SLM parameters measured by AFM were used to model substrate mechanics for the viscoelastic motor clutch model. c) Simulated axon growth using the elastic motor clutch model (Hertz stiffness from AFM) for elastic based substrates (blue) and the viscoelastic motor clutch model (SLM parameters from AFM) for the viscoelastic substrates (red) (100 Pa E and 1 kPa E N=147, 100 Pa VE and 1 kPa VE N=124). E = elastic and VE = viscoelastic. The box shows the quartiles (calculated by the interquartile range (IQR)) and the whiskers show the rest of the distribution (1.5 IQR) except for points that are determined to be outliers. Outliers are considered as $Q \pm 1.5$ IQR.

To investigate the effects of substrate viscoelasticity on axon growth velocities, I also simulated the axon growth velocity according to the viscoelastic motor clutch model (Figure 19b). Axons cultured on soft elastic substrates were predicted to grow slower (median = 11.67

nm/s) compared to axons cultured on stiff elastic substrates (median = 13.03 nm/s) (Figure 19b blue). For viscoelastic substrates, axons were predicted to grow slower on soft viscoelastic substrates (median = 11.90 nm/s) compared to stiff viscoelastic substrates (median = 12.04 nm/s) (Figure 19b red). I also paired the simulation type with the substrate type, that is plotting the elastic motor clutch (Hertz stiffness from AFM) simulation results with the elastic substrates and viscoelastic motor clutch (SLM parameters from AFM) simulations with the viscoelastic substrate Figure 19c.

Table 7 Substrate SLM and Hertz mechanical parameters used to simulate temporal response. *Parameters based on AFM force-displacement (for k) and displacement-time (for $k_l, k_a, \eta, and\ \tau$) measurements.*

Names	k_l [Pa]	k_a [Pa]	η [Pas]	k [Pa]	τ [s]
100Pa E	41.28	5.81	16.26	163.72	3.19
1kPa E	84.84	10.49	3.79	1101.39	0.41
100Pa VE	29.64	3.56	0.70	1582.66	0.22
1kPa VE	31.98	2.70	1.09	4124.74	0.44

The results I have presented in this current section (5.3) and section (4.3) suggest from a computational and experimental perspective that axon growth may be regulated by substrate mechanics. I also found that substrates with a characteristic timescale below one second also resulted in longer median axon lengths. To investigate what is going on at a mechanistic level, I wanted to look closer into the load and fail response for the motor clutch model as a function of substrate timescale. To investigate the load and fail response I ran elastic and viscoelastic motor clutch simulations with the parameters outlined in Table 7 to model the temporal response. The parameters are based on the median results from AFM force-displacement and displacement-time measurements presented in Figure 13 for each substrate.

When I simulated the temporal response of axon velocity in the elastic case, when the substrate had a higher timescale ($\tau = 3.13$ s, Figure 20a blue) the axon velocity gradually increased until a failing event occurred (sharp drop in all curves). A failing event occurs when the clutch molecules can no longer support the pulling force of the myosin motors. When the substrate had lower characteristic time scales ($\tau < 1$ s, Figure 20a orange, green, and red) the failure occurred much faster and the simulated axon velocities were much higher for the elastic

motor clutch model. To investigate if this happened differently in a viscoelastic case, I ran the same simulations for a viscoelastic substrate (Figure 20b). For substrates with larger characteristic timescales ($\tau = 3.13$ s, Figure 20a blue) the simulated velocity increase gradually and failure events were much less frequent. Interestingly, this was also the case for substrates with a lower characteristic timescale ($\tau < 1$ s, Figure 20b orange, green, and red).

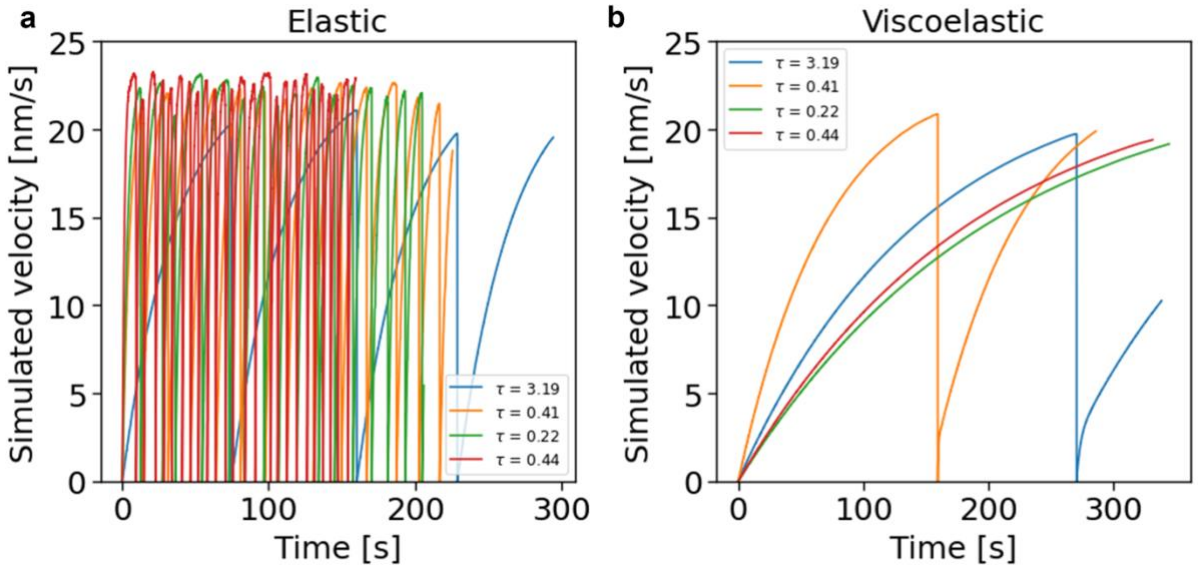

Figure 20 Characteristic substrate timescale regulates temporal axon velocity.

a) Temporal simulated axon velocity response for the elastic motor clutch model. Substrates with a characteristic timescale below 1 second predicted axons to exhibit frictional slippage. b) Temporal simulated axon velocity response for the viscoelastic motor clutch model. All substrates predicted axons to exhibit load-and-fail behaviour according to the viscoelastic motor clutch model.

From a qualitative perspective, the load and fail cycle is different depending on how the substrate mechanics are modelled (Figure 20a-b). The motor clutch model assumes that the velocity (retrograde flow velocity) and force are linearly related, which means the same load and fail cycles occur in the simulated axon traction forces. The elastic response shown for substrates with a lower characteristic timescale ($\tau < 1$ s, Figure 20a orange, green, and red) appear to be transitioning closer to the frictional slippage regime where clutch molecules are loaded very fast and fail (Chan and Odde, 2008). Generally, retrograde flow is higher when there is frictional slippage, whereas retrograde flow is lower in the load-and-fail mode.

5.4. Simulated cytoskeleton dynamics in the developing *Xenopus* brain

To test the predictions of my simulations for retinal ganglion cell axons growing through the developing *Xenopus* brain, I mapped the mechanical properties of *in vivo* brain tissue at cellular

resolution using AFM (Figure 18a) and then fit the force-indentation or indentation-time curves to a Hertz model or SLM model, respectively (Figure 18b-c). For each AFM measurement, i.e., pixel of the AFM map, I obtained the Hertz parameter (k) and SLM parameters (k_l, k_a, and η). I simulated axon velocity in each pixel according to the Hertz parameters (elastic) or SLM parameters (viscoelastic) (Figure 18d). Subsequently, I generated simulated velocity and traction force maps of the developing *Xenopus* brain that spatially predict the axon response within the brain.

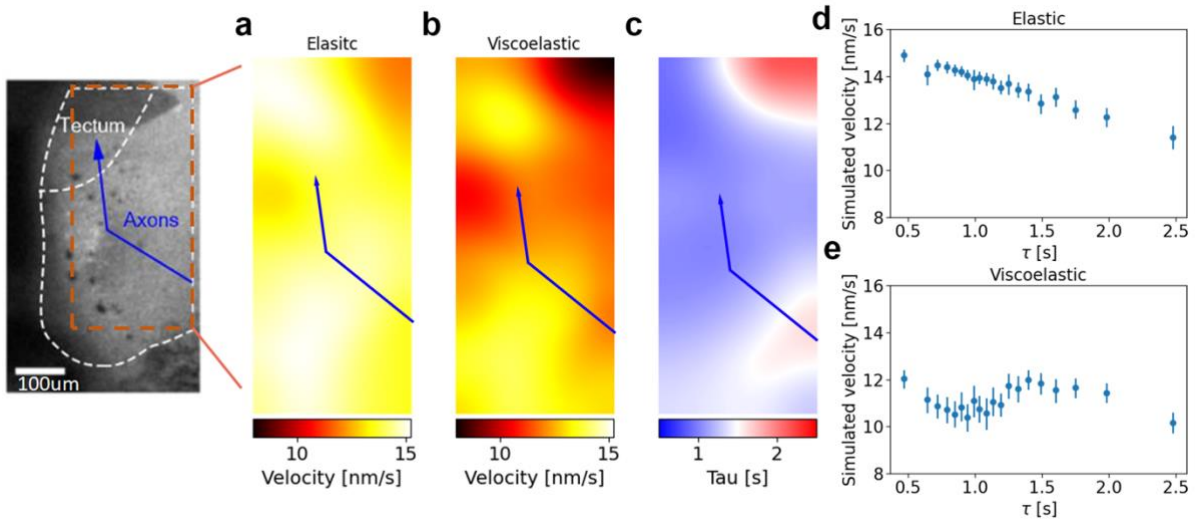

Figure 21 Motor clutch model predicts heterogenous axon velocity field in the developing Xenopus brain.

a) Representative simulated axon velocity field in the developing Xenopus brain according to the elastic motor clutch model. b) Representative simulated axon velocity field in the developing Xenopus brain according to the viscoelastic motor clutch model. Brighter pixels in a) and b) indicate that axons would travel faster in that region of the brain. c) Characteristic timescale map of the developing Xenopus brain. d) Simulated axon velocity as a function of brain tissue characteristic timescale for elastic motor clutch simulations. The Hertz model was used to model the substrate and the SLM parameters were used to get substrate timescale. The Hertz model and SLM parameters are obtained in the same force curve. e) Simulated axon velocity as a function of brain tissue characteristic timescale for viscoelastic motor clutch simulations. Data points were binned into 20 bins.

I simulated the axon velocity field according to the elastic and viscoelastic motor clutch model (Figure 21a-b). The elastic motor clutch model predicted that axons should travel at different velocities in different regions of the brain as shown in Figure 21a. In regions of the

brain that are typically stiffer, the elastic motor clutch simulations predicted higher axon velocities, whereas in typically softer regions, axon velocities were lower. The results suggest that the variations in elasticity should regulate the axon velocity. I repeated the same analysis for the viscoelastic motor clutch model (Figure 21b). Similar to the elastic case, the viscoelastic motor clutch model predicted heterogenous axon velocities within the brain. Regions of the brain that exhibit higher stiffnesses and viscosities correlated with higher axon velocities, whereas elastically softer and less viscous regions led to lower axon velocities. This suggests that the viscoelastic properties of the brain tissue could regulate axon velocities.

In the previous section (5.3), I found that the viscoelastic simulations were correlated with *in vitro* experiments and that substrates with a characteristic timescale below one second resulted in longer median axon lengths. For that reason, I wanted to investigate spatial variations in the characteristic timescale in the developing *Xenopus* brain (Figure 21c). The characteristic timescale of the brain varied spatially (Figure 21c). When a force is applied to regions of the brain with a higher characteristic timescale, there will be more of a delayed displacement response. For regions with a lower characteristic timescale, the displacement response will be more instantaneous.

To investigate the relationship between the characteristic timescale and simulated axon velocities, I visualized the relationship (Figure 21d-e). According to the elastic motor clutch model, the simulated velocity decreased when the characteristic timescale of the brain tissue increased. Therefore, the model predicts that axons should travel faster when the brain tissue has a shorter characteristic timescale, while if the brain has a longer characteristic timescale the model predicts lower axon velocities (Figure 21d). Interestingly, the viscoelastic motor clutch model predicted a biphasic response in the simulated axon velocity as shown in Figure 21e. At short characteristic timescales ($\tau < 1$ s) axon velocity was predicted to decrease but at timescales between ($1 < \tau < 1.5$ s) the simulated velocity was predicted to increase again. At longer timescales ($\tau > 1.5$ s) axons were predicted to travel with decreasing velocities (Figure 21e). Further work would be required to determine which model better predicts the velocity field. For example, axons velocity profiles could be measured *in vitro* along with viscoelasticity maps (as Thompson et al. (2019) did for elastic maps) and directly compared to elastic and viscoelastic simulations. This would make it possible to determine which model best describes axon growth.

In this section, I have investigated how the elastic and viscoelastic motor clutch models predict axon velocities in the developing *Xenopus* brain. I found that both models predict

heterogeneous velocity fields which suggests that axons travel at different velocities within the brain. Although this result is interesting it does not provide an explanation of the growth trajectories of axon bundles. In future work, the velocity field from this work could be used to simulate axon trajectories according to the methods presented by Oliveri et al. (2021).

5.5. Discussion

5.5.1. Importance of viscoelasticity in the motor clutch model

As discussed in chapter 4, the median axon length on soft and stiff viscoelastic gels exhibited the same behaviours. I found that the characteristic timescale of the substrate was correlated to the median axon length. In recent literature, it has been reported that the motor clutch model can be used to predict cell spreading speed (Gong et al., 2018) and mechantransduction (Elosegui-Artola et al., 2018). The motor clutch model directly links cytoskeletal dynamics to substrate mechanics. Using the viscoelastic motor-clutch model, I performed a grid search to predict the retrograde flow and traction forces across a broad range of stiffnesses and viscosities (Figure 17). The simulations predicted a biphasic response in retrograde flow as a function of long-term stiffness (k_l) for different additional stiffnesses (k_a) in agreement with previous literature and the elastic motor clutch model (Chan and Odde, 2008, Bangasser et al., 2013, Bangasser et al., 2017). Here, I will focus on retrograde flow but it's important to note that it's generally inversely related to traction force generation (that is low retrograde flow implies high traction force and high retrograde flow implies low traction force).

In the elastic motor clutch model, the retrograde flow started high and then started to decrease as a function of substrate timescale. Note that substrate timescales were obtained from the SLM parameters which were recorded during the same AFM measurement. Retrograde flow decreases as adhesions build up and progressive loading occurs until failure (load and fail cycles). As the stiffness increased, frictional slippage started to occur and retrograde flow increased because adhesion was low. My simulations suggested that, as a viscous component is introduced, the load and fail cycle is perturbed (Figure 17b, green dotted line). I also plotted the range of viscosities and long-term stiffnesses on the maps (Figure 17, green and blue boxes) which illustrates that both the substrates and *Xenopus* brain tissue mechanics predict that the cytoskeleton should be in the load and fail regime. Ideally, the grid search would be performed for a greater range of additional stiffness values, but this would be hard to visualise.

It is possible to use the motor clutch model using an elastic or viscoelastic substrate. I measured the elastic and viscoelastic mechanical properties of the substrates and used these values to simulate axon growth velocities. Here, I assumed that the growth rate of the axon was

$v_{axon} = v_p - v_r$, where v_p is the polymerization rate of actin filaments and v_r is the retrograde flow (this is the parameter that is simulated). This assumption was used by Gong et al. (2018) but may be limited by the fact it has not been measured on substrates with varying mechanical properties. However, it has been reported that growth cone advancement is inversely proportional to retrograde flow (Lin and Forscher, 1995).

The elastic motor clutch model predicted an increasing axon growth velocity as a function of elastic stiffness (measured by AFM and fitted to the Hertz model) (Figure 19a). However, the median axon length did not follow this same trend (Figure 14b) suggesting that the elastic motor clutch model is not sufficient to explain the results according to the AFM data. The viscoelastic motor predicted (Figure 19a) a similar trend to the *in vitro* median axon velocity data (Figure 14b). My results thus suggested that the viscoelastic motor clutch model is a better approximation of axon growth velocity compared to the elastic model.

Andreu et al. (2021) demonstrated that the force loading rate can regulate mechanosensing in fibroblasts and it explainable by the elastic motor-clutch model. The loading rate of the forces on the elastic and viscoelastic gels can be calculated by multiplying the resting velocity (v_u) by the long-term stiffness (k_l). The loading rates on 100 Pa elastic substrates (0.9 pN/s) were lower compared to 1 kPa elastic substrates (2 pN/s). Whereas the loading rates were almost the same on soft and stiff viscoelastic substrates (100 Pa: 0.71 pN/s vs 1 kPa: 0.76 pN/s). Their results suggest that a higher loading rate leads to reinforcement and adhesion growth at the local level. Therefore, it would be expected that axons on 1 kPa substrates undergo more reinforcement and have larger adhesions compared to all the other substrates. It would be interesting to measure the size of paxillin adhesions in future work to see if substrate stiffness can be used to infer adhesion dynamics.

Based on the work of Andreu et al. (2021) it would be expected that the loading rate is linked to the lifetime of focal adhesions and subsequently the substrate timescale. The characteristic lifetime associated with loading the substrate (τ_l) can be calculated by $\frac{F_m N_m}{v_u k_l}$ which describes the time it takes the clutches to stall the motor force. F_m is the force applied by a single myosin motor, N_m is the number of myosin motors, $v_u$is the unloaded velocity of an actin filament, and k_l is the long-term stiffness. Larger τ_l means that it takes longer for the myosin motors to stall. τ_b is defined as the time that it takes for clutches to bind clutch molecules between the substrate and actin filaments. Finally, τ_s is the characterise timescale of the substrate. Gong et al. (2018) classified three different growth regimes based on the timescales of the substrate, loading rate, and focal adhesions.

- State I ($\tau_s < \tau_b$): The ECM relaxes fast and exhibits its long-term stiffness (k_l) in reference to the clutch binding time. In this regime, the effects of viscosity are negligible.
- State II ($\tau_b < \tau_s < \tau_l$): In this regime the cell first feels the effective stiffness ($k_a + k_l$) and then starts to feel the long-term stiffness of the substrate. Subsequently, retrograde flows are suppressed, and growth velocity is enhanced.
- State III ($\tau_s < \tau_l$): In this regime, the substrate does not relax during the lifetime of the focal adhesions and hence the substrate behaves elastically.

For each of the substrates, I determined the regime according to these criteria. I found that axons on 100 Pa elastic substrates were in the $\tau_b < \tau_s < \tau_l$ regime. The rest of the substrates were in the $\tau_s < \tau_b$ regime, suggesting that the effects of viscosity are negligible. This may explain why the substrates with a lower timescale ($\tau_s < 1\ s$) exhibited a similar simulated axon velocity and *in vitro* median axon length.

5.5.2. Role of viscoelasticity in axon guidance according to motor clutch model

To understand how substrate viscosity was affecting the growth of axons, I wanted to understand how the cytoskeletal dynamics differs on different substrates. I demonstrated that across certain viscoelastic brain tissue properties simulated axon growth can be regulated by the local tissue viscosity. Antonovaite et al. (2021) demonstrated that rodent brain tissue exhibits heterogeneous viscoelasticity, and it has been well established that the brain tissue is viscoelastic. However, it is unknown how and if the viscoelasticity of brain tissue regulates the growth process during development. For that reason, I used the elastic and viscoelastic motor clutch model to predict the growth dynamics of axons in the brain tissue based on the viscoelasticity.

The elastic motor clutch predicted that axons should travel faster compared to the viscoelastic motor clutch model. However, this does not mean that viscoelasticity is negligible because according to the AFM measurements, brain tissue is not purely elastic. In the previous discussion (5.5.1), I outlined how Gong et al. (2018) used different cellular timescales to determine if the viscous component was important or not. I followed the same procedure for the simulations based on the mechanics of the brain tissue to work out what growth state axons were in during development. I found that 85.4 % of simulations (N = 2368 unique simulated positions from the developing brain tissue) predicted that axons would be growing in what Gong et al. (2018) defined as state II ($\tau_b < \tau_s < \tau_l$), suggesting that the effects of viscosity are

not negligible in the context of brain tissue viscoelasticity. In 13.4 % of simulations (N = 2368 unique simulated positions from the developing brain tissue) axons were predicted to be growing in state I ($\tau_s < \tau_b$) which indicates the effects of viscosity are negligible. Finally, 1.2 % of simulations (N = 2368 unique simulated positions from the developing brain tissue) axons were predicted to be growing in state III ($\tau_s < \tau_l$) which indicates that elastic stiffness predominantly governs axon growth dynamics in this state.

My provisional results suggest that it is important to consider viscoelasticity during the growth of axons during development. Previously published work from Koser et al. (2016) and Thompson et al. (2019) has demonstrated that tissue elasticity is important during the development of the optic tract. Yet, my simulations suggest that it may be a combination of elastic and viscous tissue properties that are driving the growth. In future work, it would be interesting to map how brain tissue viscoelasticity evolves while axons undergo a stereotypical caudal turn in the mid-diencephalon towards the optic tectum. However, one of the downsides of my simulations is that it is hard to validate *in vitro* in the range of viscoelastic properties measured in the brain (due to limitations of material chemistry and gel fabrication). One solution would be to image axon dynamics in the brain *in vivo* as reported by Thompson et al. (2019).

5.5.3. Limitations and general model parameters

In this chapter I used a viscoelastic motor-clutch model to predict axon growth based on the mechanics from substrates and brain tissue. I used the parameters that were previously reported by Chan and Odde (2008) and Gong et al. (2018) to configure the simulations. However, the parameters that are used to configure the motor-clutch simulations influence the predicted retrograde flow rates and traction forces. Ideally, parameters are calibrated for the cell system in question and then the model can be used to simulate the traction forces and retrograde flow rates. Since the parameters were not specifically tuned for the cell system used in this thesis, I will outline the key parameters and how they can impact the simulation results.

First, the parameters can be grouped into motor (n_m, F_m, v_u) and clutch (n_c, r_{on}^0, r_{off}^0, F_b, k_c) parameters. The motor parameters configure how myosin motors pull on the actin filaments and the clutch parameters configure how the clutch molecules stochastically bind/unbind actin filaments to the substrate. Bangasser et al. (2013) investigated how these parameters effect the retrograde flow rates and traction forces in an elastic motor-clutch model using single and dual parameter changes. The influence of parameters for a viscoelastic model have not been explored to date so only the elastic analysis will be discussed in this section.

Depending on the parameters that are used to configure the simulations the system can exist in a stalled state, load-and-fail state, or free-flowing state. In the stalled state there is near zero actin retrograde flow while in the free-flowing state actin retrograde flow is at a maximum. In the load-and-fail state a continually increasing force (i.e. load) is applied to the substrate until adhesions break (i.e. fail) and this process is repeated. The dynamics of the load-and-fail cycle vary as a function of stiffness and there is an optimum stiffness whereby traction forces are maximised (and retrograde flow rates are minimized). Generally, alterations in the model parameter influence the load-and-fail dynamics and hence the optimal stiffness.

Bangasser et al. (2013) used a metric to measure the maximum order of magnitude change in optimal stiffness as a function of parameter change to understand which parameters are key in determining the behaviour of the motor clutch model. Each of the parameters had a limited range whereby the optimal stiffness could be shifted by up to 2.6 orders of magnitude in the load-and-fail cycle. Outside this limited range the system would result in a stalled or free-flowing state. It was found that parameters such as the clutch on rate (r_{on}^{0}) had the greatest impact on the model predictions. While parameters such as the clutch stiffness (k_c) had little impact on the model predictions. In general, that authors found that single parameter changes that strengthen the clutches increase the optimal stiffness while increases in the motor parameters have the opposite effect. The simulations were generally more sensitive to the clutch parameters compared to the motor parameter. Therefore, in future work the effects of the clutch parameters for the viscoelastic motor clutch model should be investigated in further detail.

It has been observed experimentally that cells can exhibit differences in traction forces greater than 2.6 order of magnitude. This means that single parameters change in the motor clutch model are not sufficient to explain experimental observations. To explore this further the Bangasser et al. (2013) investigated the effects of dual parameter changes which can lead to changes in the optimal stiffnesses of up to 5 orders of magnitude. For example, increasing only the number of clutches would generally result in a stalled system but if the number of motors is also increased by the same number the load-and-fail behaviour of the system is preserved while the optimal stiffness is increased. Generally, by increasing a parameter that strengthens the clutch it can be compensated by an increase in a parameter that strengthens the motors giving rise to larger dynamic behaviour. The duel and harmonized change in parameters could explain the differences in traction forces for different cell types and permits tuning of the model.

The work of Bangasser et al. (2013) illustrates the importance of motor clutch parameters and how they influence the load-and-fail dynamics. A major limitation of the simulations presented in this work is that model parameters were used from literature and not fitted to experimental data. Bangasser et al. (2013) found that the number of myosin motor (n_m), number of clutch molecules (n_c), force threshold (F_b), clutch on rate (r_{on}^0), and clutch off rate (r_{off}^0) have the greatest effect on the predictions of the elastic motor clutch model. Therefore, the parameters n_m, n_c, F_b, r_{on}^0, and r_{off}^0 would be a good starting point to understand the dynamics of the viscoelastic motor clutch system.

For the elastic model, the number of myosin motors (n_m) and clutch molecules (n_c) have the greatest effect on the magnitude of the traction forces of these parameters (Bangasser et al., 2013). In the following chapter, I measured the mean forces growth cones applied and they were on average in the range of ~10 pN which would suggest the number of motors and clutches is in the range of 50 – 100 (in this work $n_m = n_c = 75$). Furthermore, frictional slippage is usually observed on glass substrates for growth cones (Chan and Odde, 2008). Therefore, the retrograde flow of actin on glass substrates is likely close to the unloaded actin velocity (v_u). In the following chapter, the retrograde flow rate on glass was measured to be ~ 100 nm/s (Figure 26e) indicating that the unloaded actin velocity should be in the range of 100 nm/s (in this work $v_u = 120$ nm/s).

Although some of the parameters were in the correct range this should be validated experimentally in future work. It would also be insightful to perform the same analysis as Bangasser et al. (2013) for a viscoelastic clutch model. However, it would be challenging to repeat the same analysis from Bangasser et al. (2013) in a viscoelastic parameter space because there is not just an optimal stiffness but an optimal viscoelastic model. An optimal viscoelastic model would have an optimal stiffnesses (k_l and k_a) and viscosity (η) which would significantly increase the parameter space to be searched. Albeit the simulations presented in this thesis provide a good starting point to predict the behaviour of axon growth as a function of viscoelasticity. By carefully reviewing and testing different parameter in future work the model could be used to better understand axon growth.

5.6. Summary

In this section, I have demonstrated that the motor clutch model can be used to simulate axon growth in the context of an elastic and viscoelastic substrates. Furthermore, I found that the viscoelastic motor clutch model was a better approximation of axon growth for elastic and viscoelastic substrates and that the substrate timescale could be important in regulating the

axon velocity. Using physiologically relevant mechanics I simulated axon growth velocity fields in the developing *Xenopus* brain and identified that the characteristic timescale of the brain tissue may regulate the growth velocity. It would be interesting to measure growth velocities *in vivo* in future experiments to determine if the motor clutch model can be used to predict the trajectory of axons *in vivo* only based on mechanics.

5.7. Acknowledgements

H. Oliveri (Mathematical Institute, University of Oxford) for discussions about simulating axon trajectories.

Chapter 6: Cytoskeletal dynamics of axon growth

6.1. Background

In the previous chapters, I found that the developing *Xenopus* brain exhibits heterogenous viscoelasticity (section 3.5) and that viscoelasticity regulates axon length (section 4.3). Furthermore, the effects of viscoelasticity were explainable using the viscoelastic motor clutch model. In the previous section, I computationally investigated the cytoskeletal dynamics and mechanical interaction of growing axons on different elastic and viscoelastic substrates. The motor clutch model predicts axon velocity, retrograde flow rates, and traction forces. To confirm the validity of the viscoelastic motor clutch model in the context of axon growth, I investigated the cytoskeletal dynamics and traction force generation during axon growth on different substrates. To enable efficient data analysis, I developed new software for analysing traction forces with optimised regularisation and efficiency, which I will present first.

6.2. Traction force microscopy analysis

Conceptionally, traction force microscopy first appears to be a very simple experiment. In essence, all that needs to be done is to capture an image of a gel embedded with beads that has not been deformed (the reference frame) and then capture a series of images when the gel is deformed (sample frame). To reconstruct the stresses introduced on the surface all that needs to be done is to calculate the distance for which the beads are displaced and divide the displacement field by the Young's modulus and normalize per unit area.

However, each of these steps comes with several technical difficulties. To automate traction force microscopy analysis, I developed the general processing workflow which is also illustrated in Figure 22:

1. Load and normalized a reference bead frame and sample frame along with the region of interest (Figure 22a)
2. Use a k-nearest neighbours' algorithm to approximate the optimum window size for the iterative PIV algorithm (Figure 22b)
3. Perform an iterative PIV to obtain a discretized displacement field (Figure 22c)
4. Use the ROI boundary to compute the noise ($\beta = \frac{1}{var}$) (Figure 22d)
5. Convert vector field to Fourier space (Figure 22e)

6. Find the optimal regularization parameter based on evidence (Figure 22e)
7. Compute traction map with optimal regularization parameter (Figure 22e)
8. Write results to Hierarchical Data Format file (HDF5) with pandas DataFrame like behaviour.

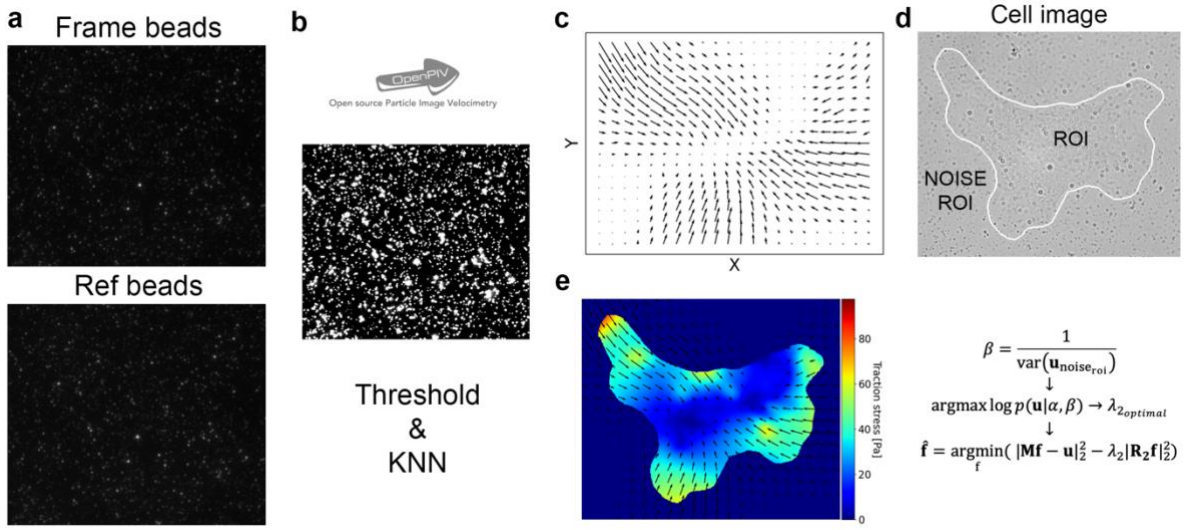

Figure 22 Workflow of pytraction python package for traction force microscopy analysis.

a) frame beads and ref beads images are loaded. The frame beads are the current position of the beads while the cell is attached to the substrate. The ref beads images are the position of the beads once the cell is detached from the substrate. b) A threshold is applied to the frame beads and the bead coverage is computed ($\frac{\sum_n^i pixel_i}{n}$) *and passed to a pretrained k-nearest neighbours' algorithm to determine the window size for the iterative PIV. c) The displacement field is calculated using OpenPIV (http://www.openpiv.net/) based on the window size from b). d) The ROI is used to group vectors outside the cell boundary for the noise calculation. e) Noise is used as the variance to maximize the log evidence to find the optimal* λ_2 ($\lambda_{2_{optimal}}$) *which is then used to compute the forces induced from the displacements.*

There are many existing tools for analysing TFM data but they generally require expert knowledge to fine tune regularization parameters, have poor or inaccessible documentation, require access to commercial software licenses, require the users to manually pick the L2 regularization parameter, and/or are computationally expensive. For that reason, I wrapped up my analysis workflow into a simple Python package called pytraction (https://github.com/rg314/pytraction) to make TFM analysis simple and accessible to

everyone. I optimized the asymptotic computational complexity of the code and designed an abstraction that enabled users to perform analysis in just a few lines of code:

```
# import visualization library
import matplotlib.pyplot as plt

# import pytraction and key component
from pytraction import TractionForceConfig, plot, process_stack

pix_per_mu = 9.8138 # Pixel per um
E = 1000  # Young's modulus in Pa

# add the paths for image, references, and roi
img_path = "data/example2/1kPa-2-Position006.tif"
ref_path = "data/example2/1kPa-2-Position006_ref.tif"
roi_path = "data/example2/1kPa-2-Position006.roi"

# add path for the configuration file
config = "config/config.yaml"

# create an instance of the configuration object
traction_config = TractionForceConfig(E=E, scaling_factor=pix_per_mu, config=config)

# load the data based on the configuration object
img, ref, roi = traction_config.load_data(img_path, ref_path, roi_path)

# process the data using pytraction
# the results are returned as a HDF5 like dataframe
results = process_stack(img[:1, :, :, :], ref, config=traction_config, roi=roi, crop=True)

# plot traction force maps
plot(results, frame=0)
plt.show()
```

In essence, I reduced the TFM workflow into three lines of code that includes defining the configuration, loading the data, and running the analysis. The workflow behind the analysis is outlined in Figure 22. To enhance the experience of the software package I saved the data from the analysis in a Hierarchical Data Format (HDF5) which enables the user to load data fast because only specified parts are loading into RAM. Furthermore, to simplify the usage of

HDF5, I built a wrapper around the file that emulated the behaviour of a pandas DataFrame which many python users will be familiar with. Note this could still be challenging for some biologists with no programming experience.

In the current section, I have outlined the workflow behind pytraction which makes the analysis of TFM data easier and simpler for users without needing a deep understanding of the analysis. Compared to packages such as the DanuserLab TFM MatLab package and the Traction Force Microscopy ImageJ plugin, pytraction offers a simpler solution by simplifying the whole process into a few lines of code with automatic regularization and fast computation.

6.3. Force generation and axon velocity of *Xenopus* eye primordia explants

In the previous chapters, I found that viscoelasticity regulates axon length (section 4.3) and that this could be explained using the viscoelastic motor clutch model (section 5). To confirm the validity of the viscoelastic motor clutch model in the context of axon growth, I wanted to measure force generation and axon velocity during the growth process. I cultured *Xenopus* eye primordia explants on soft (100 Pa) and stiffer (300 Pa) elastic substrates. I was unable to resolve bead displacements on 1 kPa substrates because growth cone forces were not strong enough to deform the substrates. Furthermore, I tried to perform TFM on the viscoelastic gels, but it was not possible to get a uniform bead distribution for imaging.

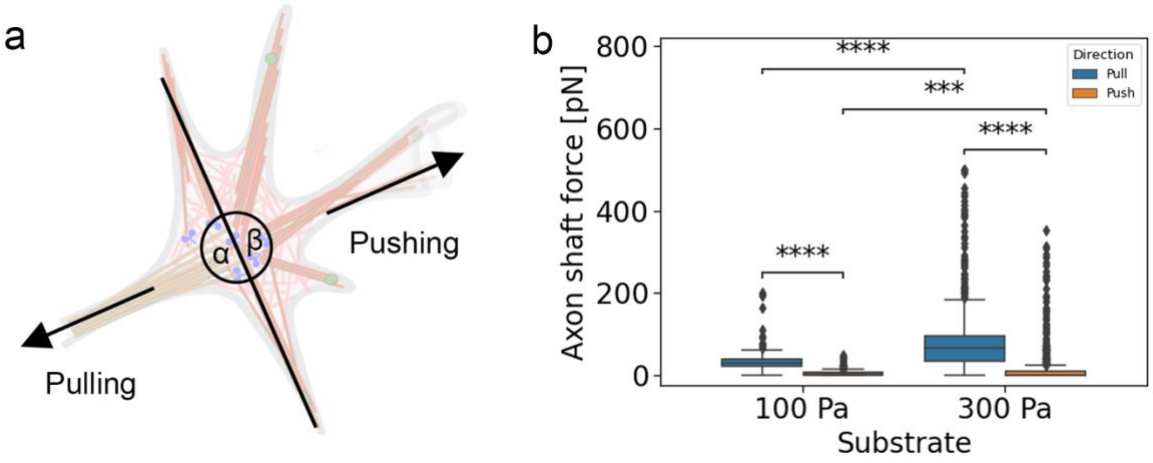

Figure 23 Axon growth cones act as "pulling" force generators. Axon growth cones apply a pulling force to the substrate as they undergo outgrowth, and the pulling force is regulated by substrate stiffness.

a) Schematic of axon growth showing the direction of net pulling and net pushing forces. Forces at angles in the range of α were considered as pulling forces and forces at angles in the range of β were considered as pushing. b) Pulling forces parallel to the axon shaft on 100 Pa (N=196) and 300 Pa (N=780) substrates. Pulling forces were significantly higher on stiffer substrates. Pushing forces on 100 Pa and 300 Pa substrates. There were significant differences between pushing forces on 100 Pa and 300 Pa substrates. Pulling forces were significantly higher on 100 Pa and 300 Pa substrates compared to pushing forces. Mann-Whitney U-test $Ns: p \leq 1$, $*: 1 \times 10^{-2} < p \leq 5 \times 10^{-2}$, $**: 1 \times 10^{-3} < p \leq 1 \times 10^{-2}$, $***: 1 \times 10^{-4} < p \leq 1 \times 10^{-3}$, $****: p \leq 1 \times 10^{-4}$. *The box shows the quartiles (calculated by the interquartile range (IQR)) and the whiskers show the rest of the distribution (1.5 IQR) except for points that are determined to be outliers. Outliers are considered as* $Q \pm 1.5$ *IQR.*

After culturing explants, I imaged bead displacement in 5-minute intervals and analysed force generating growth cones using pytraction which I described in the previous section (6.2). Using the force field, I computed the net forces along the axis of the axon shaft. For each discrete force vector, I classified it as a 'pulling' force or 'pushing' force. For example, force vectors falling within the range of α were considered as pulling forces and forces at angles in the range of β were considered as pushing (Figure 23a). For each force I calculated the net force parallel to the axon shaft and summed them to obtain the net pushing or pulling force shown in Figure 23b-c. I found that growth cones on softer substrates (100 Pa) generated a significantly lower net force along the axon shaft (31.54 ± 26.22 pN) compared to those on

stiffer substrates (300 Pa, 78.94 ± 78.85 pN). There were significant differences between the pushing forces generated on soft substrates (100 Pa, 4.86 ± 8.93 pN) compared to stiff substrates (300 Pa, 16.32 ± 43.54 pN). Pulling forces were significantly higher on both substrates compared to pushing forces.

Furthermore, I also wanted to understand how traction forces are related to axon advancement. The motor clutch model predicts that higher traction forces should result in greater axon velocities. For each force generating growth cone, I measured the axon velocity and growth cone velocity (Figure 24a-b). The axon velocity was defined by the distance the axon travelled over the imaging time (i.e. $v_{\text{axon}} = \frac{|\overrightarrow{p_0}+\overrightarrow{p_n}|}{t}$, where p_0 is the initial axon position and p_1 is the final position at time t). The growth cone velocity was defined as the total path of the growth cone over the imaging time (i.e. $v_{gc} = \frac{\sum_{i=0}^{n}|\overrightarrow{p_i}+\overrightarrow{p_{i-1}}|}{t}$). The growth cone velocity can be different from the axon velocity because the growth cone can take different paths (i.e. shorter or longer) to get to the final position. The axon velocity does not capture this information.

The axon velocity, that is, the average distance between proximal and distal ends of the axons over the imaging interval (at least 30 mins) were not significantly different ($P = 0.76$) on 300 Pa substrates (8.3 ± 4.8 nm/s Figure 24a) compared to 100 Pa (6.7 ± 2.9 nm/s Figure 24a). I also measured the absolute distance travelled by the growth cone per unit time (5 minute interval) and found that the velocities were not significantly ($P = 0.58$) different 300 Pa substrates (13.8 ± 7.4 nm/s Figure 24b) compared to 100 Pa substrates (11.2 ± 4.45 nm/s Figure 24b).

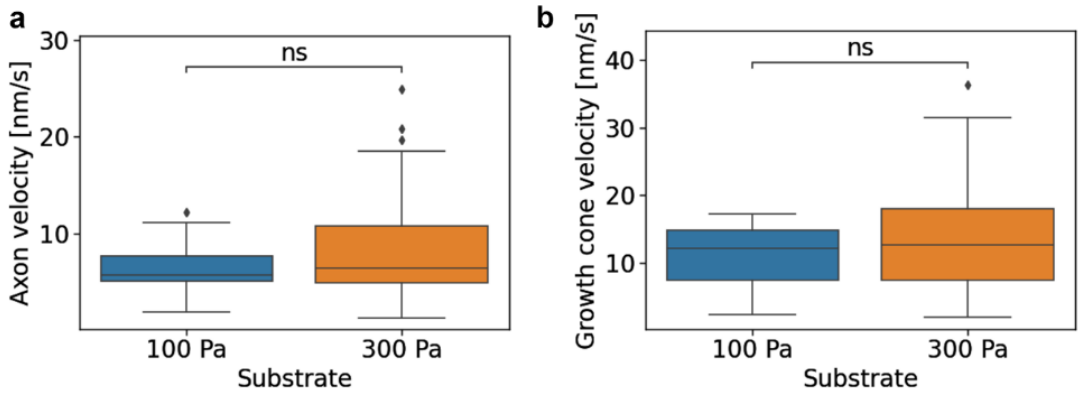

Figure 24 Axon and growth cone velocities on soft substrates.

Axon velocities and growth cone velocities on compliant substrates and velocity-force relationship. a) Axon velocity on soft (100 Pa N=61) and stiff (300 Pa N=73) substrates. The axon velocity is a measure of the net distance that the axon travelled. b) Growth cone velocity on soft (100 Pa N=61) and stiff (300 Pa, N=73) substrates. The growth cone velocity is a measure of the absolute distance that the growth cone travelled. Mann-Whitney U-test $Ns: p \leq 1$, $*: 1 \times 10^{-2} < p \leq 5 \times 10^{-2}$, $**: 1 \times 10^{-3} < p \leq 1 \times 10^{-2}$, $***: 1 \times 10^{-4} < p \leq 1 \times 10^{-3}$, $****: p \leq 1 \times 10^{-4}$. *The box shows the quartiles (calculated by the interquartile range (IQR)) and the whiskers show the rest of the distribution (1.5 IQR) except for points that are determined to be outliers. Outliers are considered as* $Q \pm 1.5\ IQR$.

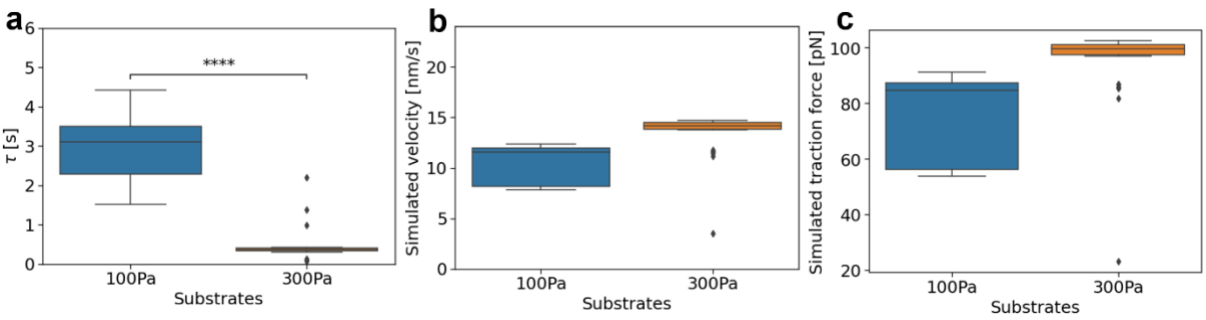

Figure 25 Motor clutch simulations predict higher velocities and traction forces for 300 Pa substrates compared to 100 Pa substrates.

Characteristic timescale of traction force microscopy substrates and simulated velocities and traction forces. a) characteristic timescale of 100 Pa and 300 Pa substrates. b) Simulated axon velocities according to the viscoelastic motor clutch. c) Simulated traction forces according to the viscoelastic motor clutch model. Parameters for the viscoelastic motor clutch model were obtained from fitting the SLM to AFM data. Mann-Whitney U-test $Ns: p \leq 1$, $*: 1 \times 10^{-2} < p \leq 5 \times 10^{-2}$, $**: 1 \times 10^{-3} < p \leq 1 \times 10^{-2}$, $***: 1 \times 10^{-4} < p \leq 1 \times 10^{-3}$, $****: p \leq 1 \times 10^{-4}$. *100 Pa N=42 gels and 300 Pa N=34 gels. The box shows the quartiles (calculated by the interquartile range (IQR)) and the whiskers show the rest of the distribution (1.5 IQR) except for points that are determined to be outliers. Outliers are considered as* $Q \pm 1.5$ *IQR.*

In the previous section, I found that substrates with a characteristic time scale less than one second resulted in longer median axon lengths. To investigate if there were difference in characteristic time scale for 100 Pa and 300 Pa TFM substrates, I measured the characteristic time scale (using SLM parameters fitted to AFM data). I found that the 100 Pa substrates had a significantly higher characteristic timescale ($\tau = 3.08 \pm 1.4$ s, Figure 25a) compared to the 300 Pa substrates ($\tau = 0.44 \pm 0.38$ s, Figure 25a). To further compare my experimental results to the motor clutch simulations I wanted to compare the axon and growth cone velocities and traction forces. The viscoelastic motor clutch model predicted that axons travelled slower (11.59 ± 1.91 nm/s, Figure 25b) on 100 Pa substrates compared to 300 Pa substrates (14.17 ± 2.06 nm/s, Figure 25b). Finally, the motor clutch model also predicted that traction forces should be higher on 300 Pa substrates (99.5 ± 14.0 pN, Figure 25c) compared to 100 Pa substrates (84.8 ± 15.5 pN, Figure 25c) which also matches the trends seen in Figure 23a. It was not possible to directly compare these forces with those measured experimentally as this would require some approximation of focal adhesion sizes, which was not performed.

In this section (6.3), I investigated how substrate stiffness regulates growth cone force generation and advancement *in vitro*. Growth cones exert "pulling" forces on substrates and

the substrate stiffness regulates the magnitude of the pulling forces. I found no significant differences in absolute growth cone or axon velocities on 300 Pa substrates compared to 100 Pa substrates.

6.4. Actin and microtubule dynamics on compliant substrates

Force generation by the growth cone is controlled by expansion and/or contraction of the underlying cytoskeleton. To investigate how substrate mechanics regulates the dynamics of the actin retrograde flow and microtubule polymerization, *Xenopus* eye primordia were transfected by colleagues with LifeAct and EB3 (Figure 26a), which fluorescently label actin filaments in the growth cone and microtubules that mainly reside in the axon shaft, respectively. Once the embryos had developed to stage 34-36, I cultured eye primordia on different substrates and imaged the axonal cytoskeleton (Figure 26a). An example image of labelled actin and microtubules is shown in Figure 26b. For each growth cone, I obtained a kymograph for actin filaments in the growth cone (Figure 26c) and microtubules in the axon shaft (Figure 26d).

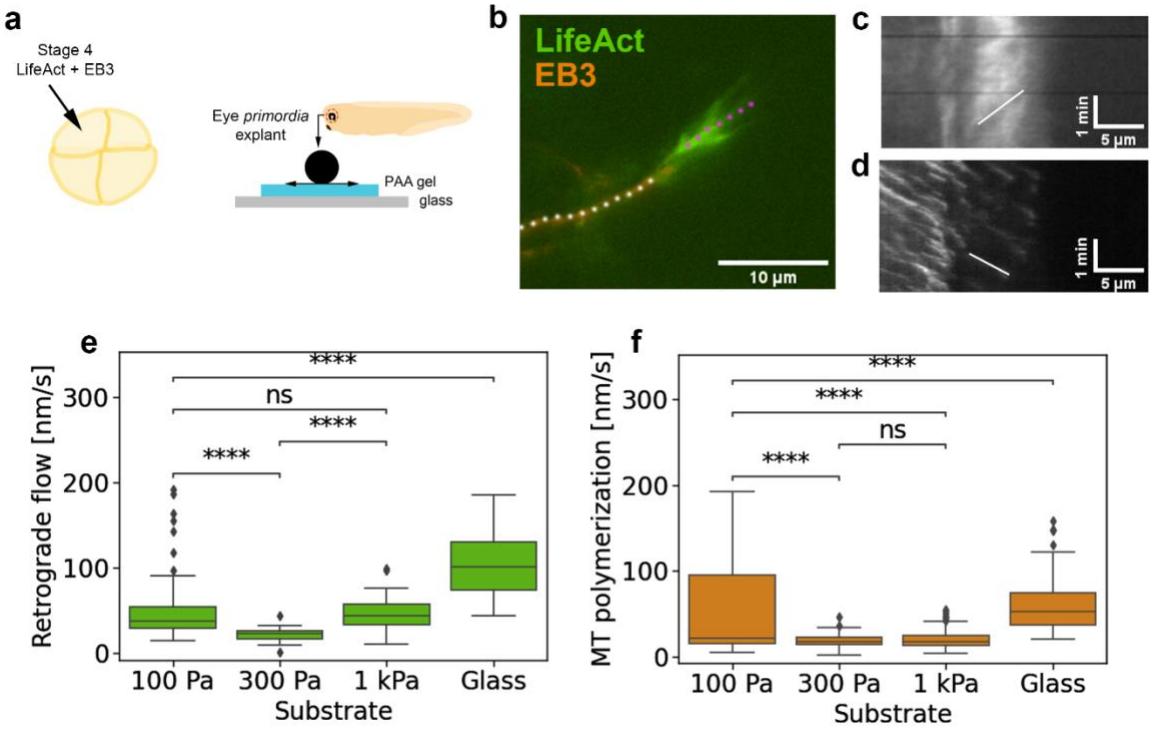

Figure 26 Actin retrograde flow and microtubule polymerization dynamics in *Xenopus* eye primordia explants are regulated by substrate mechanics.

a) Embryos were injected by collaborators with LifeAct and EB3 constructs at stage 4. Eye primordia were explanted at stage 34-36 and plated onto substrates. b) Representative image of actin (LifeAct, green) and microtubule (EB3, orange) labelled growth cone. Example line profiles for microtubules (white dotted line) and actin filaments (pink dotted line) are shown. c) LifeAct kymograph obtained from pink line profile shown in b). d) EB3 kymograph obtained from white line profile shown in b). An example hand drawn line profile that is used to calculate the actin retrograde flow and microtubule with the white angled solid line is shown in c) and d). e) Retrograde flow of actin filaments on substrates of different stiffnesses (number of growth cones N: 100 Pa =52, 300Pa = 23, 1 kPa = 113, glass = 70). Actin retrograde flow decreases and then increases as substrate stiffness increases. f) Microtubule polymerization rate on substrates of different stiffnesses (number of growth cones N: 100 Pa =341, 300Pa = 199, 1 kPa = 503, glass = 294). Microtubule polymerization decreases and then increases as substrate stiffness increases. Mann-Whitney U-test with Bonferroni correction. Ns: $p \leq 1$, $*: 1 \times 10^{-2} < p \leq 5 \times 10^{-2}$, $**: 1 \times 10^{-3} < p \leq 1 \times 10^{-2}$, $***: 1 \times 10^{-4} < p \leq 1 \times 10^{-3}$, $****: p \leq 1 \times 10^{-4}$. The box shows the quartiles (calculated by the interquartile range*

(IQR)) and the whiskers show the rest of the distribution (1.5 IQR) except for points that are determined to be outliers. Outliers are considered as $Q \pm 1.5\ IQR$.

On the softest substrate (100 Pa) the average retrograde flow rates were significantly higher compared (52.83 ± 42.82 nm/s) to 300 Pa substrates (21.67 ± 8.67 nm/s) (Figure 26e). When the substrate stiffness increased to 1 kPa, the retrograde flow rate significantly increased to 43.83 ± 17.86 nm/s from 21.67 ± 8.67 nm/s (300 Pa, Figure 26e). When explants were cultured on glass substrates, the retrograde flow rate increased to 102.40 ± 37.65 nm/s (Figure 26e). Hence, with increasing substrate stiffness, the retrograde flow rate first decreased and then increased (Figure 26e), with a minimum at around 300 Pa. The decrease in retrograde flow between 100 Pa and 300 Pa would also suggest an increase in traction forces, which is consistent with my results presented in the previous section (6.3).

Given that actin filaments are coupled to microtubules in the transition zone of the growth cone, I wanted to understand if microtubule polymerization is regulated by substrate stiffness. On the softest substrates (100 Pa), microtubule polymerisation rates were significantly higher (52.58 ± 49.00 nm/s) compared to 300 Pa (18.51 ± 6.31 nm/s) and 1 kPa (19.34 ± 8.79 nm/s) substrates (Figure 26f). There was no significant difference between microtubules polymerization rates on 300 Pa and 1 kPa substrates. The microtubule polymerization rates were the highest on glass substrates (57.02 ± 25.22 nm/s, Figure 26f).

6.5. Discussion

6.5.1. Automated traction force microscopy analysis

Traction force microscopy (TFM) has become an important method in mechanobiology laboratories to investigate the mechanical forces generated by cells. It has been shown that cellular traction forces are an important parameter for studying cancer (Li et al., 2017), central nervous system development (Betz et al., 2011), and immune cell activation (Fritzsche, 2021). There have been several publications that have focused on developing software to make it easier to analyse TFM data.

There are four key papers that aim to offer a user-friendly solution for TFM analysis. First of all, Martiel et al. (2015) developed an ImageJ plugin that first uses a particle image velocimetry (PIV) algorithms to compute the displacement field and then solves the inverse problem using a L2-regularized Fourier transform traction cytometry (FTTC) algorithm. In short, L2 regularization penalises error by the square of magnitude of that error and FTTC solves the inverse problem in the Fourier space. These regularization methods can be expensive and FTTC can provided stable solutions if the regularization parameter is correctly selected

(Kulkarni et al., 2018). An overestimation of the regularization parameter can lead to a poor approximation of traction forces and give rise to stability issues in the solution. One of the downsides is that the user must manually select the regularization parameter for the FTTC algorithm. Manual selection can make it difficult to analyse large datasets and errors can be introduced from the selection of the regularization parameter.

Han et al. (2015) created a similar package in MATLAB and provided the Boundary Elements Method (BEM) along with the FTTC algorithm. Similar to the ImageJ software, it requires the user to manually select the regularization parameter. Han et al. (2015) do offer an L-curve method to find the best regularization parameter but this is computationally expensive. Furthermore, the L-method does not always work reliably, and the package contains some bugs and poor documentation (personal experience and communication with other scientists in the field).

Bauer et al. (2021) created pyTFM for a user-friendly implementation of Traction Force Microscopy and Mono-layer Stress Microscopy. The software uses the FTTC method and does not use regularization. To avoid noise in the final traction maps, pyTFM uses a user-defined Gaussian low-pass filter, which again requires manual input from the user that could introduce errors.

Huang et al. (2019) addressed the regularization problem by using a Bayesian method to automatically select the best parameter based on the noise. The software is written in MATLAB and the user needs to provide the PIV field in a comma-separated value format generated from elsewhere. Overall, the method presented by Huang et al. (2019) makes it easy to solve the inverse problem with close to zero user input but the user needs to compute the PIV field. After reviewing the different offerings of TFM analysis packages there were some common themes and recurrent issues:

- Most packages usually require manual or (computationally) expensive L2-regularization.
- No package offers a complete analysis pipeline whereby a reference and time frame can be provided, and the results are returned with little to no user input.
- Most of the packages are written in less user-friendly programming languages including MATLAB and Java (ImageJ), which makes it hard for inexperienced users to dig into the code.
- None of the packages were written to simply integrate into existing programmatic workflows.

For the reasons listed above, I decided to combine the desirable features of existing packages into an all-in-one Python package for end-to-end analysis of TFM data with little to no user input. I bootstrapped the OpenPIV library (Liberzon et al., 2021) that automated computation of the displacement field with an iterative PIV method and median filtering. The iterative PIV algorithm did require a window size, but I used a K nearest-neighbours (KNN) algorithm that could approximate this automatically. The KNN algorithm classifies a data point based on how its neighbour is classified. That is, if $Windowsize_1$ was selected for an image with $BeadDensity_1$ then if a new image is predicted with a similar bead density to $BeadDensity_1$ then $Windowsize_1$ will be selected.

It is possible to reconstruct traction forces using finite element methods (Kulkarni et al., 2018) and boundary element methods (Sabass et al., 2008). The main difference is that the finite element methods solve the unknowns in a volume while boundary element methods solve unknowns on the boundary. Therefore, I used an automated Bayesian regularization method from Huang et al. (2019) to compute the traction maps. The Bayesian method was only implemented for the FTTC reconstruction algorithms but can also be used in conjunction with finite element methods and boundary element methods. Subsequently, the Python package that I developed made it easy to analyse large quantities of TFM data with just a few lines of code (code snippet in section 6.2). Automatic regularization parameter selection removes the subjectivity and hence makes it more appropriate to compare traction force measurements in different conditions. In future versions of the software, the Bayesian method could also be applied to the finite element methods and boundary element methods.

6.5.2. Force velocity regulation of axon growth and cytoskeletal dynamics

Polackwich et al. (2015) demonstrated that there are spatiotemporal patterns of forces generated by advancing dorsal root ganglion (DRG) axons, and there is a net pulling force parallel with the axon shaft. Koch et al. (2012) also demonstrated that axons apply a net pulling force. Here, I found that axons exhibited a net ‘pulling’ force parallel to the axon shaft. Pulling forces were larger on 300 Pa substrates compared to 100 Pa substrates (Figure 23b). There were significant differences between the ‘pushing’ force on the different substrates, and pushing forces were always significantly smaller than pulling forces (Figure 23b), suggesting that growth cones predominantly pull, in line with previous literature (Lamoureux et al., 1989).

It is well accepted that actin filaments and microtubule bundles are important for the steering of the growth cone (Zhou et al., 2002). However, Santos et al. (2020) and Dupraz et

al. (2019) showed that axons could grow without pulling on the ECM and that the actin arc in the transition zone inhibits microtubules from protruding towards the leading edge. Thus, it is likely that microtubule progression may be responsible for the physical advancement, but it is regulated by actin retrograde flow (Franze, 2020). There is coupling between microtubules and actin (Dogterom and Koenderink, 2019), and thus, as traction forces build up, microtubules grow past the transition zone and disrupt actin adhesions. As the adhesions are disrupted, microtubules may have infiltrated the growth cone enough to solidify the position and the traction forces are lost. It is well established that disruption of the actin network, myosin, or adhesions enables unrestricted microtubule growth (Koch et al., 2012). Hence, it would be expected that the forces are lost when microtubules initiate growth.

The data presented here suggest that the microtubule polymerization rate is regulated by substrate stiffness (Figure 26f) and follows a similar trend to that of actin retrograde flow (Figure 26e). The actin retrograde flow rates as a function of substrate stiffness followed a similar trend to that reported by Chan and Odde (2008). I hypothesize that actin retrograde flow might regulate microtubule polymerization. Drebrin and EB3 interactions and actin crosslinking family protein 7 (ACF7) and tau interactions link microtubules and actin filaments together (Dogterom and Koenderink, 2019). If correct, it would be expected that decreasing the Drebrin-EB3 or ACF7-tau interactions would inhibit microtubule infiltration and subsequently polymerization rates and advancement. Such experiment could be investigated in future work by genetic knockdowns or by drug treatments. Furthermore, it would be interesting to incorporate this microtubule-actin interaction into the motor clutch simulations to further understand the interplay between microtubules and actin during axon advancement and growth.

6.6. Summary

In this chapter, I developed software to make traction force microscopy analysis easier for users without needing to deeply understand the mathematics and workflow. Hopefully, the software can be used by other biologists to streamline analysis. I wanted to investigate the role of mechanics on axon growth at a mechanistic level. For that reason, I measured the viscoelastic properties of PAA substrates and the traction force and cytoskeletal dynamics of axons on these substrates. I found that growth cones mainly applied “pulling” forces to compliant substrates and the magnitude of the pulling force is modulated by substrate stiffness, in line with previous literature (Koch et al., 2012). There were differences in traction forces but no significant differences between the axon velocity on 100 Pa and 300 Pa substrates. Despite there being no differences in axon velocity, actin retrograde flow rates and microtubule polymerization were

regulated by substrate stiffness. The motor clutch simulations suggested that there should be differences in axon velocities. However, these differences between computational and experimental measurements could have been since velocities and cytoskeletal dynamics were not measured in the same experiment. In future work, it would be good to design a single experiment to measure traction forces, actin retrograde flow, microtubule polymerization, and axon velocities.

6.7. Acknowledgements

K. Mooslehner (Franze lab, PDN, Cambridge) for growing up plasmids. E. K. Pillai and R. McKeown (Franze lab, PDN, Cambridge) for injecting constructs at 4 cell stages.

Conclusions and outlooks

7.1. Viscoelasticity of the developing *Xenopus* brain

To conclude, I demonstrated that it is possible to use a variety of viscoelastic models to fit indentation time data from AFM measurements according to the Maxwell, Voigt, SLM, and PLR models. The SLM fitted indentation time data best for *Xenopus* tissue, rodent, and PAA gels according to a goodness of fit analysis. A major improvement on previous work is that the models consider the force history during the loading. Using analytical solutions, I created a Python library that makes it easy for non-expert users to apply these models to AFM creep data. I also used the Fourier transform of SLM parameters to obtain the storage and loss moduli of the tissue.

Previously, efforts have focused on investigating the elasticity of the tissue through which the optic tract grows. It has been well demonstrated that elastic mechanics are important in *Xenopus* optic tract development. Here, I extended the current framework to investigate the viscoelastic properties of the developing *Xenopus* brain *in vivo*. The tissue exhibited viscoelastic behaviour and the viscous component was heterogeneously distributed. Elastically stiffer regions of the brain had larger viscosities, while elastically softer regions of the brain were less viscous. Therefore, it might not only be tissue elasticity that regulates optic tract development but also viscoelasticity. In future work, there are two key experiments that would add greater understanding of the role of viscoelasticity in the development of the optic pathway:

- Perform time-lapse viscoelasticity AFM measurements on the developing *Xenopus* with a fluorescently labelled optic tract. This would essentially be a viscoelastic extension of the work from Thompson et al. (2019).
- Perturb the elasticity and viscosity of the developing *Xenopus* brain independently to understand how both components regulate axon guidance. However, perturbing the properties independently is challenging because changing the elasticity will change the viscosity and vice-versa.

7.2. Viscoelastic regulation of axon growth

After learning that the developing *Xenopus* brain exhibits viscoelasticity, I investigated if tissue viscoelasticity regulates axon growth. Since it was not possible to independently perturb tissue elasticity and viscosity, I decided to use an *in vitro* approach based on the work of Charrier et al. (2018). I fabricated elastic and viscoelastic substrates with tuneable mechanical properties

and attempted to match the properties of the developing brain tissue. When *Xenopus* eye primordia were cultured on elastic substrates, axons grew significantly longer compared to axons on soft elastic substrates. There were no differences between axon lengths on soft and stiff viscoelastic substrates. Thus, axon growth differed on substrates with similar elastic stiffness but different viscosity, suggesting that viscosity could regulate axon growth on soft viscoelastic substrates.

Despite finding no difference between axon length on soft and stiff viscoelastic substrates, I also found that the elastic and viscoelastic substrates exhibited different mechanical responses. There were discrepancies between the mechanical properties of the elastic and viscoelastic substates depending if they were measured on the bulk scale (shear rheology) or local scale (AFM). These differences could have been due to poroelasticity, swelling, or different loading geometries. I found that axons grew longer when the underlying substrate had a shorter characteristic timescale at the microscopic length scale (that probed with AFM). It was hard to precisely tune the mechanical properties of the gels to meet the desired viscoelasticity of brain tissue. Yet, I hypothesize that substrate timescale could regulate axon growth. In future work, the gel chemistry could be improved to test this substrate timescale hypothesis.

To further understand how substrate mechanics were regulating axon growth, I used the motor clutch model to simulate axon growth. I used an elastic and viscoelastic motor clutch model to simulate retrograde flow, traction forces, and axon velocity. I found that the viscoelastic motor clutch model was a better approximation of axon growth for elastic and viscoelastic substrates and that the substrate timescale could regulate axon velocity.

Exploiting the same framework, I used the *in vivo* AFM data to simulate the axon growth dynamics in the brain. The elastic simulations predicted a linearly decreasing velocity with increasing substrate timescale. The viscoelastic model, in contrast, predicted a biphasic response, with axon velocity increasing at short timescales and then decreasing at intermediate timescales and then maximizing and decreasing again. It predicted that axon growth velocity is maximized at short timescales ($\tau < 0.5$ s) and intermediates timescale ($1.3 < \tau < 1.5$ s). In future work, it would be good to expand the model of Oliveri et al. (2021) to predict axon trajectories according to elastic or viscoelastic motor clutch velocity maps. Furthermore, obtaining time-lapse viscoelastic AFM maps of the developing tissue along with optic tract labelling would enable a direct comparison to *in vivo* experiments.

To further investigate the role of force generation in axon advancement, I investigated traction forces and cytoskeletal dynamics as a function of substrate mechanics measured by AFM. I found that growth cones mainly applied "pulling" forces to compliant substrates and the magnitude of the pulling force is modulated by substrate stiffness. Furthermore, I found that both retrograde flow rates and microtubule polymerization rates were regulated by substrate stiffness. Both actin retrograde flow and microtubule polymerization were higher on soft substrates, then decreased at intermediate stiffnesses, and increased again with increasing substrate stiffness. Along with this analysis, I developed a Python package that could be used to easily analyse traction force microscopy data.

To better understand the role of viscoelasticity in the context of development, it would be good to perform similar measurements on viscoelastic gels, which would require a new protocol to be developed to fabricate viscoelastic TFM gels. Furthermore, the retrograde flow and microtubule polymerization rates should also be measured on viscoelastic substrates, which better resemble brain tissue mechanics. In future work, it would furthermore be interesting to investigate the role of actin-microtubule coupling as a function of substrate stiffness. In summary it would be insightful to:

- Develop viscoelastic substrates that are easier to mechanically tune.
- Use the model from Oliveri et al. (2021) to predict axon trajectories in the developing *Xenopus* brain based on motor clutch simulated velocity maps.
- Add microtubule interaction into the motor clutch model.
- Investigate the role of Drebrin-EB3 or ACF7-tau interactions.

These experiments would enable me to further understand how specifically the viscous component regulates axon growth.

7.3. Closing remarks

In conclusion, I found that the developing *Xenopus* brain exhibits heterogeneous viscoelasticity, which may regulate axon growth during development. *In vitro* explant experiments suggested that axons grow longer on stiff elastic substrates compared to soft elastic substrates, while there was no difference between axons grown on soft and stiff viscoelastic substrates. *In silico*, simulations suggested that viscoelasticity regulates axon growth according to the motor clutch model. The viscoelastic motor clutch model predicted a biphasic axon velocity as a function of characteristic timescale in the brain tissue, while the elastic model predicted a linear decrease in axon velocity with increasing substrate timescale. Different axon velocities for elastic and viscoelastic simulations suggest that viscosity could be important for

regulating axon guidance in development *in vivo*. I found that substrate mechanics regulates both retrograde flow and microtubule polymerisation rate. Therefore, viscosity could also be important in regulating actin and microtubule dynamics and hence potentially regulate axon advancement.

The work in this thesis has added further evidence for the importance of mechanics in axon growth. Viscous tissue properties should be considered when trying to understand axon growth and pathfinding in the developing brain. Here, I have demonstrated that viscosity may be import in CNS development (*in vivo* and *in vitro*) and which could have major consequences in biology, development, and regeneration.

References

ADEBOWALE, K., GONG, Z., HOU, J. C., WISDOM, K. M., GARBETT, D., LEE, H.-P., NAM, S., MEYER, T., ODDE, D. J., SHENOY, V. B. & CHAUDHURI, O. 2021. Enhanced substrate stress relaxation promotes filopodia-mediated cell migration. *Nature Materials,* 20**,** 1290-1299.

ALCARAZ, J., BUSCEMI, L., GRABULOSA, M., TREPAT, X., FABRY, B., FARRÉ, R. & NAVAJAS, D. 2003. Microrheology of Human Lung Epithelial Cells Measured by Atomic Force Microscopy. *Biophysical Journal,* 84**,** 2071-2079.

ALEKYA, B., RAO, S. & PANDYA, H. J. 2019. Engineering approaches for characterizing soft tissue mechanical properties: A review. *Clinical Biomechanics,* 69**,** 127-140.

ANDREU, I., FALCONES, B., HURST, S., CHAHARE, N., QUIROGA, X., LE ROUX, A.-L., KECHAGIA, Z., BEEDLE, A. E. M., ELOSEGUI-ARTOLA, A., TREPAT, X., FARRÉ, R., BETZ, T., ALMENDROS, I. & ROCA-CUSACHS, P. 2021. The force loading rate drives cell mechanosensing through both reinforcement and cytoskeletal softening. *Nature Communications,* 12**,** 4229.

ANTONOVAITE, N., HULSHOF, L. A., HOL, E. M., WADMAN, W. J. & IANNUZZI, D. 2021. Viscoelastic mapping of mouse brain tissue: Relation to structure and age. *Journal of the Mechanical Behavior of Biomedical Materials,* 113**,** 104159.

ATHAMNEH, AHMAD I. M., CARTAGENA-RIVERA, ALEXANDER X., RAMAN, A. & SUTER, DANIEL M. 2015. Substrate Deformation Predicts Neuronal Growth Cone Advance. *Biophysical Journal,* 109**,** 1358-1371.

ATHERTON, J., STOUFFER, M., FRANCIS, F. & MOORES, C. A. 2021. Visualising the cytoskeletal machinery in neuronal growth cones using cryo-electron tomography. *bioRxiv***,** 2021.08.06.455451.

ATKINSON-LEADBEATER, K., BERTOLESI, G. E., HEHR, C. L., WEBBER, C. A., CECHMANEK, P. B. & MCFARLANE, S. 2010. Dynamic Expression of Axon Guidance Cues Required for Optic Tract Development Is Controlled by Fibroblast Growth Factor Signaling. *The Journal of Neuroscience,* 30**,** 685.

BALLAND, M., DESPRAT, N., ICARD, D., FÉRÉOL, S., ASNACIOS, A., BROWAEYS, J., HÉNON, S. & GALLET, F. 2006. Power laws in microrheology experiments on living cells: Comparative analysis and modeling. *Physical Review E,* 74**,** 021911.

BANGASSER, BENJAMIN L., ROSENFELD, STEVEN S. & ODDE, DAVID J. 2013. Determinants of Maximal Force Transmission in a Motor-Clutch Model of Cell Traction in a Compliant Microenvironment. *Biophysical Journal,* 105**,** 581-592.

BANGASSER, B. L., SHAMSAN, G. A., CHAN, C. E., OPOKU, K. N., TÜZEL, E., SCHLICHTMANN, B. W., KASIM, J. A., FULLER, B. J., MCCULLOUGH, B. R., ROSENFELD, S. S. & ODDE, D. J. 2017. Shifting the optimal stiffness for cell migration. *Nature Communications,* 8**,** 15313.

BASU, A., WEN, Q., MAO, X., LUBENSKY, T. C., JANMEY, P. A. & YODH, A. G. 2011. Nonaffine Displacements in Flexible Polymer Networks. *Macromolecules,* 44**,** 1671-1679.

BAUER, A., PRECHOVÁ, M., FISCHER, L., THIEVESSEN, I., GREGOR, M. & FABRY, B. 2021. pyTFM: A tool for traction force and monolayer stress microscopy. *PLOS Computational Biology,* 17**,** e1008364.

BETZ, T., KOCH, D., LU, Y. B., FRANZE, K. & KÄS, J. A. 2011. Growth cones as soft and weak force generators. *Proceedings of the National Academy of Sciences of the United States of America,* 108**,** 13420-13425.

BIGOT, M., CHAUVEAU, F., BEUF, O. & LAMBERT, S. A. 2018. Magnetic Resonance Elastography of Rodent Brain. *Frontiers in Neurology,* 9.

BONFANTI, A., KAPLAN, J. L., CHARRAS, G. & KABLA, A. 2020. Fractional viscoelastic models for power-law materials. *Soft Matter,* 16**,** 6002-6020.

CALHOUN, M. A., BENTIL, S. A., ELLIOTT, E., OTERO, J. J., WINTER, J. O. & DUPAIX, R. B. 2019. Beyond Linear Elastic Modulus: Viscoelastic Models for Brain and Brain Mimetic Hydrogels. *ACS Biomaterials Science & Engineering,* 5**,** 3964-3973.

CAMERON, A. R., FRITH, J. E. & COOPER-WHITE, J. J. 2011. The influence of substrate creep on mesenchymal stem cell behaviour and phenotype. *Biomaterials,* 32**,** 5979-5993.

CAMPBELL, D. S., REGAN, A. G., LOPEZ, J. S., TANNAHILL, D., HARRIS, W. A. & HOLT, C. E. 2001. Semaphorin 3A Elicits Stage-Dependent Collapse, Turning, and Branching in Xenopus Retinal Growth Cones. *The Journal of Neuroscience,* 21**,** 8538.

CANOVIC, E. P., QING, B., MIJAILOVIC, A. S., JAGIELSKA, A., WHITFIELD, M. J., KELLY, E., TURNER, D., SAHIN, M. & VAN VLIET, K. J. 2016. Characterizing Multiscale Mechanical Properties of Brain Tissue Using Atomic Force Microscopy, Impact Indentation, and Rheometry. *JoVE***,** e54201.

CHAN, C. E. & ODDE, D. J. 2008. Traction Dynamics of Filopodia on Compliant Substrates. *Science,* 322**,** 1687.

CHARRIER, E. E., POGODA, K., WELLS, R. G. & JANMEY, P. A. 2018. Control of cell morphology and differentiation by substrates with independently tunable elasticity and viscous dissipation. *Nature Communications,* 9**,** 449.

CHARTRAND, R. 2011. Numerical Differentiation of Noisy, Nonsmooth Data. *ISRN Applied Mathematics,* 2011**,** 11.

CHAUDHURI, O., COOPER-WHITE, J., JANMEY, P. A., MOONEY, D. J. & SHENOY, V. B. 2020. Effects of extracellular matrix viscoelasticity on cellular behaviour. *Nature,* 584**,** 535-546.

CHAUDHURI, O., GU, L., DARNELL, M., KLUMPERS, D., BENCHERIF, S. A., WEAVER, J. C., HUEBSCH, N. & MOONEY, D. J. 2015. Substrate stress relaxation regulates cell spreading. *Nature Communications,* 6**,** 6365.

CHÉDOTAL, A. 2014. Development and plasticity of commissural circuits: from locomotion to brain repair. *Trends in Neurosciences,* 37**,** 551-562.

CHIM, Y. H., MASON, L. M., RATH, N., OLSON, M. F., TASSIERI, M. & YIN, H. 2018. A one-step procedure to probe the viscoelastic properties of cells by Atomic Force Microscopy. *Scientific Reports,* 8**,** 14462.

CHRIST, A. F., FRANZE, K., GAUTIER, H., MOSHAYEDI, P., FAWCETT, J., FRANKLIN, R. J. M., KARADOTTIR, R. T. & GUCK, J. 2010. Mechanical difference between white and gray matter in the rat cerebellum measured by scanning force microscopy. *Journal of Biomechanics,* 43**,** 2986-2992.

CRAIG, E. M. 2018. Model for Coordination of Microtubule and Actin Dynamics in Growth Cone Turning. *Frontiers in Cellular Neuroscience,* 12.

DEINER, M. S., KENNEDY, T. E., FAZELI, A., SERAFINI, T., TESSIER-LAVIGNE, M. & SRETAVAN, D. W. 1997. Netrin-1 and DCC Mediate Axon Guidance Locally at the Optic Disc: Loss of Function Leads to Optic Nerve Hypoplasia. *Neuron,* 19**,** 575-589.

DENT, E. W., BARNES, A. M., TANG, F. & KALIL, K. 2004. Netrin-1 and Semaphorin 3A Promote or Inhibit Cortical Axon Branching, Respectively, by Reorganization of the Cytoskeleton. *The Journal of Neuroscience,* 24**,** 3002.

DENT, E. W., GUPTON, S. L. & GERTLER, F. B. 2011. The growth cone cytoskeleton in axon outgrowth and guidance. *Cold Spring Harbor perspectives in biology,* 3**,** a001800.

DI LORENZO, F., HELLWIG, J., VON KLITZING, R. & SEIFFERT, S. 2015. Macroscopic and Microscopic Elasticity of Heterogeneous Polymer Gels. *ACS Macro Letters,* 4**,** 698-703.

DOGTEROM, M. & KOENDERINK, G. H. 2019. Actin–microtubule crosstalk in cell biology. *Nature Reviews Molecular Cell Biology,* 20**,** 38-54.

DUPRAZ, S., HILTON, B. J., HUSCH, A., SANTOS, T. E., COLES, C. H., STERN, S., BRAKEBUSCH, C. & BRADKE, F. 2019. RhoA Controls Axon Extension Independent of Specification in the Developing Brain. *Current Biology,* 29**,** 3874-3886.e9.

EFREMOV, Y. M., OKAJIMA, T. & RAMAN, A. 2020. Measuring viscoelasticity of soft biological samples using atomic force microscopy. *Soft Matter,* 16**,** 64-81.

EFREMOV, Y. M., SHPICHKA, A. I., KOTOVA, S. L. & TIMASHEV, P. S. 2019. Viscoelastic mapping of cells based on fast force volume and PeakForce Tapping. *Soft Matter,* 15**,** 5455-5463.

EFREMOV, Y. M., WANG, W.-H., HARDY, S. D., GEAHLEN, R. L. & RAMAN, A. 2017. Measuring nanoscale viscoelastic parameters of cells directly from AFM force-displacement curves. *Scientific Reports,* 7**,** 1541.

ELKIN, B. S., AZELOGLU, E. U., COSTA, K. D. & MORRISON, B., 3RD 2007. Mechanical heterogeneity of the rat hippocampus measured by atomic force microscope indentation. *J Neurotrauma,* 24**,** 812-22.

ELKIN, B. S., ILANKOVAN, A. & MORRISON, B., 3RD 2010. Age-dependent regional mechanical properties of the rat hippocampus and cortex. *J Biomech Eng,* 132**,** 011010.

ELOSEGUI-ARTOLA, A., BAZELLIÈRES, E., ALLEN, M. D., ANDREU, I., ORIA, R., SUNYER, R., GOMM, J. J., MARSHALL, J. F., JONES, J. L., TREPAT, X. & ROCA-CUSACHS, P. 2014. Rigidity sensing and adaptation through regulation of integrin types. *Nature Materials,* 13**,** 631.

ELOSEGUI-ARTOLA, A., ORIA, R., CHEN, Y., KOSMALSKA, A., PÉREZ-GONZÁLEZ, C., CASTRO, N., ZHU, C., TREPAT, X. & ROCA-CUSACHS, P. 2016. Mechanical regulation of a molecular clutch defines force transmission and transduction in response to matrix rigidity. *Nature Cell Biology,* 18**,** 540.

ELOSEGUI-ARTOLA, A., TREPAT, X. & ROCA-CUSACHS, P. 2018. Control of Mechanotransduction by Molecular Clutch Dynamics. *Trends in Cell Biology,* 28**,** 356-367.

ERSKINE, L. & HERRERA, E. 2007. The retinal ganglion cell axon's journey: Insights into molecular mechanisms of axon guidance. *Developmental Biology,* 308**,** 1-14.

ERSKINE, L. & HERRERA, E. 2014. Connecting the retina to the brain. *ASN neuro,* 6**,** 1759091414562107.

ESTEKI, M. H., ALEMRAJABI, A. A., HALL, C. M., SHERIDAN, G. K., AZADI, M. & MOEENDARBARY, E. 2020. A new framework for characterization of poroelastic materials using indentation. *Acta Biomaterialia,* 102**,** 138-148.

EVANS, R. M. L., TASSIERI, M., AUHL, D. & WAIGH, T. A. 2009. Direct conversion of rheological compliance measurements into storage and loss moduli. *Physical Review E,* 80.

FLANAGAN, L. A., JU, Y.-E., MARG, B., OSTERFIELD, M. & JANMEY, P. A. 2002. Neurite branching on deformable substrates. *Neuroreport,* 13**,** 2411-2415.

FRANZE, K. 2020. Integrating Chemistry and Mechanics: The Forces Driving Axon Growth. *Annual Review of Cell and Developmental Biology,* 36**,** 61-83.

FRANZE, K. & GUCK, J. 2010. The biophysics of neuronal growth. *Reports on Progress in Physics,* 73.

FRITZSCHE, M. 2021. What Is the Right Mechanical Readout for Understanding the Mechanobiology of the Immune Response? *Frontiers in Cell and Developmental Biology,* 9.

GARCIA, P. D. & GARCIA, R. 2018a. Determination of the Elastic Moduli of a Single Cell Cultured on a Rigid Support by Force Microscopy. *Biophysical Journal,* 114**,** 2923-2932.

GARCIA, P. D. & GARCIA, R. 2018b. Determination of the viscoelastic properties of a single cell cultured on a rigid support by force microscopy. *Nanoscale,* 10**,** 19799-19809.

GARCIA, P. D., GUERRERO, C. R. & GARCIA, R. 2020. Nanorheology of living cells measured by AFM-based force–distance curves. *Nanoscale,* 12**,** 9133-9143.

GARCÍA-MARÍN, V., GARCÍA-LÓPEZ, P. & FREIRE, M. 2009. The Growth Cone as Seen Through Cajal's Original Histological Preparations and Publications. *Journal of the History of the Neurosciences,* 18**,** 197-210.

GOMEZ, T. M. & LETOURNEAU, P. C. 2014. Actin dynamics in growth cone motility and navigation. *Journal of neurochemistry,* 129**,** 221-234.

GONG, Z., SZCZESNY, S. E., CALIARI, S. R., CHARRIER, E. E., CHAUDHURI, O., CAO, X., LIN, Y., MAUCK, R. L., JANMEY, P. A., BURDICK, J. A. & SHENOY, V. B. 2018. Matching material and cellular timescales maximizes cell spreading on viscoelastic substrates. *Proceedings of the National Academy of Sciences,* 115**,** 2686-2695.

GUIMARÃES, C. F., GASPERINI, L., MARQUES, A. P. & REIS, R. L. 2020. The stiffness of living tissues and its implications for tissue engineering. *Nature Reviews Materials,* 5**,** 351-370.

GUO, M., EHRLICHER, ALLEN J., JENSEN, MIKKEL H., RENZ, M., MOORE, JEFFREY R., GOLDMAN, ROBERT D., LIPPINCOTT-SCHWARTZ, J., MACKINTOSH, FREDERICK C. & WEITZ, DAVID A. 2014. Probing the Stochastic, Motor-Driven Properties of the Cytoplasm Using Force Spectrum Microscopy. *Cell,* 158**,** 822-832.

HAN, S. J., OAK, Y., GROISMAN, A. & DANUSER, G. 2015. Traction microscopy to identify force modulation in subresolution adhesions. *Nature Methods,* 12**,** 653.

HARRIS, W. A. 1986. Homing behaviour of axons in the embryonic vertebrate brain. *Nature,* 320**,** 266-269.

HARRIS, W. A. 1989. Local positional cues in the neuroepithelium guide retinal axons in embryonic Xenopus brain. *Nature,* 339**,** 218-221.

HECHT, F. M., RHEINLAENDER, J., SCHIERBAUM, N., GOLDMANN, W. H., FABRY, B. & SCHÄFFER, T. E. 2015. Imaging viscoelastic properties of live cells by AFM: power-law rheology on the nanoscale. 11**,** 4584-4591.

HIRATSUKA, S., MIZUTANI, Y., TODA, A., FUKUSHIMA, N., KAWAHARA, K., TOKUMOTO, H. & OKAJIMA, T. 2009. Power-Law Stress and Creep Relaxations of Single Cells Measured by Colloidal Probe Atomic Force Microscopy. *Japanese Journal of Applied Physics,* 48**,** 08JB17.

HUANG, Y., GOMPPER, G. & SABASS, B. 2020. A Bayesian traction force microscopy method with automated denoising in a user-friendly software package. *Computer Physics Communications,* 256**,** 107313.

HUANG, Y., SCHELL, C., HUBER, T. B., ŞIMŞEK, A. N., HERSCH, N., MERKEL, R., GOMPPER, G. & SABASS, B. 2019. Traction force microscopy with optimized regularization and automated Bayesian parameter selection for comparing cells. *Scientific Reports,* 9**,** 539.

HUI, E., GIMENO, K. I., GUAN, G. & CALIARI, S. R. 2019. Spatial control of viscoelasticity in phototunable hyaluronic acid hydrogels. *bioRxiv***,** 646778.

JAKOBS, M. A. H., ZEMEL, A. & FRANZE, K. 2021. Unrestrained growth of correctly oriented microtubules instructs axonal microtubule orientation. *bioRxiv***,** 2021.06.03.446862.

JALALI, S., DEL POZO, M. A., CHEN, K.-D., MIAO, H., LI, Y.-S., SCHWARTZ, M. A., SHYY, J. Y. J. & CHIEN, S. 2001. Integrin-mediated mechanotransduction requires its

dynamic interaction with specific extracellular matrix (ECM) ligands. *Proceedings of the National Academy of Sciences,* 98**,** 1042.

KAHN, O. I. & BAAS, P. W. 2016. Microtubules and Growth Cones: Motors Drive the Turn. *Trends in neurosciences,* 39**,** 433-440.

KALIL, K. & DENT, E. W. 2014. Branch management: mechanisms of axon branching in the developing vertebrate CNS. *Nature reviews. Neuroscience,* 15**,** 7-18.

KALIL, K., LI, L. & HUTCHINS, B. I. 2011. Signaling Mechanisms in Cortical Axon Growth, Guidance, and Branching. *Frontiers in Neuroanatomy,* 5.

KOCH, D., ROSOFF, WILLIAM J., JIANG, J., GELLER, HERBERT M. & URBACH, JEFFREY S. 2012. Strength in the Periphery: Growth Cone Biomechanics and Substrate Rigidity Response in Peripheral and Central Nervous System Neurons. *Biophysical Journal,* 102**,** 452-460.

KOSER, D. E., MOEENDARBARY, E., HANNE, J., KUERTEN, S. & FRANZE, K. 2015. CNS cell distribution and axon orientation determine local spinal cord mechanical properties. *Biophysical Journal,* 108**,** 2137-2147.

KOSER, D. E., THOMPSON, A. J., FOSTER, S. K., DWIVEDY, A., PILLAI, E. K., SHERIDAN, G. K., SVOBODA, H., VIANA, M., COSTA, L. D. F., GUCK, J., HOLT, C. E. & FRANZE, K. 2016. Mechanosensing is critical for axon growth in the developing brain. *Nat. Neurosci.,* 19**,** 1592--1598.

KULKARNI, A. H., GHOSH, P., SEETHARAMAN, A., KONDAIAH, P. & GUNDIAH, N. 2018. Traction cytometry: regularization in the Fourier approach and comparisons with finite element method. *Soft Matter,* 14**,** 4687-4695.

LAMOUREUX, P., BUXBAUM, R. E. & HEIDEMANN, S. R. 1989. Direct evidence that growth cones pull. *Nature,* 340**,** 159-162.

LAN, P. S., GLASER, K. J., EHMAN, R. L. & GLOVER, G. H. 2020. Imaging brain function with simultaneous BOLD and viscoelasticity contrast: fMRI/fMRE. *NeuroImage,* 211**,** 116592.

LEE, A. C. & SUTER, D. M. 2008. Quantitative analysis of microtubule dynamics during adhesion-mediated growth cone guidance. *Developmental Neurobiology,* 68**,** 1363-1377.

LI, Z., PERSSON, H., ADOLFSSON, K., ABARIUTE, L., BORGSTRÖM, M. T., HESSMAN, D., ÅSTRÖM, K., OREDSSON, S. & PRINZ, C. N. 2017. Cellular traction forces: a useful parameter in cancer research. *Nanoscale,* 9**,** 19039-19044.

LIBERZON, A., KÄUFER, T., BAUER, A., VENNEMANN, P. & ZIMMER, E. 2021. OpenPIV/openpiv-python: OpenPIV-Python v0.23.4.

LIN, C.-H. & FORSCHER, P. 1995. Growth cone advance is inversely proportional to retrograde F-actin flow. *Neuron,* 14**,** 763-771.

LU, Y. B., FRANZE, K., SEIFERT, G., STEINHÄUSER, C., KIRCHHOFF, F., WOLBURG, H., GUCK, J., JANMEY, P., WEI, E. Q., KÄS, J. & REICHENBACH, A. 2006. Viscoelastic properties of individual glial cells and neurons in the CNS. *Proceedings of the National Academy of Sciences of the United States of America,* 103**,** 17759-17764.

LUTOLF, M. P. & HUBBELL, J. A. 2005. Synthetic biomaterials as instructive extracellular microenvironments for morphogenesis in tissue engineering. *Nature Biotechnology,* 23**,** 47-55.

MANDAL, K., GONG, Z., RYLANDER, A., SHENOY, V. B. & JANMEY, P. A. 2020. Opposite responses of normal hepatocytes and hepatocellular carcinoma cells to substrate viscoelasticity. *Biomaterials Science,* 8**,** 1316-1328.

MARTIEL, J.-L., LEAL, A., KURZAWA, L., BALLAND, M., WANG, I., VIGNAUD, T., TSENG, Q. & THÉRY, M. 2015. Chapter 15 - Measurement of cell traction forces with ImageJ. *In:* PALUCH, E. K. (ed.) *Methods in Cell Biology.* Academic Press.

MERRIAM, E. B., MILLETTE, M., LUMBARD, D. C., SAENGSAWANG, W., FOTHERGILL, T., HU, X., FERHAT, L. & DENT, E. W. 2013. Synaptic regulation of microtubule dynamics in dendritic spines by calcium, F-actin, and drebrin. *The Journal of neuroscience : the official journal of the Society for Neuroscience,* 33**,** 16471-16482.

MESSERSMITH, E. K., LEONARDO, E. D., SHATZ, C. J., TESSIER-LAVIGNE, M., GOODMAN, C. S. & KOLODKIN, A. L. 1995. Sernaphorin III can function as a selective chemorepellent to pattern sensory projections in the spinal cord. *Neuron,* 14**,** 949-959.

MIGUEL-RUIZ, J. E. S. & LETOURNEAU, P. C. 2014. The Role of Arp2/3 in Growth Cone Actin Dynamics and Guidance Is Substrate Dependent. *Journal of Neuroscience,* 34**,** 5895-5908.

MOEENDARBARY, E., WEBER, I. P., SHERIDAN, G. K., KOSER, D. E., SOLEMAN, S., HAENZI, B., BRADBURY, E. J., FAWCETT, J. & FRANZE, K. 2017. The soft mechanical signature of glial scars in the central nervous system. *Nature communications,* 8**,** 14787-14787.

MOGILNER, A. & OSTER, G. 1996. Cell motility driven by actin polymerization. *Biophysical journal,* 71**,** 3030-3045.

MOSHAYEDI, P., DA F COSTA, L., CHRIST, A., LACOUR, S. P., FAWCETT, J., GUCK, J. & FRANZE, K. 2010. Mechanosensitivity of astrocytes on optimized polyacrylamide gels analyzed by quantitative morphometry. *Journal of Physics Condensed Matter,* 22.

MURPHY, M. C., HUSTON, J. & EHMAN, R. L. 2019. MR elastography of the brain and its application in neurological diseases. *NeuroImage,* 187**,** 176-183.

NAKAGAWA, S., BRENNAN, C., JOHNSON, K. G., SHEWAN, D., HARRIS, W. A. & HOLT, C. E. 2000. Ephrin-B regulates the Ipsilateral routing of retinal axons at the optic chiasm. *Neuron,* 25**,** 599-610.

NAM, S., STOWERS, R., LOU, J., XIA, Y. & CHAUDHURI, O. 2019. Varying PEG density to control stress relaxation in alginate-PEG hydrogels for 3D cell culture studies. *Biomaterials,* 200**,** 15-24.

NIEUWKOOP, P. D. & FABER, J. 1956. *Normal table of Xenopus laevis (Daudin) a systematical and chronological survey of the development from the fertilized egg till the end of metamorphosis,* Amsterdam, Amsterdam, 1956.

NIEUWKOOP, P. D. & FABER, J. 1994. *Normal table of Xenopus laevis (Daudin)*, Routledge.

O'LEARY, D. D. M. & MCLAUGHLIN, T. 2005. Mechanisms of retinotopic map development: Ephs, ephrins, and spontaneous correlated retinal activity. *Progress in Brain Research.* Elsevier.

OLIVERI, H., FRANZE, K. & GORIELY, A. 2021. Theory for Durotactic Axon Guidance. *Physical Review Letters,* 126**,** 118101.

PIPER, M., ANDERSON, R., DWIVEDY, A., WEINL, C., VAN HORCK, F., LEUNG, K. M., COGILL, E. & HOLT, C. 2006. Signaling Mechanisms Underlying Slit2-Induced Collapse of Xenopus Retinal Growth Cones. *Neuron,* 49**,** 215-228.

PLOTNIKOV, SERGEY V., PASAPERA, ANA M., SABASS, B. & WATERMAN, CLARE M. 2012. Force Fluctuations within Focal Adhesions Mediate ECM-Rigidity Sensing to Guide Directed Cell Migration. *Cell,* 151**,** 1513-1527.

POLACKWICH, R. J., KOCH, D., MCALLISTER, R., GELLER, H. M. & URBACH, J. S. 2015. Traction force and tension fluctuations in growing axons. *Frontiers in cellular neuroscience,* 9**,** 417-417.

RAMON, Y. & CAJAL, S. 1899. Textura del Sistema Nervioso del Hombre y de los Vertebrados. *Imprenta y Librería de Nicolás Moya, Madrid (1899–1904)*.

RAMÓN Y CAJAL, S. 1909. *Histologie du système nerveux de l'homme & des vertébrés / par S. Ramón Cajal*
traduite de l'Espagnol par L. Azoulay, Paris, Paris : A. Maloine, 1909-1911.

RANSOHOFF, R. M. & CARDONA, A. E. 2010. The myeloid cells of the central nervous system parenchyma. *Nature,* 468**,** 253-262.

RASBAND, K., HARDY, M. & CHIEN, C.-B. 2003. Generating X: Formation of the Optic Chiasm. *Neuron,* 39**,** 885-888.

RHEINLAENDER, J. & SCHÄFFER, T. E. 2019. Mapping the creep compliance of living cells with scanning ion conductance microscopy reveals a subcellular correlation between stiffness and fluidity. *Nanoscale,* 11**,** 6982-6989.

SABASS, B., GARDEL, M. L., WATERMAN, C. M. & SCHWARZ, U. S. 2008. High resolution traction force microscopy based on experimental and computational advances. *Biophysical journal,* 94**,** 207-220.

SANTOS, T. E., SCHAFFRAN, B., BROGUIÈRE, N., MEYN, L., ZENOBI-WONG, M. & BRADKE, F. 2020. Axon Growth of CNS Neurons in Three Dimensions Is Amoeboid and Independent of Adhesions. *Cell Reports,* 32**,** 107907.

SCHAEFER, A. W., KABIR, N. & FORSCHER, P. 2002. Filopodia and actin arcs guide the assembly and transport of two populations of microtubules with unique dynamic parameters in neuronal growth cones. *The Journal of cell biology,* 158**,** 139-152.

SCHIERBAUM, N., RHEINLAENDER, J. & SCHAFFER, T. E. 2019. Combined atomic force microscopy (AFM) and traction force microscopy (TFM) reveals a correlation between viscoelastic material properties and contractile prestress of living cells. *Soft Matter,* 15**,** 1721-1729.

SEGEL, M., NEUMANN, B., HILL, M. F. E., WEBER, I. P., VISCOMI, C., ZHAO, C., YOUNG, A., AGLEY, C. C., THOMPSON, A. J., GONZALEZ, G. A., SHARMA, A., HOLMQVIST, S., ROWITCH, D. H., FRANZE, K., FRANKLIN, R. J. M. & CHALUT, K. J. 2019. Niche stiffness underlies the ageing of central nervous system progenitor cells. *Nature,* 573**,** 130-134.

SERAFINI, T., COLAMARINO, S. A., LEONARDO, E. D., WANG, H., BEDDINGTON, R., SKARNES, W. C. & TESSIER-LAVIGNE, M. 1996. Netrin-1 Is Required for Commissural Axon Guidance in the Developing Vertebrate Nervous System. *Cell,* 87**,** 1001-1014.

SHOLL, D. A. 1953. Dendritic organization in the neurons of the visual and motor cortices of the cat. *Journal of anatomy,* 87**,** 387-406.

SRIDHAR, M. & INSANA, M. F. 2007. Ultrasonic measurements of breast viscoelasticity. *Medical physics,* 34**,** 4757-4767.

SUBRAMANI, R., IZQUIERDO-ALVAREZ, A., BHATTACHARYA, P., MEERTS, M., MOLDENAERS, P., RAMON, H. & VAN OOSTERWYCK, H. 2020. The Influence

of Swelling on Elastic Properties of Polyacrylamide Hydrogels. *Frontiers in Materials,* 7.

SUGIMURA, K., LENNE, P.-F. & GRANER, F. 2016. Measuring forces and stresses in situ in living tissues. *Development,* 143**,** 186-196.

TANAKA, E. & KIRSCHNER, M. W. 1995. The role of microtubules in growth cone turning at substrate boundaries. *The Journal of cell biology,* 128**,** 127-137.

TANAKA, E. M. & KIRSCHNER, M. W. 1991. Microtubule behavior in the growth cones of living neurons during axon elongation. *Journal of Cell Biology,* 115**,** 345-363.

TEDESCHI, A., DUPRAZ, S., CURCIO, M., LASKOWSKI, C. J., SCHAFFRAN, B., FLYNN, K. C., SANTOS, T. E., STERN, S., HILTON, B. J., LARSON, M. J. E., GURNIAK, C. B., WITKE, W. & BRADKE, F. 2019. ADF/Cofilin-Mediated Actin Turnover Promotes Axon Regeneration in the Adult CNS. *Neuron,* 103**,** 1073-1085.e6.

THOMPSON, A. J., PILLAI, E. K., DIMOV, I. B., FOSTER, S. K., HOLT, C. E. & FRANZE, K. 2019. Rapid changes in tissue mechanics regulate cell behaviour in the developing embryonic brain. *eLife,* 8**,** e39356.

VAN HORCK, F. P. G., WEINL, C. & HOLT, C. E. 2004. Retinal axon guidance: novel mechanisms for steering. *Current opinion in neurobiology,* 14**,** 61-66.

VAN OOSTEN, A. S. G., CHEN, X., CHIN, L., CRUZ, K., PATTESON, A. E., POGODA, K., SHENOY, V. B. & JANMEY, P. A. 2019. Emergence of tissue-like mechanics from fibrous networks confined by close-packed cells. *Nature,* 573**,** 96-101.

VILJOEN, A., MATHELIÉ-GUINLET, M., RAY, A., STROHMEYER, N., OH, Y. J., HINTERDORFER, P., MÜLLER, D. J., ALSTEENS, D. & DUFRÊNE, Y. F. 2021. Force spectroscopy of single cells using atomic force microscopy. *Nature Reviews Methods Primers,* 1**,** 63.

WANG, H. C. & WINEMAN, A. S. 1972. A mathematical model for the determination of viscoelastic behavior of brain in vivo—I Oscillatory response. *Journal of Biomechanics,* 5**,** 431-446.

WEBER, I. P., YUN, S. H., SCARCELLI, G. & FRANZE, K. 2017. The role of cell body density in ruminant retina mechanics assessed by atomic force and Brillouin microscopy. *Physical Biology,* 14.

WELSHHANS, K. & BASSELL, G. J. 2011. Netrin-1-induced local β-actin synthesis and growth cone guidance requires zipcode binding protein 1. *The Journal of neuroscience : the official journal of the Society for Neuroscience,* 31**,** 9800-9813.

WEN, Z. & ZHENG, J. Q. 2006. Directional guidance of nerve growth cones. *Current Opinion in Neurobiology,* 16**,** 52-58.

WHITAKER, D. J., HUANG, Z., LONGBOTTOM, B. W., SALA, R. L., WU, G. & SCHERMAN, O. A. 2021. Supramolecular hydrogels prepared from fluorescent alkyl pyridinium acrylamide monomers and CB[8]. *Polymer Chemistry,* 12**,** 519-525.

WILLIAMSON, T., GORDON-WEEKS, P. R., SCHACHNER, M. & TAYLOR, J. 1996. Microtubule reorganization is obligatory for growth cone turning. *Proceedings of the National Academy of Sciences,* 93**,** 15221-15226.

ZHANG, L. I., TAO, H. W., HOLT, C. E., HARRIS, W. A. & POO, M.-M. 1998. A critical window for cooperation and competition among developing retinotectal synapses. *Nature,* 395**,** 37-44.

ZHOU , F.-Q., WATERMAN-STORER , C. M. & COHAN , C. S. 2002. Focal loss of actin bundles causes microtubule redistribution and growth cone turning. *Journal of Cell Biology,* 157**,** 839-849.